DIPLOMARBEIT

Quantifying the impact of climate oscillation on Mediterranean hydrology using multivariate statistics

Ausgeführt am Department für Geodäsie und Geoinforamtion
der Technischen Universität Wien

unter der Anleitung von
Univ.Prof. Dr.rer.nat. MSc Wouter Arnoud Dorigo

betreut durch
Univ.Ass. Dipl.-Ing. Bernhard Bauer-Marschallinger

durch
Agnes Kauer

Wien, Dezember 2017

Abstract

The Mediterranean area has a complex geography covering several climate zones. Currently the interactions and processes of the hydrological cycle in the area are in the focus of many scientific studies due to the increase in extreme weather events and climate change impact. The ever-increasing need for water in tourism and agriculture reinforces the problem in areas of drought. Therefore, monitoring and better understanding of the hydrological cycle are crucial in order to create better long-term forecasts for this area.

The variabilities in climate that follow distinct repeating spatio-temporal patterns known as climate modes, are one of the major drivers for the hydrological cycle. Therefore, this study seeks to quantify the relationship between regional climate modes and the hydrological cycle in the study area. Empirical Orthogonal Functions (EOF), and variations of them, are applied to a wide range of hydrological datasets to extract the major variation over the study period. More than ten datasets, describing precipitation, soil moisture, and evapotranspiration, have been analysed to give further support and enrich findings of earlier studies. The time span of the datasets varies and lies within 1980 - 2015. The resulting EOFs are then correlated with regional climate modes using Spearman Rank correlation analysis. This is done for the entire time span of the EOFs by monthly and seasonal means.

There is evidence for relationships between hydrological phenomenon and the climate modes North Atlantic Oscillation (NAO), Arctic Oscillation (AO), Eastern Atlantic (EA), and Tropical Northern Atlantic (TNA). By analysing by seasonal and monthly means, especially high correlation in the winter months are found. However, the results strongly depend on the study area extent.

The findings suggest an impact of regional climate modes on the hydrological cycle in the Mediterranean area.

Kurzfassung

Der mediterrane Raum hat eine komplexe Geographie, die sich über verschiedene Klimazonen streckt. Die Interaktionen und Prozesse des Wasserkreislaufs der Region sind aufgrund der Häufung von extremen Wetterphänomenen und dem Klimawandel derzeit im Fokus vieler wissenschaftlicher Studien. Der ständig wachsende Bedarf an Wasser durch den Tourismus und durch die Landwirtschaft verstärkt die Probleme in von Dürren geplagten Gegenden noch weiter. Deshalb sind Monitoring und ein besseres Verständnis für den Wasserkreislauf in dieser Region besonders wichtig.

Variationen im Klima, die speziellen räumlichen und zeitlichen Mustern folgen und als Klimaoszillationen bekannt sind, sind ein wichtiger Treiber des Wasserkreislaufs. Deshalb versucht diese Arbeit ein besseres Verständnis für die Verbindung zwischen lokalen Klimaoszillationen und dem Wasserkreislauf in der Region zu erreichen. Empirische Orthogonale Funktionen (EOF) und dessen Variationen werden an eine große Auswahl von Datensätzen, die den Wasserkreislauf beschreiben angewendet, um die Hauptkomponenten für den Betrachtungszeitraum zu extrahieren. Mehr als zehn Datensätze, die Niederschlag, Evapotranspiration und Bodenfeuchte beschreiben wurden untersucht, um die bisherigen wissenschaftlichen Studien zu ergänzen. Die Datensätze decken unterschiedliche Perioden im Zeitraum von 1980-2015 ab. Die berechneten EOFs werden dann mit regionalen Klimamodi mit der Spearman Rank Korrelationsanalyse korreliert. Das wird für die gesamte Studiendauer der EOFs gemacht, sowohl für monatliche als auch saisonale Mittelwerte.

Die Ergebnisse sprechen für eine Beziehung zwischen den hydrologischen Datensätzen und den Klimaoszillationen NAO, AO, EA und TNA. Bei Analysen der jeweils monatlichen und saisonalen Mittelwerte finden sich besonders hohe Korrelationen in den

Wintermonaten. Gleichzeitig wurde eine starke Abhängigkeit der Ergebnisse von den gewählten Studienbereichen gefunden.

Die Ergebnisse deuten auf einen Einfluss der regionalen Klima Oszillationen auf den Wasserzyklus im Mediterranen Raum hin.

Acknowledgements

This master thesis was written in the Research Group Climate and Environmental Remote Sensing (CLIMERS) at the Department of Geodesy and Geoinformation. My first thanks go to my supervisors who guided me through this process with a lot of patience and knowledge. Especially Bernhard Bauer-Marschallinger always had an open door, ready to help me with any difficulties. Wouter Dorigo supported me with his scientific expertise and inspired me to go further and to dig deeper. Appreciation also goes out to all the bright minds behind the WACMOS-MED project, that made it possible for me to use such a large amount of datasets.

The task of not just completing my thesis, but also my degree at the Vienna University of Technology, would not have been possible without the amazing support I received throughout the last seven years and my entire life. Friends, mentors, scouts and guides from around the world, and most of all Diogo, were always great inspirations and sources of energy. But the biggest gratitude goes out to my incredible family. From my grandmother, who has always been my greatest inspiration, my sister who always had an open ear, to my amazing parents, who, with their never ending support and love, made it all possible.

Thank you! Danke! Obrigada!

Contents

1 Introduction 1

2 Climate and Hydrology of the Mediterranean Area 5
- 2.1 The Mediterranean Area . . . 5
  - 2.1.1 The Mediterranean Basin . . . 5
  - 2.1.2 The Mediterranean Region . . . 7
- 2.2 The Climate in the Mediterranean Region . . . 8
- 2.3 Hydrology . . . 11
  - 2.3.1 Precipitation . . . 14
  - 2.3.2 Evapotranspiration . . . 15
  - 2.3.3 Soil Moisture . . . 16
  - 2.3.4 Climate Change Projections in the Mediterranean Region . . . 16

3 Climate Modes 19
- 3.1 North Atlantic Oscillation Pattern . . . 20
- 3.2 Tropical North Atlantic Pattern . . . 22
- 3.3 Eastern Atlantic Pattern . . . 23
- 3.4 Arctic Oscillation Pattern . . . 24
- 3.5 El Niño Southern Oscillation . . . 25
- 3.6 Influence of Climate Modes in the Region . . . 27

4 Data 31
- 4.1 Precipitation . . . 31
  - 4.1.1 GPCP . . . 33
  - 4.1.2 CMORPH . . . 33
  - 4.1.3 TRMM-TMPA . . . 33

4.2 Evapotranspiration 34
4.2.1 GLEAM v3 34
4.2.2 MODIS16 34
4.2.3 PML-ET 35
4.2.4 PT-JPL 35
4.2.5 NTSG 35
4.3 Soil Moisture 35
4.3.1 CCI Soil Moisture 36

5 Methods **37**
5.1 Study Setup 37
5.2 Empirical Orthogonal Functions 40
5.3 Variations of EOF Analysis 47
5.3.1 Complex Orthogonal Functions 47
5.3.2 EOF Rotations 50
5.4 Correlations 53

6 Results and Discussion **55**
6.1 Revealing the impact of methodological choices on identifying main patterns of evaporation 55
6.1.1 Spatial Subset 56
6.1.2 Variations of EOF analysis 59
6.1.3 Correlations with Climate Modes 65
6.2 General Results 75
6.2.1 Precipitation 75
6.2.2 Evapotranspiration 75
6.2.3 Soil Moisture 79

7 Conclusion **87**

Acronyms **89**

Bibliography **91**

List of Tables

2.1 Köppen-Geier Climate Classes 10

3.1 Climate Oscillation Indices used in this study. 20

4.1 Datasets used in this study 32

List of Figures

2.1 The Mediterranean Basin 6
2.2 The Mediterranean Region 7
2.3 The Köppen-Geier Classification 9
2.4 Climograph Examples for Climate Classifications 12
2.5 The Hydrological Cycle 13

3.1 Positive and Negative NAO 21
3.2 NAO 1980-2014 22
3.3 TNA 1980-2014 23
3.4 EA 1980-2014 24
3.5 Positive and Negative AO 25
3.6 AO 1980-2014 26
3.7 SOI 1980-2014 27

5.1 Data Structure Tree 1 37
5.2 Data Structure Tree 2 38
5.3 Data Structure Tree 3 38
5.4 Data Structure Tree 4 38
5.5 Data Structure Tree 5 38
5.6 Data Structure Tree 6 39
5.7 Data Structure Tree 7 40
5.8 EOF Analysis 41

6.1 Results of EOF analysis applied to the GLEAMv3 dataset with the spatial extent of the Mediterranean Basin 57
6.2 Results of EOF analysis applied to the GLEAMv3 dataset with the spatial extent of the Mediterranean Region 58

6.3 Results of Complex EOF analysis applied to the GLEAMv3 dataset - Part 1 61
6.3 Results of Complex EOF analysis applied to the GLEAMv3 dataset - Part 2 62
6.4 Results of EOF analysis with rotation using the varimax criterion applied to the GLEAMv3 dataset with the spatial extent of the Mediterranean Region 63
6.5 Results of EOF analysis with rotation using the quartimin criterion applied to the GLEAMv3 dataset with the spatial extent of the Mediterranean Region 64
6.6 Monthly correlations of EOFs and climate modes 66
6.7 Results of EOF analysis applied to the GLEAMv3 dataset with seasonal values 67
6.8 Seasonal correlations of EOFs and climate modes 68
6.9 Correlation by season - Part 1 70
6.9 Correlation by season - Part 2 71
6.10 Individual plots for seasonal correlation for analysis results for GLEAMv3 data 72
6.11 Correlation of the results of CEOF - Part 1 73
6.11 Correlation of the results of CEOF - Part 2 74
6.12 Results of EOF analysis applied to the GPCP dataset with seasonal values 76
6.13 Correlation by season for the GPCP dataset - Part 1 77
6.13 Correlation by season for the GPCP dataset - Part 2 78
6.14 Results of EOF analysis applied to the MODIS16 dataset with seasonal values 80
6.15 Results of EOF analysis with rotation using the varimax criterion applied to the MODIS16 dataset 81
6.16 Results of EOF analysis with rotation using the quartimin criterion applied to the MODIS16 dataset 82
6.17 Results of EOF analysis applied to the CCI Soil Moisture dataset with seasonal values 83
6.18 Correlation by season for the CCI Soil Moisture dataset - Part 1 84
6.18 Correlation by season for the CCI Soil Moisture dataset - Part 2 85

1 Introduction

This thesis aims to quantify the impact of climatic oscillation on the hydrological cycle of the Mediterranean area. A strong motivation to study the hydrological cycle is the practical need for water management to handle water scarcity and other water-related hazards in this particular region of the planet [14]. This study is part of the WACMOS-MED project which seeks to monitor the water cycle in the Mediterranean area based on remote sensing data. Satellite remote sensing offers valuable possibilities for monitoring the individual parts of the hydrological cycle on a large scale.

The hydrological cycle describes the circulation of water within the climate system, which is here understood as the atmosphere, hydrosphere, cryosphere, land surface, and the biosphere. The interaction between these component is very complex and makes it difficult to fully understand the system. Any changes in the components or their interaction, whether natural or anthropogenic, may cause changes in climate. The term climate, therefore in a wider sense refers to the state of the climate system as a whole. More commonly, climate is defined as the average weather in one location over a substantial period of time [29].

To better understand changes in climate, it is important to understand the natural variability in climate. The climate's main drivers are the radiation from the sun and the rotation of our planet, but there also exist other forms of oscillations, called climate modes. These variabilities in climate follow distinct repeating spatial-temporal patterns, which can be yearly, diurnal, seasonal, or quasi-periodic cycles. In general, the modes describe the spatial structure of two strongly coupled areas, but instead of being spatially independent, one can see synchronized behaviour in regions that are far apart [75]. The El Niño Southern Oscillation, the North Atlantic Oscillation, and the Arctic Oscillation are well-known examples for climate modes. Some oscillations are more localised within a smaller region while others affect regions across the globe [13]. Climate modes are a major driver for hydrology in many regions of the world, including the Mediterranean [46][17][24][6].

The Mediterranean was chosen as a study area due to the extreme effects changes in climate have on the hydrological cycle there [32]. The region is already experiencing droughts, forest fires, rivers drying up, but also extensive flooding [72]. Due to heavy tourism and agriculture, water scarcity is also largely due to human activities in the area. Further the IPCC 2007 [72] also expects a significant change in the hydrological cycle in the Mediterranean region [44] [43]. Therefore, it is especially important to understand the connection of the regional climate in the Mediterranean with the global climate. By quantifying the impact of climate oscillations on the Mediterranean hydrology, an important step taken in right directions.

There already exist studies that tie the climate oscillations to the climate in the Mediterranean region. The winters in the Mediterranean region are dominated by the wet air coming from the west with storms forming over the Atlantic. These so-called 'Westerlies' are affected by Atlantic climate oscillations, especially in the western part of Europe [23]. Other climate modes are believed to have a significant impact on the climate in the Mediterranean region. These climate modes are heavily monitored and studied on their variability because of global climate change. The impact that they have on the Mediterranean climate needs to be better understood and quantified, to help understand the effect that climate change will have on the Mediterranean region.

This study uses Empirical Orthogonal Functions (EOF) Analysis to extract the main signals out of large hydrological datasets, to quantify the impact of climate oscillations on the Mediterranean water cycle. This significantly reduces the complexity of the dataset and enables correlation analyses with climate oscillation indices. These indices describe the climate oscillations with simple numerical values, which are derived from complex climate observations.

This study will first give a broad introduction to the climate in the study area and any predictions on the future of the climate in the region. Then the climate modes are introduced and their impact on the Mediterranean is highlighted. After these two theoretical chapters, the datasets used in this study are introduced followed by a thorough explanation of the methods used. Ultimately, the results are presented and the conclusions of the study are summarised.

2 Climate and Hydrology of the Mediterranean Area

In this chapter, the geography of the region is roughly introduced. Further, the climate of the Mediterranean region is discussed. In this study only hydrological variables are considered, and for this reason this chapter will also briefly introduce the hydrological cycle in the Mediterranean and some key components of it. Further, the impacts of climate change on the region are outlined at the end of the chapter, emphasizing on the effects on the hydrology.

2.1 The Mediterranean Area

In this study, we differentiate between the Mediterranean basin (Figure 2.1) and the Mediterranean region (Figure 2.2). While the Mediterranean basin covers a much larger and more diverse area, the Mediterranean region, as defined for this study, includes mostly the Mediterranean Sea and the surrounding lands.

2.1.1 The Mediterranean Basin

The Mediterranean basin is defined by the total catchment area of the Mediterranean Sea. This includes all rivers that lead into the Mediterranean Sea including the Black Sea and its catchment area and the Nile river. The area reaches from the Atlantic in the west to the Don river in the east, and from Moscow in the north to Lake Victoria in the south, covering an area of approximately 5 million km^2 (Figure 2.1) [40].

The four largest Mediterranean catchments are the rivers Ebro, Rhone, Po, and Nile which account for roughly 60% of total Mediterranean river discharge [40]. The Nile river takes on a special role by transporting rainfall to a completely detached area. This allochthonous water source has an impact on the salinity of the Mediterranean Sea especially in the eastern Mediterranean [7].

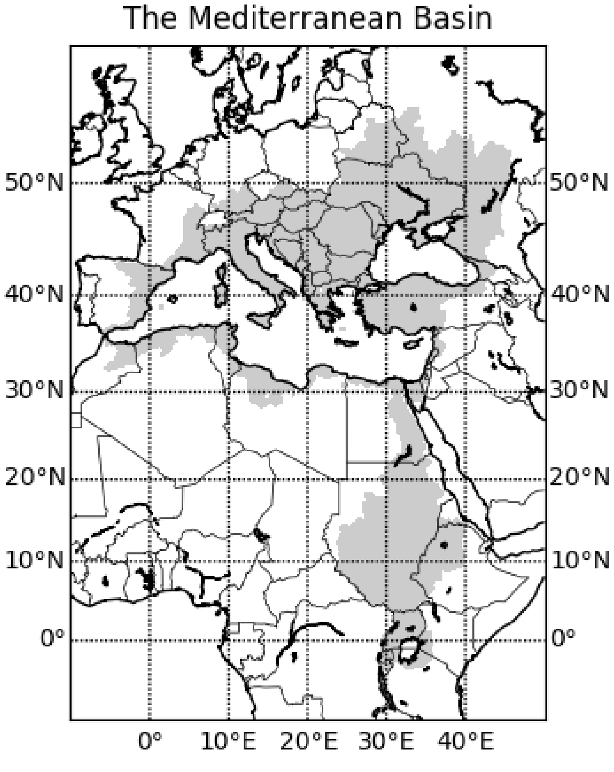

Figure 2.1: The Mediterranean basin is shown here in grey, covering the total catchment area of the Mediterranean Sea. It includes all river basins that drain into the Mediterranean Sea including the Nile river.

The Mediterranean basin stretches across several climate zones. It includes equatorial climates from equatorial monsoon around Lake Victoria to equatorial savannah, then Arid climates with steppe and desert climate. Further north the Mediterranean basin has warm temperate climates in the west and snow climates in the north east of the basin [38].

2.1.2 The Mediterranean Region

The Mediterranean region is the land surrounding the Mediterranean Sea. There is no definition on the exact extent of the Mediterranean region, but in most studies of the Mediterranean climate, a region spanning approximately between 25°N - 50°N and 10°W - 45°E is used (Figure 2.2). With these boundaries, the Mediterranean region ranges from the Alpine region in the north to the Sahara Desert in the south and from the Iberian Peninsula in the west to the Middle East in the east. This area includes, fully or partially, more than 25 countries, which lie on three different continents. This bounding box is chosen generously to ensure that all areas of the Mediterranean region are included.

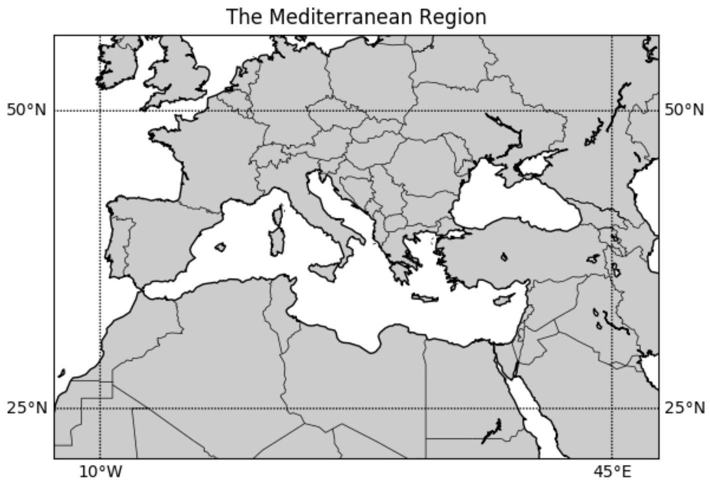

Figure 2.2: The Mediterranean region is shown here with the chosen extents for this study. Here the region spans 25°N - 50°N and 10°W - 45°E.

The Mediterranean Sea is the crucial environmental factor for this region [40]. The size of the Mediterranean Sea is substantial, with an area of about 2.5 million km^2, excluding the Black Sea. It stretches about 3700 km in longitude and 1600 km in latitude and has an average depth of 1500 m [40]. The Strait of Gibraltar on the Western end of the

Mediterranean Sea connects it to the Atlantic Ocean. It is only 14.5 km wide and less than 300 m deep at the shallowest sill. Through this connection the Mediterranean Sea can compensate for water loss due to evaporation. The water entering from the Atlantic Ocean is less salty and normally has a higher temperature than the water flowing out of the Mediterranean Sea [40] .

The Mediterranean region has a complicated morphology and land-sea pattern with many islands and peninsulas, that dived the Mediterranean Sea in many basins which are connected by narrow straits [40]. There are two main basins in the Mediterranean Sea which connected by the Strait of Sicily which are commonly referred to as Western and Eastern Mediterranean. These two basins are roughly the same size and are each made up several subbasins [60].

The morphology on land includes the highest mountain range of Europe with the Alps, reaching a maximum height of 4,800m and several other mountain ranges close to the water [39]. Human activities have profoundly transformed the Mediterranean region over millennia, leaving only 4.7% of the region with its primary vegetation unaltered. The region consists of flat agriculture and forested areas, mountain ridges, and steadily growing urban areas [22]. In the Mediterranean region 34% of population lives in low lying areas within 10m of mean sea level, compared to 10% of the population worldwide [40].

2.2 The Climate in the Mediterranean Region

The term "Mediterranean Climate" is used to describe climates with mild wet winters and warm to hot, dry summers. This climate is found mainly on the west coast of continents between the 30°and 40°latitude [8] [39].

In the commonly used Köppen-Geiger climate classification [54] [37], the Mediterranean climate is defined as a mid-latitude temperate climate with a dry summer season, which can be either warm or hot. These two types are labelled Csa and Csb, respectively, in the Köppen-Geiger classification. Besides the Mediterranean region, these climate classes can be found in the west of the United States, in parts of Chile, on the south-western tip of Africa, and the south-western tip of Australia. The Mediterranean region is geographically unique for having a large marginal and almost completely closed sea on the western side of a large continental area. This serves as a large reservoir of heat and moisture for the region. Although the Mediterranean Sea takes up a significant part of the area, there is no uniform climate for the whole region [40]. Many other climate classes are present in the area according to the Köppen-Geiger classification, while the Csa and Csb classifications apply only to a fraction of the Mediterranean region (Figure 2.3).

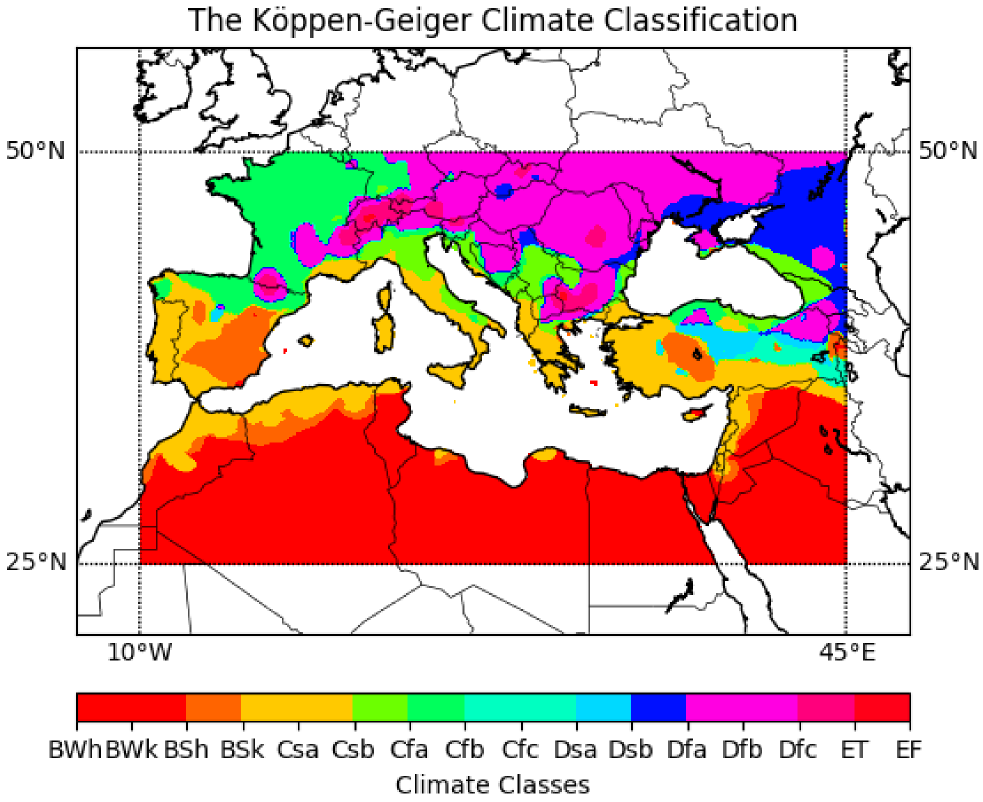

Figure 2.3: Thr Köppen-Geier Classification of the Mediterranean Region is shown here [54][53]. See Table 2.1 for explanation of the abbreviations used in this figure.

The Mediterranean winters are dominated by storms forming over the Atlantic and drawing into the region from the west. Besides the Atlantic storms, there is also the

Abbreviation	**Climate Classification**
BWh	Arid Desert Hot
BWk	Arid Desert Cold
BSh	Arid Steppe Hot
BSk	Arid Steppe Cold
Csa	Temperate Dry Summer Hot Summer
Csb	Temperate Dry Summer Warm Summer
Cfa	Temperate Without dry season Hot Summer
Cfb	Temperate Without dry season Warm Summer
Cfc	Temperate Without dry season Cold Summer
Dsa	Cold Dry Summer Hot Summer
Dsb	Cold Dry Summer Warm Summer
Dfa	Cold Without dry season Hot Summer
Dfb	Cold Without dry season Warm Summer
Dfc	Cold Without dry season Cold Summer
ET	Polar Tundra
EF	Polar Frost

Table 2.1: Köppen-Geier Climate Classes [54] which are present in the Mediterranean region

occurrence of local storms in the Mediterranean region that mostly form on the south side of the Alps. The Mediterranean summer is dominated by high pressure systems causing very dry weather especially in the southern areas of the region [8][23].

Besides these large-scale processes, the climate of the Mediterranean is strongly influenced by local processes which lead to the large climate variability. The variations in climate come from the regions location in a transitional climate zone, between the subtropical zone to the south and the temperate zone to the north, and the complicated morphology of the surrounding land. The area is made up of many sharp mountainous features, often close to the coastlines, and there are distinct basins and gulfs, islands, and peninsulas. This geography has a strong effect on the atmospheric circulation [40].

Even at relatively small spatial scales, the spatial variability of the climate in the region is high, especially when moving away from the coast of the Mediterranean Sea. The distance between most parts of this region and the sea is only a couple of hundred kilometres, but still one can find other temperate, arid, and snow climate types in this relatively small space. Some sites with the highest annual precipitation can be found in the area of the eastern Adriatic coast towards the Alps. On the other hand, extremely dry areas can be found in North Africa at 32°N [40]. The climographs in Figure 2.4 show examples for various climates that can be found in the Mediterranean region as defined in this study. They exemplify the diversity of climates found in the small space of this region.

2.3 Hydrology

Hydrology is literally the science of water, with its etymological roots in Ancient Greek. Hydrology is now defined as the science that deals with the aspects of the cycling of water in the natural environment that relate with the continental water processes and the global water balance [10]

The hydrological cycle (Figure 2.5) describes the circulation of water and includes the spatial and temporal distribution of water in the ocean, atmosphere, and over land. The study of the hydrological cycle is a central part of the Earth's climate at all scales [14]. The hydrological cycle is mainly driven by solar heating which evaporates water from the oceans and land surfaces. The water vapor is transported by wind and eventually condensed to form clouds. This leads to precipitation over land and oceans. Precipitation over land is stored temporarily as snow or soil moisture or runs off in streams and rivers, which eventually discharge the freshwater into the oceans which completes the global water cycle [70].

The two main components of the water cycle are precipitation (P) and evaporation (E). Globally $\mathsf{P} = \mathsf{E}$, but over land-surface we need to introduce run-off (R) which is given by

$$\mathsf{R} = \mathsf{P} - \mathsf{E} \tag{2.1}$$

[10]

The hydrological cycle of the Mediterranean region is largely influenced by the presence of a large semi-enclosed sea. The Mediterranean Sea is characterized by a negative water

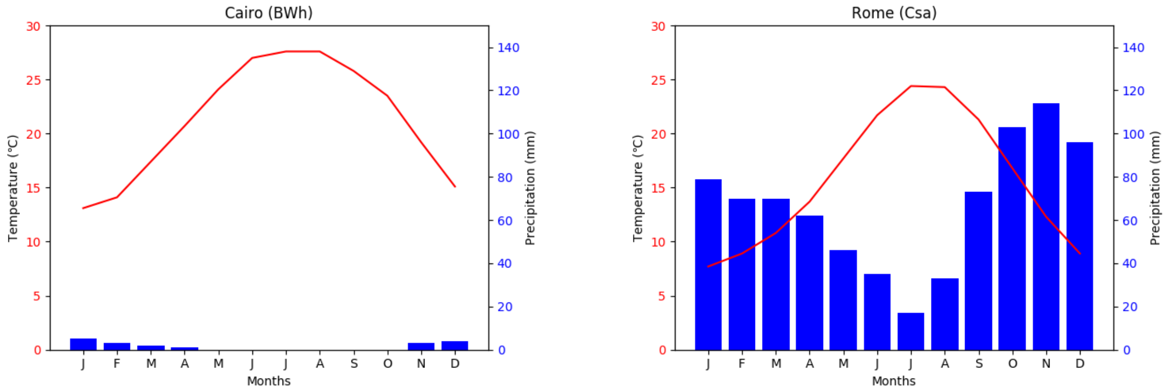

(a) Climograph for Cairo, Egypt (BWh)

(b) Climograph for Rome, Italy (Csa)

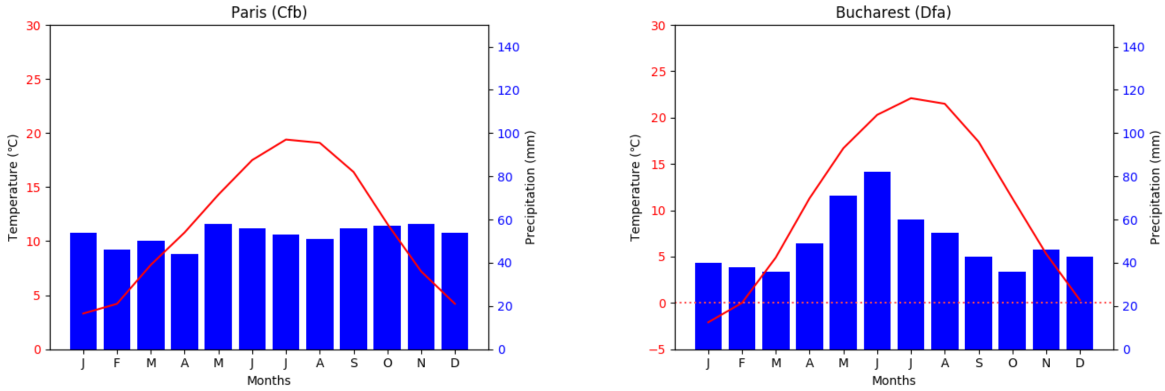

(c) Climograph for Paris, France (Cfb)

(d) Climograph for Bucharest, Romania (Dfa)

Figure 2.4: Four examples for climographs from Köppen-Geiger classified climates within the Mediterranean region as defined in this study. Top left is an example for Arid Desert Hot climate with very low precipitation and high temperatures especially in summer. Top right is an example for Temperate Dry Summer Hot Summer climate with a low in precipitation and a high in temperature in summer. Bottom left is an example for Temperate Without dry season Warm Summer climate with constant precipitation and moderate temperatures with a maximum in Summer. Bottom right is an example for Cold Without dry season Hot Summer climate with a cold winter and high temperatures in summer and a maximum in precipitation in summer.

budget where the excess of evaporation over freshwater input is balanced by the water inflow from the Atlantic. The freshwater input in the Mediterranean Sea is, as described

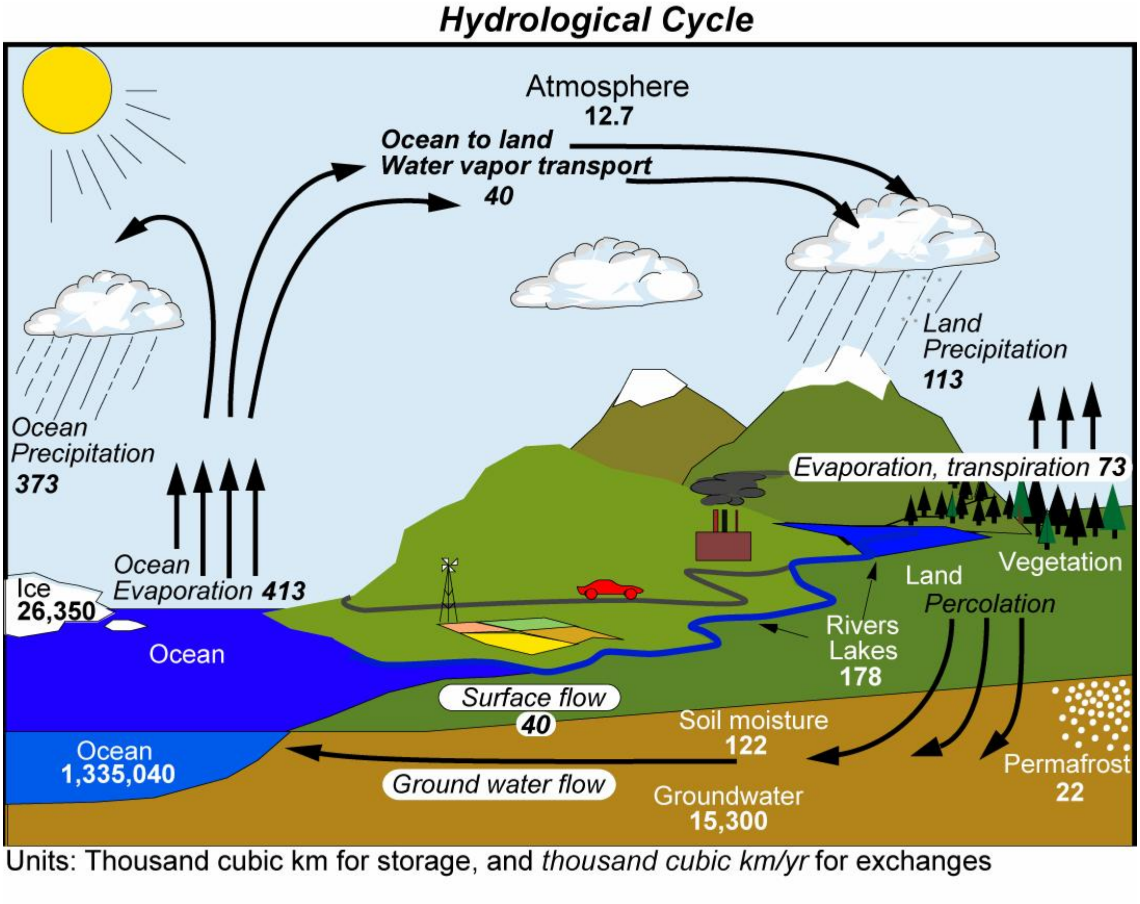

Figure 2.5: This figure shows the hydrological cycle with water changing phase from liquid to solid to gas and back to liquid. The estimated global volume of water stored in each part of the system or exchanged with another part during a year is given in cubic kilometres. This figure was taken from Trenberth et al. (2007) [70]

in the water cycle, given by the river runoff, precipitation over the sea surface, and inflow of the Black Sea water. The river runoff is estimated to account for 160-180 mm/yr of freshwater [40].

The total estimated evaporation from the sea is in the range of 934-1179 mm/yr. In winter months due to the influence of northern dry and cold winds the large evaporation over the sea has its annual high. Precipitation over sea ranges between 331-477 mm/yr [40].

Combining the excess of evaporation and the river input, there is an estimated Mediterranean freshwater deficit of about 480 mm/yr. The deficit should be balanced by the freshwater inflow from the Black Sea and the Atlantic Ocean [40].

Over land the high spatial variability of the climate in the Mediterranean region as describes in Section 2.2, is also reflected by the hydrology of the region. The complex geography plays a crucial role in airflow and consequently in the hydrological cycle. This can lead to the creation of high-impact hydrological weather systems, such as heavy precipitation and flash-flooding or heat-waves with droughts [43]. Besides the local circulation patterns there are also larger processes that lead to hydrometeorological extremes in different parts of the Mediterranean. Especially the eastern Mediterranean is influenced by several tropical processes leading to cloud bands forming over the Red Sea and the Cyprus lows. The western Mediterranean meanwhile is sensitive to the timing and location of winter storms that form over the Atlantic Ocean [43].

In the following subsections, the variables of the hydrological cycle and their importance to the Mediterranean hydrological cycle are briefly introduced.

2.3.1 Precipitation

Precipitation in the Mediterranean shows a latitudinal gradient in all seasons, with an increase in precipitation with increasing latitudes. The mean precipitation along the African coast is about 350 mm/yr while over 750 mm/yr are found in parts of France and along the Alps. Over the sea the western Mediterranean subbasin is drier than the eastern Mediterranean in the annual mean.

Temporal variations in precipitation show very little precipitation in the summer months in most of the Mediterranean region except for the North towards the Alps where we see a maximum in precipitation in the summer months. Besides the minimum in summer, there is a broad maximum in precipitation that extends beyond the conventional winter season from autumn to spring. The largest amounts of precipitation occur from November to January [43].

Interannual fluctuations in precipitation in the Mediterranean region occurred with a variation of about 150mm/yr from the wetter period around 1985 to the drier 1990.

Significant interdecadal changes happend from the mid-1960s to around 1990 where Mediterranean precipitation dropped from 550 mm/yr to 400 mm/yr [43].

Precipitation extremes are local and temporal fluxes in precipitation, they account for 60% of the total precipitation in the Mediterranean region and are more likely to happen over land than over sea. Precipitation extremes have a 5- to 50-year return cycle [40] and can cause floods in the region. Floods and flash floods are very prominent in the Mediterranean area and pose a significant threat. Although they are much more common north of the Mediterranean Sea, they have also occurred along the African coast [16].

2.3.2 Evapotranspiration

Evapotranspiration is a part of the hydrological cycle where liquid water is removed from vegetation and surface and into the atmosphere. This needs two processes of both transpiration and evaporation. While evaporation is the process of liquid water being transformed to water vapour, transpiration is the process when water in plants is lost to the atmosphere.

Evapotranspiration is the second largest component of the hydrological cycle after precipitation and the second largest component in surface energy balance after net radiation. A significant amount of incoming solar radiation is energetically accounted for by evapotranspiration. A reduction in evapotranspiration would therefore lead to higher temperatures [80] [48].

The spatial distribution of evapotranspiration in the Mediterranean region roughly follows the climate classes of the region (Figure 2.3), with lower evapotranspiration in the humid climates in northern Mediterranean region and larger evapotranspiration in the arid climates of the south [69].

When observing solely the evaporation in the Mediterranean region we see the maximum during the winter months mainly because of stronger and drier winds. In summer evaporation is lower in over sea and in the southern Mediterranean while it increases in the north of the basin, towards central eastern Europe [43].

2.3.3 Soil Moisture

Soil Moisture is the water contained in the root zone of the soil where it is available to plants. Although water contained in soil moisture only makes up a very small fraction of the total water on earth, it has a known importance for the environment and climate systems. It influences hydrological and agricultural processes, runoff generation, drought development and many others. Through atmospheric feedback it also has an impact on the climate system. Soil Moisture is involved in both the water and energy cycles as it is the source of evapotranspiration over land [20] [5].

Soil moisture is of great interest in the Mediterranean region due to its direct link to droughts. In the region droughts occur regularly in the summer months especially in more recent years [77]. In the summer, a lack in soil moisture has a limiting effect on evapotranspiration and consequently cloud formation and precipitation in the region [66].

2.3.4 Climate Change Projections in the Mediterranean Region

The increase in mean global air temperature over the past 30 years, linked to the anthropogenic increase of CO2 emissions, is commonly known as climate change and is believed to have a significant impact on global circulation patterns [32]. The location of the Mediterranean region, between the arid climate zone of northern Africa and the temperate and humid climate of Europe, makes the Mediterranean climate especially sensitive to changes in the global circulation [40]. Climate change is therefore expected to have an especially strong impact on the Mediterranean region [32].

In the Mediterranean region, an increase in temperature and decrease in precipitation is expected in results to climate change [40]. It is projected that the warm season will be affected especially with a precipitation decrease between 25-30% and warming exceeding 4-5°C when the 2071-2100 period is compared with the 1961-1990 period. Only in the winter months an increase in precipitation can be expected in some areas of the north, especially in the Alps. An expected increase of inter-annual variability will lead to a greater occurrence of extreme heat and drought events [40]. A rapid drying on the region is expected from 2020 onwards. The drier land surface would then inevitably lead to a decrease in evapotranspiration, but only at half the rate of precipitation [3].

The possible impact of climate change on the Mediterranean Sea is even more dramatic. While precipitation will reduce over sea, evaporation will increase at the same rate. As a result, a 24% increase in loss of freshwater is expected. The inflow from the Black Sea could at the same time decrease leaving an even larger freshwater deficit. This would lead to an increase in salinity and temperature of the surface waters. Consequently, this could have an effect on deep-water formation in the sea basin and the water exchange over the Strait of Gibraltar with the Atlantic Ocean. The changes in the Mediterranean Sea especially the surface waters could in return have a modulating impact on the atmospheric changes in the Mediterranean region [40] [3].

The rivers in the Mediterranean region are also expected to become much drier due to climate change with a decrease in flow up to 85%, only the river Nile might have an increase in river discharge [33].

Among many other studies Drobinsky et al. (2014) [16], Alpert et al. (2013) [3], Quintana Seguí et al. (2010) [56], Jin et al. (2010) [33], Zampieri et al. (2009) [77], Giorgi and Lionello (2008) [23], and Mariotti et al. (2008) [44] show with different climate models that climate change will have a significant impact on the Mediterranean climate and hydrological cycle.

3 Climate Modes

The world's climate is the long-term behaviour and structure of the atmosphere, hydrosphere, and cryosphere. To better understand changes in climate it is important to understand the natural variability in climate. These variabilities in climate follow distinct repeating spatio-temporal patterns that are often described as climate modes or climate oscillations. These patterns can be yearly, diurnal, seasonal, or quasi-periodic cycles. They can be monitored by scalar-valued climate indices, representing them with simple features. In general, the modes describe the spatial structure of two strongly coupled areas, but instead of being spatially independent one can see synchronized behaviour in regions that are far apart [75]. Many different climate oscillations exist around the world with some of the most prominent being the El Niño/Southern Oscillation (ENSO), the NAO, the Pacific Decadal Oscillation (PDO), and the Madden-Julian Oscillation (MJO). Some oscillations are more localised within a smaller region while others affect regions across the globe. Individual oscillations often have several teleconnections to other climate modes leading to correlations between the respective climate oscillation indices [13].

Climate modes are a major driver for hydrology in many regions of the world, including the Mediterranean [46] [17] [24] [6].

In the following sections, the climate modes and their corresponding indices used in this study are introduced, followed by an overview over the existing findings regarding the influence of climate modes on the Mediterranean region. In Table (3.1) a complete list of climate indices used in this study is given. These indices were chosen due to the findings of earlier studies regarding this topic. A more detailed description can be found in Section 3.6.

Climate Oscillation Indices	
AO	Arctic Oscillation
EA	Eastern Atlantic
EAWR	East Atlantic/West Russia
EP-NP	East Pacific - North Pacific
NAO	North Atlantic Oscillation
PNA	Pacific/North America
SOI	Southern Oscillation Index
TNA	Tropical Northern Atlantic
TSA	Tropical Southern Atlantic

Table 3.1: Climate Oscillation Indices used in this study.

3.1 North Atlantic Oscillation Pattern

The NAO is one of the longest known climate patterns, dating back several centuries. The NAO explains the redistribution of atmospheric mass between the Arctic and the subtropical Atlantic and is especially strong in the winter months of the northern hemisphere (November-April). It is known that the NAO has a direct effect on weather phenomenon in the Atlantic and its surrounding continents [31], including the Mediterranean [71].

The NAO consists of two pressure systems. The locations of the pressure systems can vary, but are typically located with the low-pressure system near Iceland and the high-pressure system over the Azores. During a positive winter NAO (see Figure 3.1), the Icelandic low and Azores high are strengthened and result in warm moist air coming from the Atlantic towards Europe through the strengthened westerlies jet stream. While a negative NAO indicates a weakening of the Icelandic low and Azores high which weakens the westerlies and causes cold dry air to come into Europe from the east [67].

The NAO relates to hydrological processes: Spencer and Essery (2016)[67] showed the connection between the NAO and the snow cover in Scotland. Salgueito et al. (2013)[63]

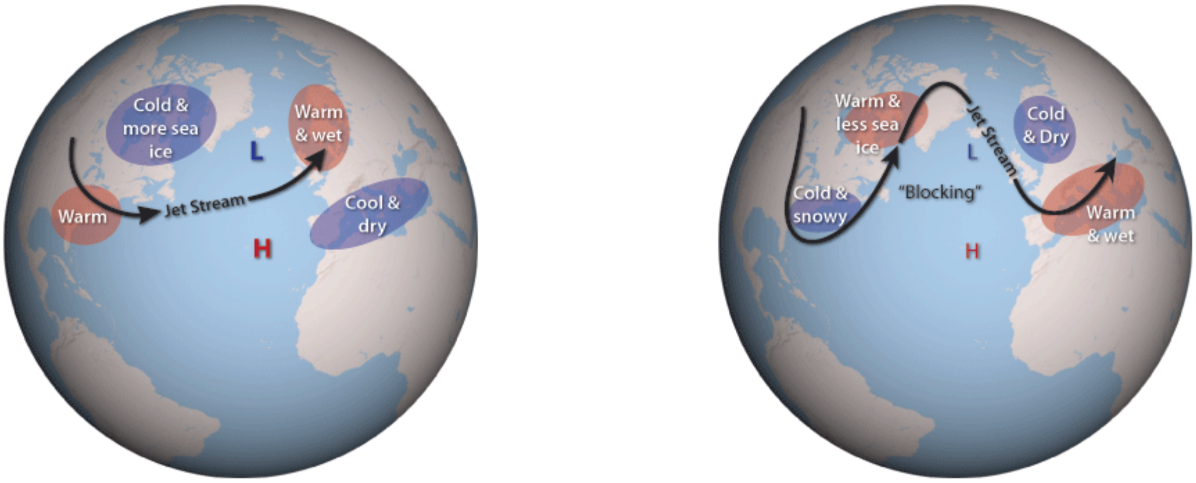

(a) Positive NAO.

(b) Negative NAO.

Figure 3.1: On the left, a positive NAO is shown with a strong Icelandic low and Azores high resulting in warm and wet air coming from the Atlantic to Europe. The right image shows the weakening of both pressure systems during a negative NAO leading to cold and dry air coming from the North to Europe. Graphics from the MetOffice, United Kingdom (http://www.metoffice.gov.uk/learning/learn-about-the-weather/north-atlantic-oscillation)

found a stochastic relationship of flood magnitudes in the Tagus River with the NAO. And Kahya (2011)[35] discusses the impacts of NAO on the hydrology of the eastern Mediterranean region.

North Atlantic Oscillation Index The NAO Index is the difference of normalized Sea Level Pressure (SLP) between Lisbon, Portugal and Stykkisholmore/Reykjavik, Iceland. The SLP values at each station are normalized by removing the long-term mean and by dividing be the long-term standard deviation. Additional normalizations are used to avoid the series being dominated by the greater variability of the northern station.

Instead of using the station based NAO index as it may not be the best representation of the associated pattern, EOF analysis can be used. In this case, the leading EOF mode of the seasonal (December to March) SLP anomalies over the Atlantic sector (20°- 80°N, 90°W- 40°E) are used.

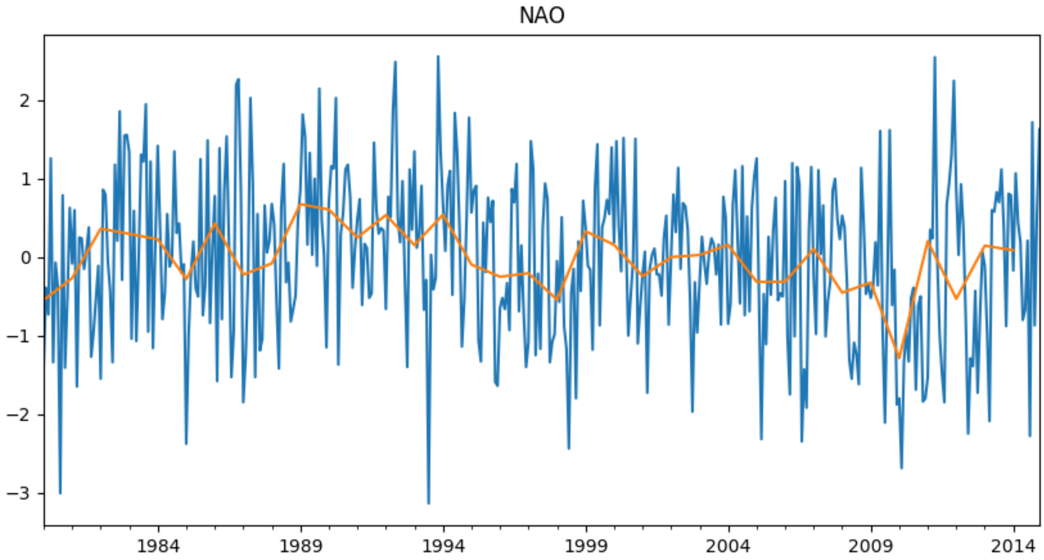

Figure 3.2: North Atlantic Oscillation Index for 1980-2014 with monthly values shown in blue and the annual average in red.

3.2 Tropical North Atlantic Pattern

The Tropical North Atlantic Pattern together with the Tropical South Atlantic Pattern make up the Atlantic meridional gradient mode [74]. Together they form a dipole and are indicators for the Sea Surface Temperature (SST) of the tropical Atlantic [18]. Both TNA and Tropical Southern Atlantic (TSA) are associated with variations of the Hadley circulation [74].

The TNA is believed to be closely linked to the ENSO [74] [4]. The NAO and TNA also show a connection where a positive TNA is associated with a negative phase of the NAO [57] [11].

Tropical North Atlantic Index The TNA Index is calculated with SST measurements within the 55°W - 15°W and 5°N - 25°N bounding box. It uses the standardized average of the monthly SST anomalies over the tropical north Atlantic region [11].

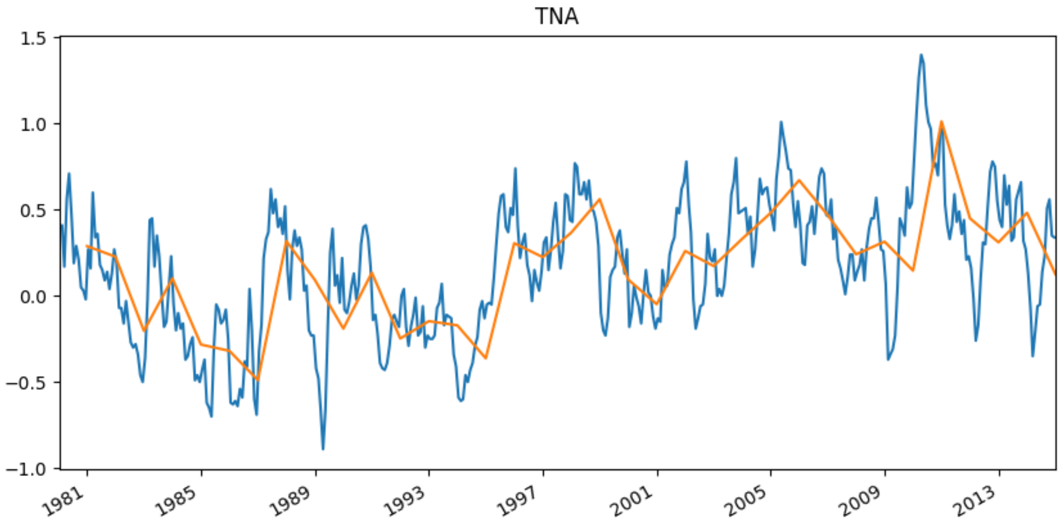

Figure 3.3: Tropical North Atlantic Index for 1980-2014 with monthly values shown in blue and the annual average in red.

3.3 Eastern Atlantic Pattern

The Eastern Atlantic Pattern is said to be the second leading climate mode in the North Atlantic and has a significant impact on the structure of the NAO including changes in location and intensity [49]. It consists of a north-south dipole of anomaly centres spanning the North Atlantic from east to west resembling the NAO with a southward shift. Unlike the NAO, the EA shows a strong subtropical link for the lower-latitude centre which makes it distinct from the NAO.

A positive phase of the EA results in higher temperatures in Europe in all months and seasonally depended low temperatures in the United States. It is also associated with higher precipitation in Northern Europe and lower precipitation in Southern Europe [73].

The EA has multi-decadal variability, with a negative EA during 1950-1976 and a positive EA during 1977-2004 with a particularly strong positive during 1997 and 2004. In recent years the EA has again been strongly positive since 2012.

Eastern Atlantic Index Unlike the NAO index, the EA index is not as well established and its pattern depends heavily on the methods used to calculate it [71]. The most commonly used definition of the EA index comes from Wallace et al. (1981) [73] and the EA index used in this study also follows this definition.

The EA Index is based on normalized 500 hPa height anomalies at three specific centres. One is located south west of the Canary Islands, another west of Great Britain, and the third near the Black Sea. A positive pattern index indicates a high 500 hPa height over the North Atlantic low heights over the subtropical Atlantic and eastern Europe. A negative pattern index indicates the opposite [73].

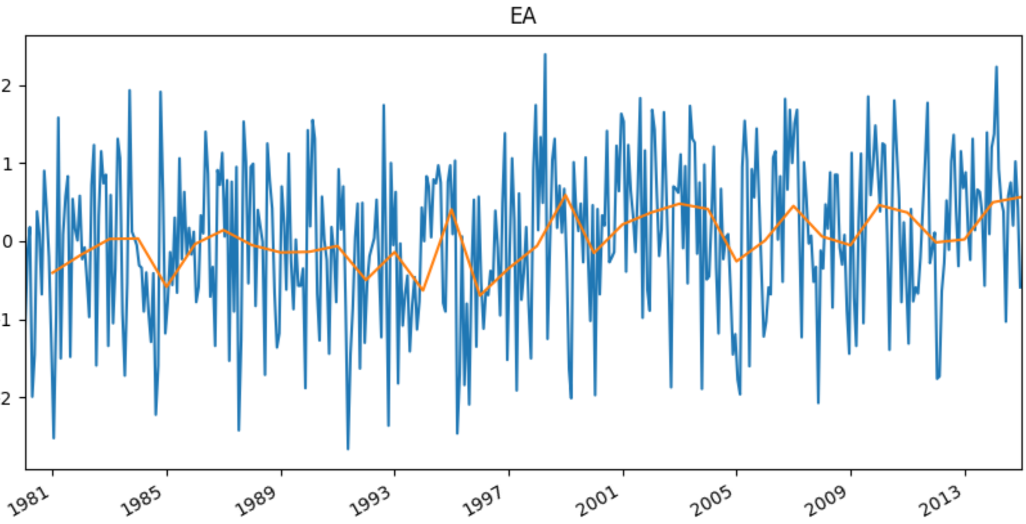

Figure 3.4: Eastern Atlantic Index for 1980-2014 with monthly values shown in blue and the annual average in red.

3.4 Arctic Oscillation Pattern

The Arctic Oscillation pattern is characterized by winds circulating around the Arctic. The AO resembles with the NAO strongly, but still shows distinct differences. The AO centres more on the Arctic, making it more zonally symmetric [68].

In a positive phase of the AO the cold air is confined by high pressure in the Arctic which causes the rest of the northern hemisphere to be warmer. In a negative phase, the weaker pressure system allows the cold air to move south, causing the northern hemisphere to be colder (Figure 3.5).

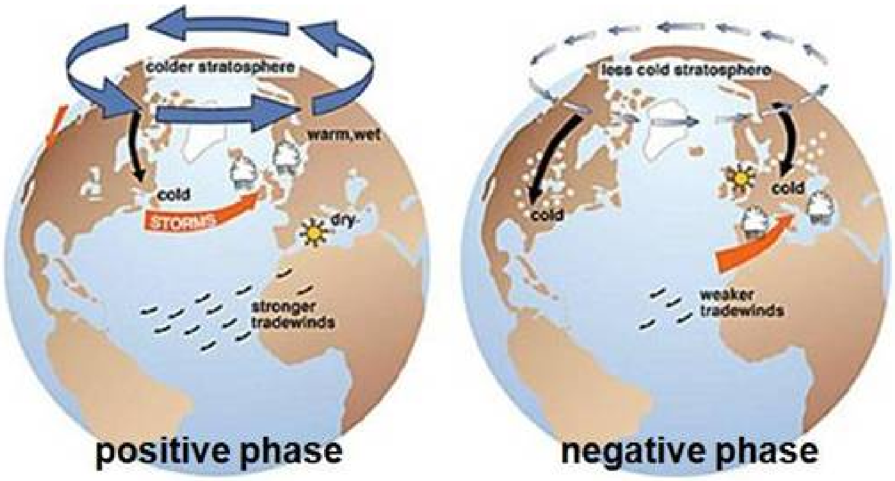

Figure 3.5: The effects of a positive and negative Arctic Oscillation pattern are shown here. A positive phase results in dry and warm weather in the Mediterranean area whereas a negative phase causes cold and wet weather in this area.

Arctic Oscillation Index The AO Index is derived from the monthly mean 1000 hPa height anomalies across the Arctic poleward of 20°N using EOF analysis. The first leading mode of the EOF analysis is the temporal pattern of AO. To obtain the temporal pattern, a year-round monthly mean anomaly data is used. The AO has the largest variability in the winter months and the principal components therefore primarily show the characteristics of the cold season patterns.

3.5 El Niño Southern Oscillation

The Niño Southern Oscillation (ENSO) is a climate phenomenon that involves fluctuating ocean temperatures in the equatorial Pacific. The pattern generally fluctuates between two states: warmer than normal eastern equatorial Pacific SST (El Niño) and cooler than normal eastern equatorial Pacific SST (La Niña). The terms El Niño and

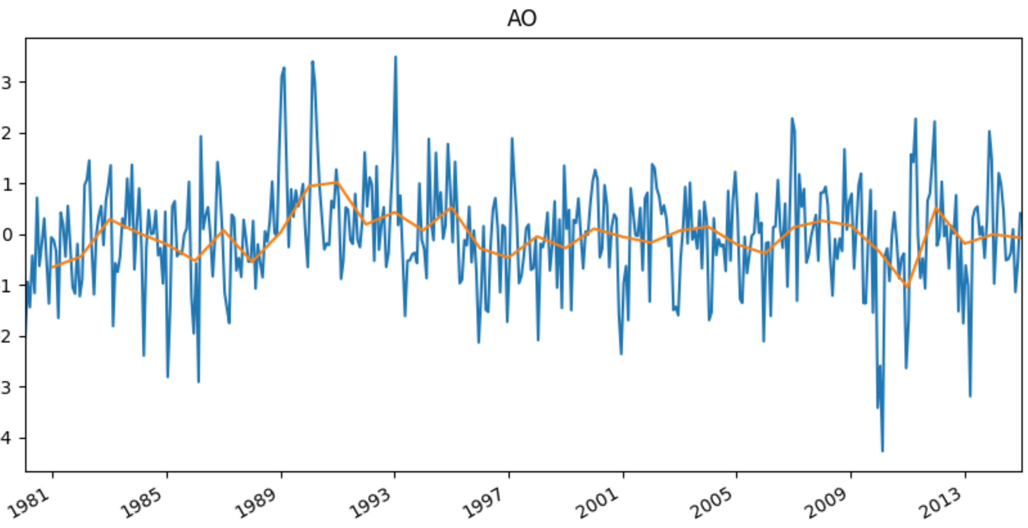

Figure 3.6: Arctic Oscillation Index for 1980-2014 with monthly values shown in blue and the annual average in red.

La Niña originate from the (Spanish speaking) Christian inhabitants of South America who celebrate Christmas around the time when the phenomenon usually reaches its full strength. ENSO is the most important coupled ocean-atmosphere phenomenon to cause global climate variability on interannual scales [9] [5].

ENSO has a significant impact on the pacific region in terms of rainfall, drought and tropical cyclone behaviour, but via teleconnection it has an impact many parts of the world especially in the tropics. During an El Niño event which usually lasts for one year, the trade winds weaken, which are the drivers for ocean upwelling in the eastern tropical Pacific. As a consequence, SST rise as much as 5°C above normal and surface ocean currents are altered. This weakens trade wind even more, introducing a positive feedback mechanism [9].

There is a large number of known ENSO-teleconnections to the North Pacific and Indian Ocean. Brönnimann (2007) also describes a significant effect of El Niño on European climate which appears to be closely linked through the NAO [9].

Southern Oscillation Index The Southern Oscillation Index (SOI) index is derived from observations of the sea level pressure at stations in Darwin, Australia and Tahiti. The SOI is the standardized difference between the two atmospheric pressures. SOI is used to quantify the strength of an ENSO event. Normally, lower pressure over Darwin and higher pressure over Tahiti encourages a circulation of air from east to west, indicating strong trade winds. A weaker pressure difference is strongly coincidental with El Niño conditions.

The SOI used in this study is the Troup SOI which is the standardised anomaly of the Mean Sea Level Pressure difference between Tahiti and Darwin, Australia (Figure 3.7).

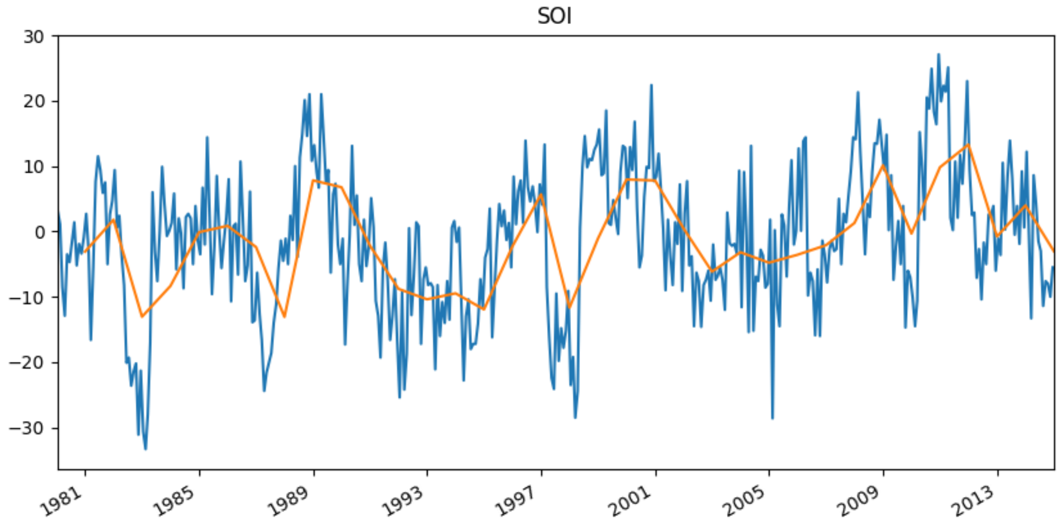

Figure 3.7: Southern Oscillation Index for 1980-2014 with monthly values shown in blue and the annual average in red.

3.6 Influence of Climate Modes in the Region

As described in Chapter 2, the location of the Mediterranean region in the transition zone causes the local climate to be influences by both the mid-latitudes and tropical climate variability. In the north-west a large part of the variability is linked to the NAO and other midlatitude teleconnections patterns [16] especially the EA [40] while in the south the influence of the descending branch of the Hadley cell in the form of the Azores high is dominating. The Hadley cell is a primary circulation cell that lies between the equator and 30-40°latitude. Warm air rises near the equator and is transported polewards and then descends in the subtropics causing high pressure systems. The east is influenced by the ENSO [16], especially winter precipitation [40].

The influence of mid-latitude variability is greatest during winter season in the Mediterranean. As the region is at the southern limit of North Atlantic storm tracks it is especially sensitive to slight changes in the trajectories of mid-latitude cyclones. Storm impact variability has the strongest influence in the western Mediterranean, but also shows in the eastern part. [71]

In the Mediterranean region, the NAO is known to have a strong impact on precipitation in the winter months. This can be seen in both eastern and western Mediterranean, but the impact is stronger in the west. Interestingly, the NAO has an influence on precipitation but does not have an impact temperature or evapotranspiration [71].There exist many studies on the influence of the NAO on the Mediterranean region. For example Salgueiro et al. (2013) [63], Kahya (2011) [35], López-Moreno et al. (2011) [41], Queralt et al. (2009) [55], all study the impact of the NAO on the Mediterranean.

While the impact of the EA on the Mediterranean climate is not as well studied as of the NAO, there is still evidence for variability associated with this pattern. Sáenz et al. (2001) shows a significant impact of the EA on winter precipitation [61] and temperature [62] over the Iberian Peninsula. Salmaso (2012) [64] shows an influence of the EA on freshwater ecosystems in the Mediterranean and the Alps. These ecosystems are impacted by changes in temperature due to positive or negative phases of the EA. More recently, Cook et al. (2016) [12] shows the impact of spring EA variability on droughts in the Mediterranean area.

There exist many studies trying to quantify the impact of other climate modes on the climate in the Mediterranean area. Alpert et al. (2006) [2] discusses the relation between the climate variability in the Mediterranean region and the ENSO and monsoons. Martínez-Asensio et al. (2014) [46] discover connections between the Mediterranean sea level to the climate modes. Capa-Morocho et al. (2016) [11] finds correlation between the TNA and water availability for crop growth in the Iberian Peninsula.

4 Data

The data for this thesis was gathered for the WACMOS-MED (Water Cycle Observation Multi-mission Strategy for Mediterranean) project [19] of the European Space Agency (ESA). The project aims at a better understanding and quantification of the hydrological cycle in the Mediterranean by using ESA and non-ESA earth observation datasets. The datasets used, span different origins and time scales, but share a common extent over the Mediterranean region. The datasets are exclusively raster datasets and are stored in NetCDF files. The grid size varies in size and was a coarse as 2.5°x 2.5°for some datasets and as fine as 0.5°x 0.5°grids. The timespan of the datasets varies between ten to more than 30 years spanning from the 1980s to the 2010s. Although the temporal resolution also varies between 3 hourly and monthly, in this study the datasets are being resampled to either monthly or seasonal data before EOF analysis is applied. In the following sections, the different datasets listed in the table 4.1, are briefly introduced and explained.

4.1 Precipitation

Precipitation is often not highly correlated in space and time, but can be scattered in space and discontinuous in time. This is especially true for small scales and many location on earth, including the Mediterranean region. Even with the near-global coverage of satellites, most satellites fly over a region only twice per day, potentially missing precipitation events.

For this reason, many data sets combine observations from multiple satellite platforms that carry passive microwave and/or infrared instruments. Infrared sensors are used to

Dataset	**Type**	**Time Span**	**Temporal Res.**	**Spatial Resolution**
Global Precipitation Climatology Project (GPCP)	Precipitation	1996 - 2015	daily	1°x1°
CPC MORPHing technique (CMORPH)	Precipitation	1998 - 2015	3 hourly	0.25°x0.25°
TRMM Multi-satellite Precipitation Analysis (TRMM-TMPA)	Precipitation	1998 - 2014	3 hourly	0.25°x0.25°
Global Land Evaporation Amsterdam Model Version 3 (GLEAM v3)	Evapotranspiration	1980 - 2012	daily	0.25°x0.25°
MODIS 16 - Evapotranspiration (MODIS16)	Evapotranspiration	2001 - 2014	monthly	0.05°x0.05°
Penman-Monteith-Leuning Evapotranspiration (PML-ET)	Evapotranspiration	1981 - 2012	monthly	0.5°x0.5°
Priestley–Taylor Jet Propulsion Laboratory (PT-JPL)	Evapotranspiration	1984 - 2006	monthly	1°x1°
Numerical Terradynamic Simulation Group (NTSG)	Evapotranspiration	1983 - 2006	monthly	1°x1°
Climate Change Initiative (CCI)	Soil Moisture	1980 - 2015	daily	0.25°x0.25°

Table 4.1: Datasets used in this study with their type and time span and their original Temporal and Spatial Resolution.

estimate cloud top temperatures, which must be calibrated to some other precipitation estimate. The microwave-based algorithms derive the precipitation signal from both scattering and emission, but only the scattering signal is useful over land because of strong variations in surface emissivity that distort the emission [51].

4.1.1 GPCP

The GPCP monthly precipitation dataset from 1979 - today combines observations and satellite precipitation data into 1°x1°global grids. It has been in existence for over twenty years as part of the Global Energy and Water Cycle Exchanges (GEWEX) effort under the World Climate Research Program (WCRP). The GPCP monthly product integrates several satellite data sets over land and ocean and a gauge analysis over land for a consistent analysis of global precipitation. To estimate the monthly rainfall on the 1°grid, data from the rain gauge stations, satellites, and sounding observations are merged. By combining several satellite-based rainfall estimates the GPCP monthly product is the most complete analysis of rainfall available covering the entire planet [52] [1].

4.1.2 CMORPH

The CMORPH data set is a high temporal and spatial resolution data set with a spatial resolution of 0.25°x 0.25°and a temporal resolution of 30 minutes. The data set includes data from 2002 to today. The CPC MORPHing technique uses precipitation estimates that have been derived from low orbiter satellite microwave observations exclusively. Their features are transported via spatial propagation information that is obtained entirely from geostationary satellite IR data [34].

4.1.3 TRMM-TMPA

The Tropical Rainfall Measuring Mission (TRMM) was a joint space mission between NASA and Japan's National Space Development Agency designed to monitor and study tropical and subtropical precipitation and the associated release of energy. The TRMM-TMPA data set with monthly precipitation averages was the most relevant TRMM data set. It has a resolution of 0.25°x 0.25°for 1998 to 2015. The TRMM-TMPA combines microwave data from multiple satellites while coverage gaps in space and time are filled in with calibrated infra-red data [30].

4.2 Evapotranspiration

The observation of evapotranspiration is difficult, as it cannot be sensed directly from satellites and therefore remains the part of the hydrological cycle with the largest uncertainties. As the understanding of the importance to measure evapotranspiration to better understand the hydrological cycle increases, more in situ networks have been created and models to utilize a combination of remotely sensed drivers of evapotranspiration have been developed [45].

4.2.1 GLEAM v3

GLEAM v3 [47] is a set of algorithms dedicated to the estimation of evapotranspiration and root-zone soil moisture from satellite data by separately estimating the different components of evapotranspiration. It also assimilates the components of evapotranspiration (e.g. precipitation, soil moisture, radiance, vegetation stress, etc.) [45]. The dataset has been developed in 2011 and spans 36 years from 1980 to 2015 with a temporal resolution of one day. In this thesis, the dataset spanning 1980 - 2012 was used.

4.2.2 MODIS16

The MODIS16 evapotranspiration dataset is based on the data from the MODerate-resolution Imaging Spectroradiometer (MODIS) which is a key instrument on the Terra and Aqua satellites from National Space Agency (NASA). The dataset is a regular 0.05°grid land surface evapotranspiration dataset for the global vegetated land areas at

8-day, monthly and annual intervals. The dataset spans the time period of 2000 - 2010 [50].

4.2.3 PML-ET

The PML-ET evapotranspiration dataset was computed through the observation-driven Penman-Monteith-Leuning model. The dataset spans 1981 to 2006 with monthly data. It has a spatial resolution of 0.5°[80].

4.2.4 PT-JPL

The dataset is based on the Priestley–Taylor Jet Propulsion Laboratory (PT-JPL) model. The evapotranspiration dataset based on the PT-JPL algorithm comes in a 1°grid with monthly data for the time span of 1984-2006 [21].

4.2.5 NTSG

The dataset of the NTSG is based on a remote sensing based evapotranspiration algorithm in order to assess terrestrial evapotranspiration. Like other datasets, it uses a modification of the Penman-Moneith approach to estimate the soil evaporation and the open water evaporation with a Priestly-Taylor approach. The NTSG dataset spans 1983 to 2006 and has a temporal resolution of one month. The spatial resolution is 1°[79] [78].

4.3 Soil Moisture

There are several techniques to measure the soil moisture. For in-situ measurements electric devices that measure the conductivity of the soil, which can be converted to soil moisture with a model. Since in-situ measurements of soil moisture are expensive and the individual stations are often poorly distributed, remote sensing is preferred for large spatial coverage. Spaceborne microwave sensors have proven ability to determine soil moisture on a global scale. Both passive and active microwave systems are suitable for soil moisture measuring as both emission and scattering properties of soil are strongly influenced by the soil's permittivity [5]. For retrieving soil moisture, it is necessary to have models that are capable of accounting for vegetation and surface roughness effects on the microwave signal and then convert accordingly the received intensity to soil moisture values [5].

4.3.1 CCI Soil Moisture

The CCI Soil Moisture dataset is part of the CCI programme of ESA. The CCI program seeks to contribute to data bases collecting essential climate variables for the Global Climate Observing System and other international parties. For soil moisture retrieval, the CCI project uses C-band scatterometers (ERS-1/2 scatterometer, METOP Advanced Scatterometer) and multi-frequency radiometers (SMMR, SSM/I, TMI, AMSR-E, Windsat) [15][20].

5 Methods

This chapter explores the methods used in this thesis. First an overview over the study setup is given. It is followed by a detailed description of the EOF Analysis and relevant variations of it. Finally Spearman Rank Correlation Analysis is introduced as the correlation method used in this thesis.

5.1 Study Setup

In this section, the overall data structure of all results of this study are described for better understanding of the full extent of the study. This description uses tree graphs to visualize the data structure level by level. A complete tree graph of the data structure was omitted due to the high number of variations and branches.

All results are clustered in two geographic study areas: the Mediterranean region and the Mediterranean basin.

Figure 5.1: Data Structure Tree 1: The Results are clustered in two geographic study areas

For each study area, all datasets (see Chapter 4) that were available in this study were analysed separately. Table 4.1 presents a complete list of the used datasets.

These datasets are re-sampled for either monthly or seasonal values.

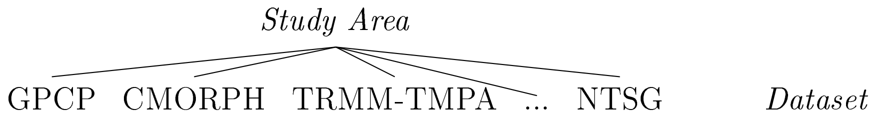

Figure 5.2: Data Structure Tree 2: For each study area, 9 different datasets (see Table 4.1) was used.

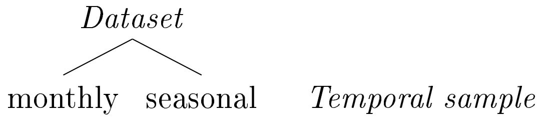

Figure 5.3: Data Structure Tree 3: Each dataset was re-sampled for both monthly and seasonal values.

For each temporal sample, the analysis was done using either EOF or Complex Empirical Orthogonal Functions (CEOF). The differences in the analysis are described in Section 5.2 and Section 5.3.1 respectively.

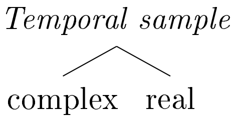

Figure 5.4: Data Structure Tree 4: For each temporal sampling of the datasets EOF and CEOF analysis was applied.

Following the EOF or CEOF analysis, a rotation (see Section 6.1.2) was applied to the results. Either the varimax criterion for an orthogonal rotation or the quartimin criterion for an oblique rotation was used to determine the rotation matrix. For comparison, the not rotated results were also used in further steps of the study.

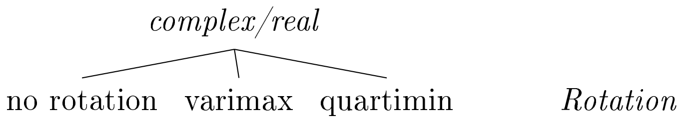

Figure 5.5: Data Structure Tree 5: After the analysis, a rotation was possibly added. There was either no rotation or the varimax or quartimin criterion was used to determine the rotation matrix

Following the (possible) rotation the results were correlated with climate modes (see Chapter 3). The set up for the correlations depends on whether the dataset was re-sampled for monthly or seasonal values. The correlation was done using all possible values from the result (for each month or each season) and also the results were correlated using only the values for one month (Jan, Feb, ..., Dec) or season (DJF / **D**ecember-**J**anuary-**F**ebruary, MAM / **M**arch-**A**pril-**M**ay, JJA / **J**une-**J**uly-**A**ugust, SON / **S**eptember-**O**ctober-**N**ov) independently.

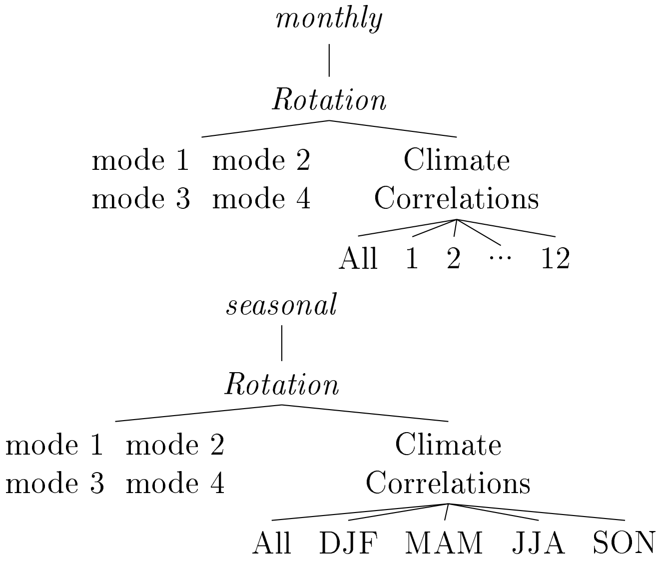

Figure 5.6: Data Structure Tree 6: Depending on the temporal sampling the climate correlations are either done by month or by season. Also, the plots of the first 4 modes of the analysis are outputted.

Further, in case CEOF was applied, the results were correlated using either the amplitude, the real part, or the imaginary part of the complex value. This leads to three different correlation results.

In case of standard EOF analysis, there is no need to differentiate in the correlation. For each of these results a correlation matrix was created out of all four modes and the climate modes (for example see Figure 6.6) and for each of these correlations a separate graph showing both the EOF / CEOF results and the climate mode time series for the same time span. This leads to a total of 36 graphs per correlation calculation.

This study set-up allowed the specific creation of a set of graphic outputs through the settings. In the course of this study not all possible outputs were created for each dataset as this would have exceeded the capacity of this study, instead all settings were

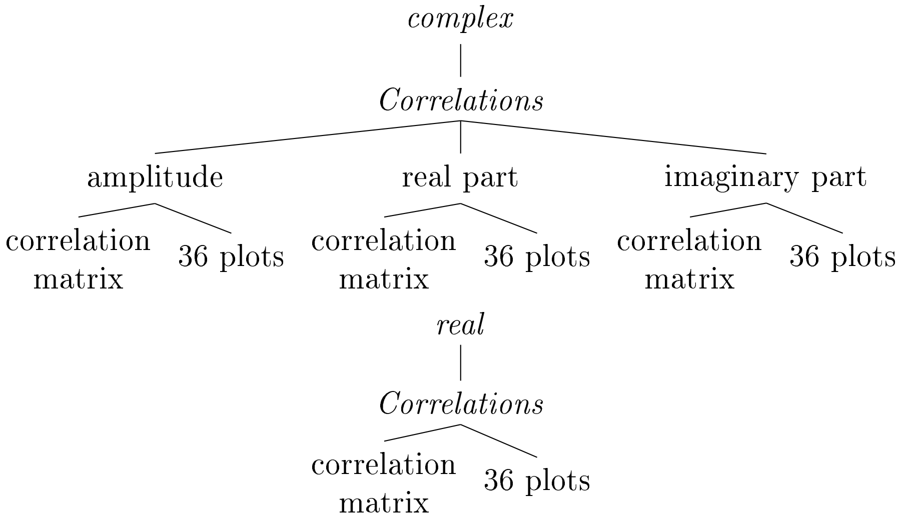

Figure 5.7: Data Structure Tree 7: For CEOF the results are correlated with the climate modes by amplitude, real part, and imaginary part. The climate correlations have an output of a correlation matrix and 36 individual plots of all correlations between the first four modes of the analysis and the 9 climate indices.

tested and the most successful ones applied to all datasets. The code can also be easily adapted to include more variations on EOF analysis or to run with a different dataset or a different study area.

5.2 Empirical Orthogonal Functions

In this section, Empirical Orthogonal Functions (EOF) are introduced. This method is also known as Principal Component Analysis (PCA) and either name is used in different scientific disciplines. The method was originally used in social science at the beginning of the 20th century. EOF is a versatile exploratory method for numerical datasets as it enables the display of a space-time field as a time display and a space display. There exist many implementations, so that it has been used for very diverse applications [27]. In atmospheric science EOF is a widely used statistical method [27] and was first termed in this field by Lorenz (1956) [42] who applied EOF to weather data. The method was chosen for this thesis as it is suitable for the extraction of climate signals from large datasets and well-tested in this field.

For a given space-time field, EOF analysis finds a set of orthogonal spatial patterns along with a set of associated uncorrelated time series or Principal Components (PC) . In Figure 5.8 EOF Analysis is schematically pictured.

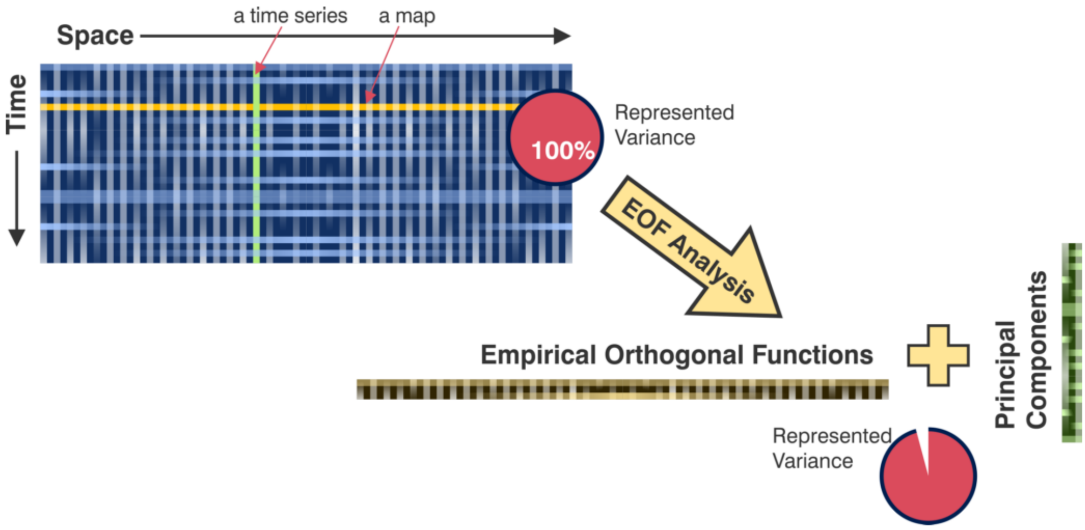

Figure 5.8: Schematic representation of the EOF analysis [5]

The following summary of the method comes from Hannachi (2007) [27] and the notation has been taken from Bauer-Marschallinger (2012) [5].

The base idea of EOF is to separate a space-time field into a space and a time field:

$$X(t,s) = \sum_{k=1}^{M} c_k(t) u_k(s) \tag{5.1}$$

Where M is the total number of functions (modes) that are contained in the dataset (field). The field $X(t,s)$ is split up into the basic functions of space $u_k(s)$ and the expansion functions of time $c_k(t)$ [27]. When using EOF analysis the main idea is to get uncorrelated, independent, representative representations of the entire dataset, while keeping the number of modes M significantly lower than the total number of available modes. This is done to simplify the dataset and to focus on a handful of modes that explain a lot of total variability of the dataset. [5]

To compute EOFs we start with a spatio-temporal field $X(t, s)$ which shows the value of the field X for time t and location s. The dataset can be noted as a matrix X:

$$X(t, s) = \{x_1, x_2, ...x_{\mathcal{T}}\}^T = \begin{pmatrix} x_{1,1} & x_{1,2} & \cdots & x_{1,\mathcal{S}} \\ x_{2,1} & x_{2,2} & \cdots & x_{2,\mathcal{S}} \\ \vdots & \vdots & \ddots & \vdots \\ x_{\mathcal{T},1} & x_{\mathcal{T},2} & \cdots & x_{\mathcal{T},\mathcal{S}} \end{pmatrix} \tag{5.2}$$

In the matrix, the row-vectors in the matrix $x_t = (x_{t1}, x_{t2}, ..., x_{t\mathcal{S}})^T$ are the value (or the map) of the field at times t and the column-vectors in the matrix $x_s = (x_{1s}, x_{2s}, ..., x_{\mathcal{T}s})$ are the time series at locations s. The indexing in time is $t = 1, 2, ..., \mathcal{T}$, in space the indices are $s = 1, 2, ..., \mathcal{S}$. In this study, all datasets are considered to contain more spatial than temporal variables, meaning $\mathcal{S} > \mathcal{T}$.

For the EOF analysis the anomalies x', of the values in the dataset are used to eliminate the impact of the actual size or unit of the original values. To get the anomalies the mean of each time series is calculated and the subtracted from the individual values of that time series:

$$\bar{x}_s = \frac{1}{\mathcal{T}} \sum_{\mathcal{T}}^{k=1} x_{ks} \tag{5.3}$$

$$x'_{ts} = x_{ts} - \bar{x}_s \tag{5.4}$$

As an alternative to anomalies climatology values can be used. Here the average is calculated by only using values for a certain time span e.g. for a monthly climatology the average is calculated for each month separately and then deducted from the individual values of each month. This is a very common approach in atmospheric science [27] [5]

$$\bar{c}_s = \frac{1}{\mathcal{P}} \sum_{k=1}^{\mathcal{P}} x_{ks} \tag{5.5}$$

$$x'_{ts} = x_{ts} - \bar{c}_s \tag{5.6}$$

For simpler notation, the dash of the anomalies will be dropped and x' will be x in the following.

In case the data is stored in a regular geographic grid defined by latitudes and longitudes, it is recommended by Hannachi et al. (2006) [26] to weigh the values to account for the actual area represented by a grid cell at location s. The time series in the data matrix X are therefore multiplied by latitudinal weights w_s that depend on the latitude φ_s of the location.

$$w_s = \sqrt{\cos \varphi_s} \tag{5.7}$$

As a next step, the sample covariance matrix is assembled. It contains the covariance between the time series of any pair of grid points (s_i, s_j):

$$sij = [S]_{ij} = \frac{1}{\mathcal{T}} \sum_{t=1}^{\mathcal{T}} x_{ti} x_{tj} \tag{5.8}$$

or in matrix notation:

$$S = \frac{1}{\mathcal{T}} X^T X. \tag{5.9}$$

The diagonal of the covariance matrix S holds the sample variances of the S spatial elements of the dataset X. The covariances can be found in the off-diagonal positions in the matrix. In case a correlation analysis is wanted, this empirical covariance matrix is replaced by a empirical correlation matrix. A correlation matrix is created when the anomalies are divided by the standard deviation of the time series samples in the beginning, like suggested by Wilks (2011) [76]. This is recommended if different units or physical parameters are used in the original dataset, which would distort the numerical conditions of the calculations.

Computation of EOFs from Eigenvalue Analysis The aim of EOF analysis is to find uncorrelated linear combinations (the modes) of the different variables that explain maximum variances. To achieve this, the vectors $e = (e1, e_2, ..., e_S)^T$, which point in the directions of maximum variability, need to be found. With e having the unit-length, Xe has the maximum variability, which further yields:

$$\max\ (e^T S e) \text{ with } e^T e = 1 \tag{5.10}$$

This leads to the following eigenvalue problem:

$$Se = \lambda^2 e \tag{5.11}$$

where the eigenvectors e_k and the eigenvalues λ_k of the k'the EOF have to be found:

$$\lambda_k^2 = e_k^T S e = \frac{1}{\mathcal{T}} \|X e_k\|^2 \tag{5.12}$$

The eigenvalues describe the variance of the data that is accounted for in the corresponding eigenvectors. The eigenvalues are sorted in decreasing order as $|\lambda_1| \geqslant |\lambda_1| \geqslant ... \geqslant |\lambda_S|$. Which leads to the first eigenvector having the highest variance and then the second eigenvalue describing the variance of the second eigenvector and so forth. The spectrum of the covariance matrix S which is made up of the eigenvalues λ_k provide information of the distribution of variation and separation of the EOF patterns. The sum of all eigenvalues equals one if all modes explain the total variability:

$$\sum_{k=1}^{S} \lambda_k = 1 \tag{5.13}$$

It is common to present the variance of a mode in percent of the total variability:

$$\frac{100\lambda_k}{\sum_{k=1}^{S} \lambda_k} \% \tag{5.14}$$

Finally, the anomaly field X is projected onto the EOFs. The results are the k Principal Components (PCs) p_k of the data field X:

$$p_{tk} = \sum_{j=1}^{S} x_{tj} e_{kj} \tag{5.15}$$

or in Matrix notation:

$$\mathbf{p}_k = X\mathbf{e}_k \tag{5.16}$$

With this, Equation (5.1) and therefore our initial problem has been solved and the principal components of the dataset $X(t, s)$ can be calculated. Equation (5.1) and Equation (5.15) have the same structure and describe the same dataset. The time function $c_k(t)$ and the space function $u_k(s)$ correspond to x_{tj} and u_{kj}, respectively. [27] [5]

Computation of EOFs from Singular Value Decomposition Singular Value Decomposition (SVD) can be used alternatively for the determination of the covariance matrix and eigenvectors as described above. It is a very powerful tool from linear algebra [27]. Every $\mathcal{T} \times \mathcal{S}$ matrix X can be decomposed as:

$$X = P\Sigma E^T \tag{5.17}$$

In (5.17) P and E are respectively $\mathcal{T} \times r$ and $r \times \mathcal{S}$ unitary matrices ($P^T P = E^T E = I_r$) with $r = \mathrm{rank}(X)$ and $r \leqslant \min(\mathcal{T}, \mathcal{S})$. I_r is therefore the identity matrix of order r. The columns of P are the left singular vectors $\mathbf{p}_r$, and the columns of E are the right singular vectors $\mathbf{e}_r$ of the data matrix X.

The Σ matrix is diagonal and its diagonal elements are the (positive) singular values of X in descending order, so that

$$\Sigma = diag(\sigma_1, \sigma 2, ..., \sigma_r) \text{ with } \sigma_1 \geqslant \sigma 2 \geqslant ... \geqslant \sigma_r \geqslant 0 \tag{5.18}$$

The SVD applied to the covariance matrix S (5.9) yields to:

$$S = \frac{1}{\mathcal{T}} E \Sigma^2 E^T \tag{5.19}$$

It can be shown that the SVD of the anomaly data X and the eigenvalue analysis of its covariance matrix S deliver the same information. The columns $\mathbf{p}_r$ of P and the columns $\mathbf{e}_r$ of E are the left and right singular vectors of X, respectively. With the left singular vectors as the eigenvectors (EOFs) and the right singular vectors as the eigenvalues (PCs) of the data matrix anomaly X. The EOFs and the PCs can therefore be directly extracted from the SVD of X. The singular values σ_r of X are the square roots of the eigenvalues λ_k of S per $\mathcal{T}$, so that

$$\lambda_k = \frac{1}{\mathcal{T}} \sigma_k^2 \tag{5.20}$$

After separation of singular vectors and -values of X, Equation (5.17) can be written as

$$\mathbf{x}_t = \sum_{k=1}^{r} \mathbf{p}_{tk} \sigma_k \mathbf{e}_k \tag{5.21}$$

This equation describes the synthesis of original data at all spatial locations at time t by r principal components. If a compression of the original data without a significant loss of information is desired, a truncation of the sum in Equation (5.21) is possible, which means summing only over the first singular values instead of overall r [5]. The choice of number of PCs or modes is arbitrary, but as described before (5.18) the first PC contain the most variability. The truncation of modes M to m drops the equal sign in Equation (5.1) and the synthesis of the original data out of the EOFs and PCs becomes an approximation:

$$X(t,s) \approx \sum_{k=1}^{m<M} c_k(t)u_k(s) \tag{5.22}$$

This formulation of the SVD is one out of many, but it offers a compact representation of the original data since it drops unnecessary zero singular values due to $r = T \ll S$, which is the case for meteorological or environmental parameters.

5.3 Variations of EOF Analysis

There exist many variations of EOF with each a different goal and application. Several of those variations are nicely outlined by Hannachi (2007) [27]. In this thesis, several possible enhancements of the EOF analysis have been tested on the data to see if significant improvement over the standard EOF analysis could be detected. First the expansion of EOF to Complex EOF was considered in order to capture evolving or propagating patterns in the field, which cannot be achieved with basic EOFs.

To increase the interpretability and meaningfulness of EOFs many different approaches are discussed in literature. EOF rotation is the most commonly used method, as it is very simple [59]. EOF rotation will be introduced at the end of this chapter.

5.3.1 Complex Orthogonal Functions

Conventional EOF analysis which was presented above allows us to find stationary patters when applied to a space-time field. These patterns are stationary in the sense that with any obtained EOF pattern there is a corresponding time series, which only shows decrease or increase of the magnitude of that EOF pattern over time while the spatial structure itself remains the same [27]. We therefore do not know about the relative time, or the phase, of the impact [5]. As EOFs are based on (simultaneous) covariances, the arrangement of the elements is irrelevant. In fact, two univariate time series x_t and y_t and any permutation ($\pi_{f(t)}$) of them will yield the same covariance [27]. This leads to

$$\rho_{xy} = \mathrm{cov}(x_t, y_t) = \mathrm{cov}(x_{\pi(t)}, y_{\pi(t)}) \tag{5.23}$$

for $t = 1, 2, ..., n$. This proves that any propagating signal in the field will not be detected by EOFs [27]. The evolution of EOFs to Complex EOFs (CEOFs) can solve this problem.

An explanation can be found when looking at a signal that can be represented as a wave and can therefore be generally described as

$$x(t) = Ae^{i\omega t + \phi_0} = Ae^{i\phi} = A(\cos(\phi) + i\sin(\phi)) \tag{5.24}$$

where A is the wave amplitude, e the Euler's constant, i the imaginary unit, ω the frequency, ϕ_0 the phase shift at the origin and ϕ the actual phase. By augmenting the input data with a complex component propagating signals may be detected by the EOF analysis [5] [27] [28]. There are many options to add a complex component to the dataset proposed in literature [27] In this study Hilbert Transform is used to "complexify" the original dataset. This technique was introduced by Rasmusson et al (1981) [58] and has been used in CEOF successfully [5] [27] [28].

Hilbert Transform Hilbert Transform augments the original data with a complex component by using its Hilbert transform as the imaginary part. This leads to the inclusion of the information about the rate of change of the field as the artificial imaginary part. It can therefore be seen as the time derivative of the original process [5].

The Hilbert Transform is shortly introduced here. It follows the descriptions found in Hannachi et al. (2007) [27] and Bauer-Marschallinger (2012) [5]:

Let $\mathbf{x}_t = (x_{1s}, x_{2s}, ..., x_{ts})$ with $t = 1, 2, ..., n$ be the representation for a time series from a field $X(t, s)$. With vector Fourier coefficients $\mathbf{a}(\omega)$ and $\mathbf{b}(\omega)$ the Fourier representation of the time series is:

$$\mathbf{x}_t = \sum^{\omega} \mathbf{a}(\omega)\cos(\omega t) + \mathbf{b}(\omega)\sin(\omega t). \tag{5.25}$$

Since propagating waves need a complex representation as in Equation (5.24), Equation (5.25) can be transformed to yield the general complex Fourier decomposition:

$$\mathbf{y}_t = \sum^{\omega} \mathbf{c}(\omega) e^{-i\omega t} \tag{5.26}$$

with $\mathsf{Re}(\mathbf{y}_t) = \mathbf{x}_t$ and $\mathbf{c}(\omega) = \mathbf{a}(\omega) + i\mathbf{b}(\omega)$. This new complex field $\mathbf{y}_t = (y_{t1}, y_{t2}, ..., y_{tp})^T$ can therefore be written as:

$$\mathbf{y}_t = \mathbf{x}_t + i\mathcal{H}(\mathbf{x}_t) \tag{5.27}$$

where the imaginary part of $\mathbf{y}_t$ is the Hilbert transform of $\mathbf{x}_t$

$$\mathcal{H}(\mathbf{x}_t) = \sum^{\omega} \mathbf{b}(\omega)\cos(\omega t) - \mathbf{a}(\omega)\sin(\omega t). \tag{5.28}$$

The Hilbert transform $\mathcal{H}(\mathbf{x}_t)$ is seen to represent a simple phase shift by $\frac{\pi}{2}$ in time. In fact, it can be seen that the Hilbert transform when considered as a filter, removes zero frequency without affecting the modulus of all others. As mentioned above, the Hilbert transform can also be considered as the time derivative of the original process in case the time series contains only one frequency. Therefore, locally in the frequency domain $\mathcal{H}(\mathbf{x}_t)$ provides information about the rate of change of $\mathbf{x}_t$ with respect to time t.

The derivative character and the $\frac{\pi}{2}$ phase shift becomes evident when comparing Equation (5.25) and Equation (5.28). Both become manifest in the switch of sin and cos at the **a**-term and **b**-term and the change in sign for the **a**-term, which reflect the basic relation between these two functions [5].

For completeness, the Hilbert transform of a continuous time series x(t) is in formal terms defined by the convolution

$$\mathcal{H}(x_t) = \frac{1}{\pi}\int \frac{x(u)}{t-u}du. \tag{5.29}$$

In practice, the Hilbert transform of a continuous time series is estimated using Fourier coefficients with are commonly derived from Fast Fourier Transformation [27] [28].

Hilbert EOF Analysis To apply EOF Analysis on the "complexified" dataset using the Hilbert Transform only minor changes to the EOF analysis presented in the beginning of this section have to be applied. This is then called Hilbertain EOFs (HEOFs). First the real-valued time series of the field $X(t,s)$ are expanded as in Equation (5.27). Then the covariance matrix of the complexified dataset Y yields

$$S_{yy} = \frac{1}{\mathcal{T}}\sum_{k=1}^{\mathcal{T}} \mathbf{y}_t \mathbf{y}_t^{\star T} \tag{5.30}$$

in which $\star$ donates the complex conjugate, and $\mathcal{T}$ is the number of elements of the time series as above. The HEOFs are then equal to the eigenvectors of S_{yy}. Of course, they can also be obtained as the right complex singular value vectors of the data matrix Y through SVD. The complex PCs (CPCs) are obtained by adapting Equation (5.16). The eigenvalues, which are still real-valued, are calculated accordingly as in the regular EOF case.

5.3.2 EOF Rotations

The rotation of EOF results is done to increase interpretability of the results. These linear transformations are based on vector rotation and yield simpler patterns than in the original EOFs. Most of the analytic rotations are simple algebraic expressions which attempt to approximate simple structure through the application of specially designed mathematical algorithms which distribute the PC loadings such that the dispersion of the loadings is maximized by maximizing the number of large and small coefficients.

These so-called rotation criteria are not unique and the number of EOFs used for the rotation remains arbitrary. [27]

Hannachi et al. (2007) provide a comprehensive introduction into the rotation of EOFs:

Rotation of the EOF patterns can systematically alter the structures of EOFs. By constraining the rotation to maximise a simplicity criterion, the rotated EOF patterns can be made simple. Given a $p \times m$ matrix $E_m = (e_1, e_1, ...e_m)$ of the loadings m EOFs, the rotation is formally achieved by seeking an $m \times m$ rotation matrix R to construct the rotated EOFs B according to:

$$B = E_m R \tag{5.31}$$

where R can also be $(R_T)_{-1}$ depending on the type of rotation as detailed below. The criterion for choosing the rotation matrix R is what constitutes the rotation algorithm or the simplicity criterion, and is expressed by the maximisation problem:

$$\max f(E_m R) \tag{5.32}$$

over a specified subset or class of $m \times m$ square rotation matrices R. The functional $f()$ in (5.32) represents the rotation criterion. Note that instead of rotating the EOFs E_m as in (5.31), one could equally rotate the EOFs scaled by the square root of the corresponding eigenvalues, i.e. using $E_m \times m$, where $m = (\lambda_1, \lambda_2, ..., \lambda_m)$ is the diagonal matrix containing the leading singular values. Alternatively, one can also rotate PCs instead. Various rotation criteria exist in the literature. Richman (1986) [59], for example, lists more than ten simplicity criteria. Broadly speaking, there are two large families of rotation: orthogonal and oblique rotations. While the criterion for an orthogonal rotation seeks an orthogonal rotation matrix R, in oblique rotation one seeks a (non-orthogonal) rotation matrix R [27]. In this thesis, a criterion for each the orthogonal rotation and the oblique rotation have been tested. In this section, these criteria are briefly introduced.

Varimax

The varimax criterion is the most well-known orthogonal rotation algorithm for EOFs. In orthogonal rotation, the rotation matrix R in (5.31) is chosen to be orthogonal, and $\mathcal{R} = \mathsf{R}$. The problem is to solve (5.32) subject to the condition:

$$\mathsf{R}\mathsf{R}^\mathsf{T} = \mathsf{R}^\mathsf{T}\mathsf{R} = I_m \tag{5.33}$$

where I_m is the $m \times m$ identity matrix. For the varimax criterion let us designate by $b_{ij}, i = 1, ...p$, and $j = 1, ...m$, the elements of the rotated EOFs matrix B in (5.31), i.e. $b_{ij} = [\mathsf{B}]_{ij}$, then the varimax orthogonal rotation maximises a simplicity criterion according to:

$$max\left(f(\mathsf{B}) = \sum_{k=1}^{m}\left[p\sum_{j=1}^{p} b_{jk}^4 - \left(\sum_{j=1}^{p} b_{jk}^2\right)^2\right]\right) \tag{5.34}$$

where m is the number of EOFs chosen for rotation. The quantity inside the square brackets in (5.34) is proportional to the (spatial) variance of the square of the rotated vector $b_k = (b_{1k}, ..., b_{pk})^\mathsf{T}$. Therefore, varimax attempts to simplify the structure of the patterns by pushing the loadings coefficients towards zero, or ± 1. [27] [36]

Quartimin

In oblique rotations, a non-orthogonal rotation matrix R with unit length columns is chosen, so that the oblique rotated EOFs

$$\mathsf{B} = \mathsf{E}_m(\mathsf{R}^\mathsf{T})^{-1} \tag{5.35}$$

minimise a certain criterion $f(\mathsf{B})$. One well known example for oblique rotation is the quartimin criterion, which corresponds to:

$$f(B) = \frac{1}{4} \sum_{r \neq s} \sum_{k} b_{kr}^2 b_{ks}^2 \tag{5.36}$$

The oblique rotation matrix is calculated by solving (5.32) which is subject to the previous constraints [27]. The quartimin criterion

5.4 Correlations

To identify if two or more samples of datasets or observations are statistically connected is subject of Correlation Analysis [65]. Correlation analysis can be used to detect if two or more signals are synchronous and to what extent. There exist many different methods in this field that provide information concerning the strength and the direction of these relationships between data. The causality of these relationships can of course not be determined with these methods. Additional distinct statements about the quality of the correlation analysis are needed together with the actual results of the correlations analysis. [5]. This is why in this study we use correlations measures to investigate the relationship of variables of the hydrology in the Mediterranean region and different climate modes. In this study, Spearman Rank Correlation was used to quantify this relationship, as it does not require assumptions about the probability distribution of the samples. In the following paragraph, this correlation method is briefly introduced.

Spearman Rank Correlation Suppose our data consists of pairs of n observations on two variables A and B, $(A_1, B_1), (A_2, B_2), ..., (A_n, B_n)$. We first order (or rank) all the observations from A between themselves from smallest to largest (or from largest to smallest). Then we independently do the same for the values of B. So, each observation is assigned a rank according to its position relative to all other observations in its own group. In case that this ranking can be done unambiguously without any two values claiming the same rank the Spearman correlation coefficient is defined by:

$$\rho = 1 - \frac{6}{n^3 - n} \sum_{i=1}^{n} D_i^2 \tag{5.37}$$

where D_i, $i = 1, 2, ..., n$ are the differences in ranks of A_i and B_i and n is the number of observations in each group. It can be shown that

$$-1 \leqslant \rho \leqslant 1. \tag{5.38}$$

In case the variables A and B are perfectly correlated $\rho = 1$, while if they are the complete opposite of each other and have a perfect negative correlation $\rho = -1$. $\rho = 0$ when there is no relation between A and B values. All other values of ρ that are between the extremes give a relative indication on the relation between A and B [25].

The significance of a non-zero value of ρ can be tested by computing the test quantity

$$t = \rho\sqrt{\frac{N-2}{1-\rho^2}} \tag{5.39}$$

which is distributed approximately as Student's distribution with $N - 2$ degrees of freedom. [5]

6 Results and Discussion

This study uses several variations of EOF analysis to quantify the impact of climate modes on the Mediterranean hydrology. In this chapter, the different set-ups as explained in Section 5.1 are discussed in a chronological order according to the study. Then an example case with graphic output examples is presented. For this, first the spatial subset for the study is chosen and the impact of the spatial extent is shown. Then variation of EOF analysis like presented in Section 5.2 are applied to the datasets. Finally, correlations to well knows climate modes which were presented in Chapter 3 are calculated using the methods introduced in Section 5.4.

Although, in this study, the presented steps were conducted using the whole range of datasets which are listed in Chapter 4, below only examples from the study are presented in detail and an overview of the results using all datasets in given at the end of the chapter. For better comparability, the examples are all taken from the analysis of the GLEAMv3 dataset describing evapotranspiration which is introduced in Section 4.2.1.

6.1 Revealing the impact of methodological choices on identifying main patterns of evaporation

The examples presented here use the GLEAMv3 dataset which is introduced in 4.2.1. It is an evapotranspiration dataset and was chosen as the complete example for this study, because of its completeness and interesting results. The results of all other datasets were analysed as part of this study and a quick overview of them, will be given at the end of this chapter.

6.1.1 Spatial Subset

In this study both the Mediterranean basin and the Mediterranean region as presented in Section 2.1 in Chapter 2 were used in the application of EOF analysis. First the standard EOF analysis was applied to datasets with these two different spatial extents. The non-complex EOF analysis was applied over all months from 1980-2013.

The first four modes of the EOF analysis for the spatial extent of the Mediterranean basin can be seen in Figure 6.1. On the left, the spatial patterns of the first four modes are mapped in colours from red over white to blue. Red and orange colours represent negative amplitude and blue colours positive amplitude. The map corresponds to the temporal normalized amplitudes which are shown on the right. The modes are ordered by the amount of represented variance as explained in Section 5.2. The first and second mode show an annual pattern with only slight variation. The spatial pattern for all modes show strong signals in the tropics between 0°N and 15°N. Details in the spatial distribution around the Mediterranean Sea are only visible in the third mode with a difference between the area more in the south close to the Mediterranean Sea and the areas further north and more detached from the sea.

The results of the same analysis applied to the Mediterranean region is shown in Figure 6.2 with again the first four modes of the result. The first mode shows an annual pattern while the second mode shows a biannual temporal pattern. The spatial distribution is complex and shows details for the Mediterranean region. In the first mode, we see a difference between the areas south and north of the Mediterranean Sea. In the second mode, we see the same pattern that we see in the third mode of the analysis of the Mediterranean basin. The third and fourth mode also show spatial differences for the Mediterranean region in evapotranspiration.

These two examples are representative for the domain dependence of EOF analysis. The selection of the study area has a large impact on the result of the analysis [26]. As this study tried to quantify the impact of climate oscillations on the Mediterranean, and the Nile river with its vast catchment area only contributes very little to the overall situation in and around the Mediterranean Sea, but dominates the derived signal, this study applied the analysis on the Mediterranean region instead of the Mediterranean basin.

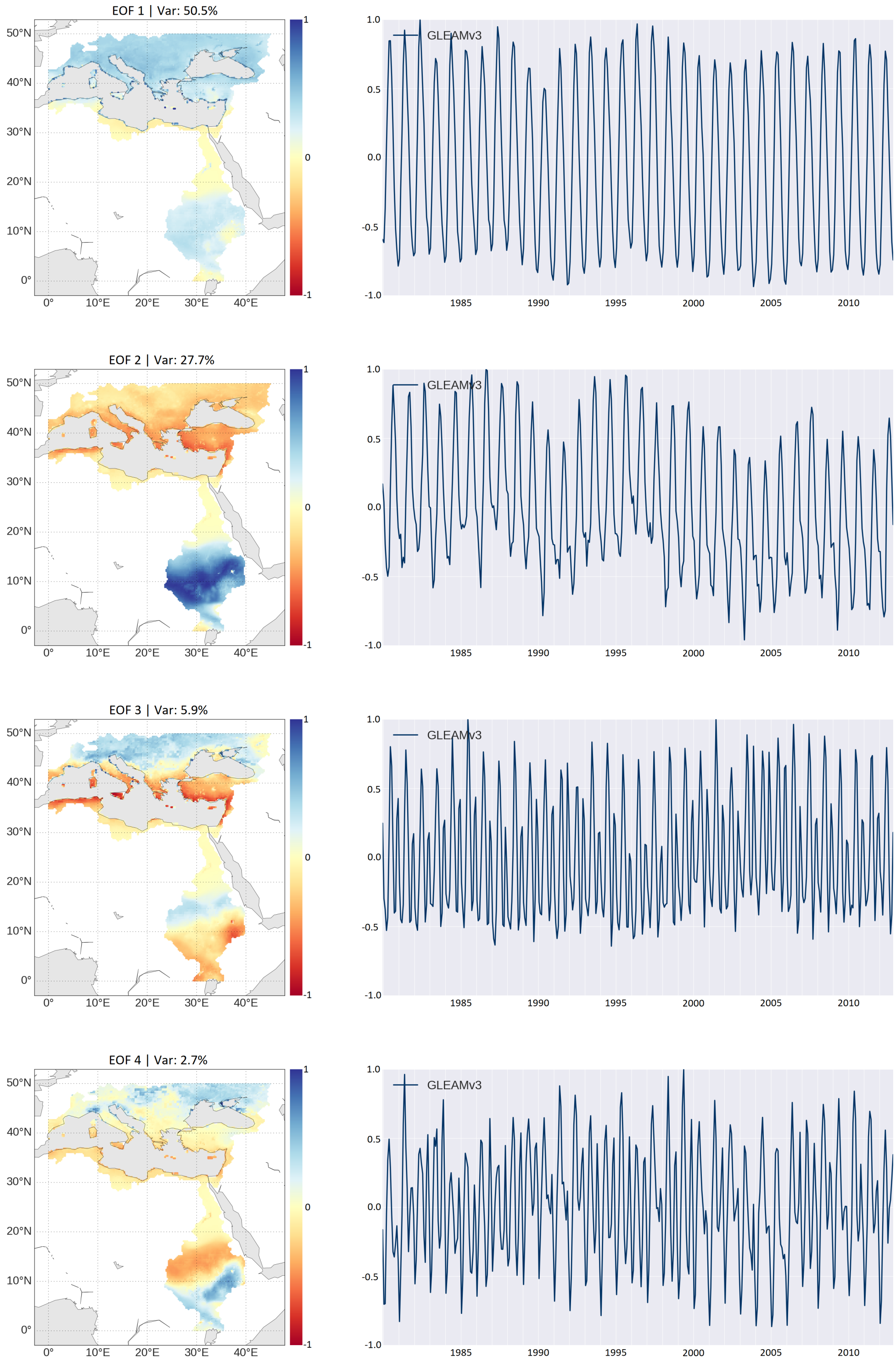

Figure 6.1: The first four modes of the results of EOF analysis applied to the GLEAMv3 dataset with the spatial extent of the Mediterranean basin. The dominance of the tropical signal from the area around Lake Victoria can be seen very clearly.

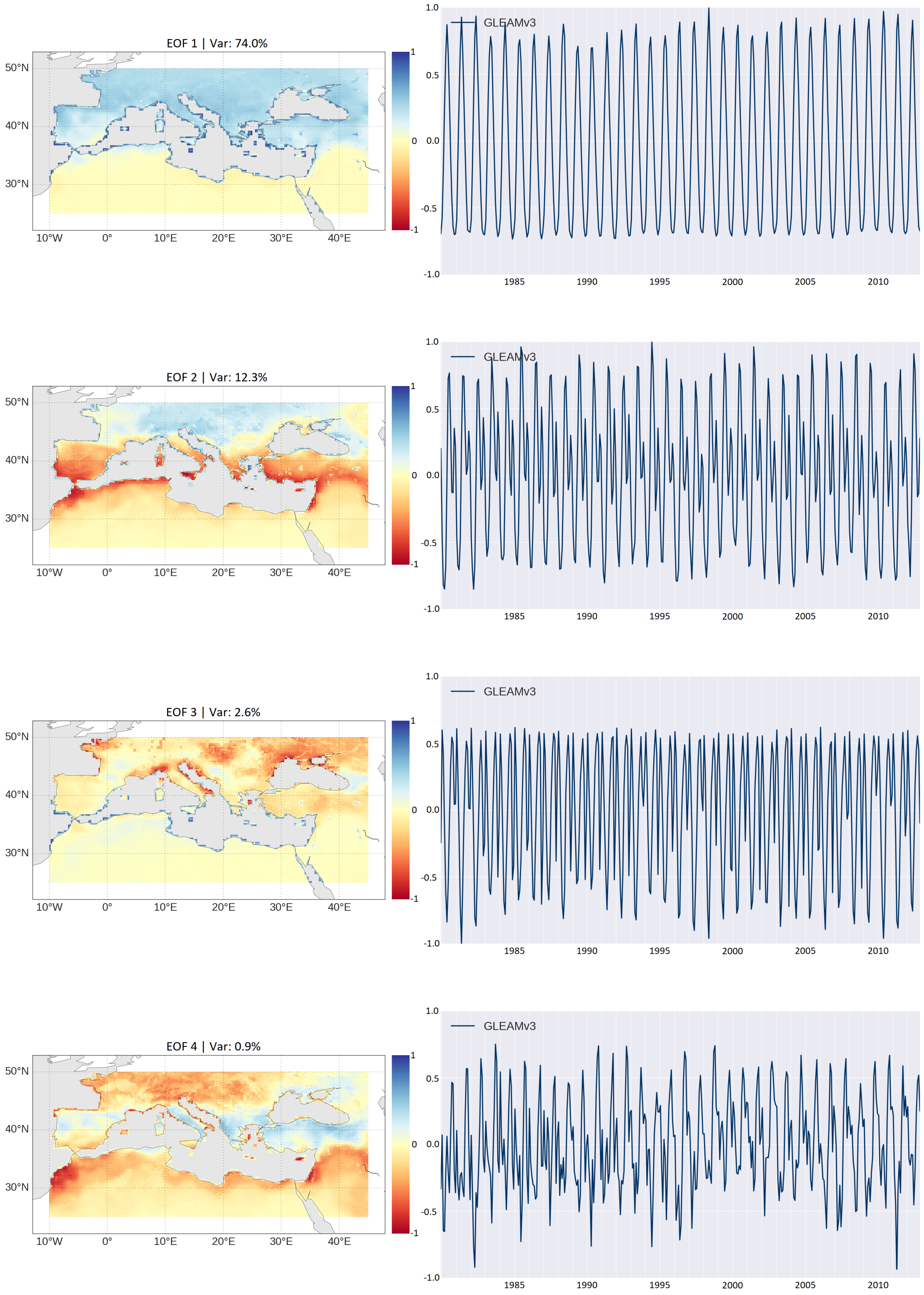

Figure 6.2: The first four modes of the results of EOF analysis applied to the GLEAMv3 dataset with the spatial extent of the Mediterranean region. A more detailed signal can be seen in the area surrounding the Mediterranean Sea.

6.1.2 Variations of EOF analysis

As presented in Section 5.2 many variations of EOF analysis exist. In this study, some of the available variations were implemented to investigate the advantages or disadvantages for each adaptation of EOF analysis. First complex EOF are applied to increase the information detail one can retrieve from the modes. Then rotations are applied to increase interpretability of the results.

Complex EOF

Analogical to the EOF analysis presented above, CEOF analysis, as described in 5.3.1, was applied to the GLEAMv3 dataset. The results of the first four modes can be seen in Figure 6.3. The results are now split up in two spatial and temporal plots for each mode. The upper plots show the spatial and temporal amplitude while the lower plots show the spatial and temporal phase. The temporal and spatial amplitude contain the same kind of information as the one found in the EOF analysis mode. The spatial pattern for the amplitude for all four modes are similar to the patterns found in the EOF results. The spatial phase and temporal phase show the propagating nature of that pattern.

The first mode explains 85.5% of variability which is significantly higher than the first mode of the EOF analysis, which only explains 74.0% of variability. The difference accounts for the fact that they each include different information: CEOF modes also contain information about the temporal relationship of the observations.

There is a clear annual signal which is demonstrated by one phase revolution per year in the phase graph of the first mode. This is connected to the spatial phase, where it shows the propagation from south to north during one annual cycle. The maximum amplitude is reached in the north around July-August and in the south in January-February. Also in the southern regions of the northern coast of around the Mediterranean has the maximum amplitude in April-May. The amplitude plots show that there is barely any evapotranspiration in the south, except for coastal areas.

The second mode explains 4.6% of variability and shows a biannual phase pattern.

There is also a biannual signal in the phase pattern of the third mode which explains 1.0% of variability.

The fourth mode with has a different spatial amplitude pattern compared to the fourth mode of the EOF analysis and explains only 0.8% of variability.

Rotations of EOF

In this study both rotations presented in Section 5.3.2 were applied to the datasets. Both rotation criteria deliver similar results for the rotated EOFs, which is in accordance with Hannachi et al. (2006) [26].

While some of the rotated EOFs did in fact increase interpretability for some datasets (see Figure 6.15 and Figure 6.16) the overall result for the GLEAMv3 dataset was not satisfying. The rotated EOFs followed extreme outliers and disregarded the general patterns present in the signal. Especially the first mode has lost the general annual temporal pattern and the north south spatial pattern. The rotations have failed for this dataset in particular, because of the outlier pixel along the coast of the Mediterranean Sea.

Varimax The result of rotated EOFs using the varimax criterion show both positive and negative outlier for the first mode. The second to forth mode is dominated by the positive outliers in the temporal pattern. Interestingly the overall spatial pattern remains the similar to the spatial pattern of the not rotated EOFs.

Quartimin The result of rotated EOFs using the quartimin criterion show mostly positive outliers for all four modes. Which is a small difference in the result compared to the results using the varimax criterion. Again, the overall spatial pattern remains the similar to the spatial pattern of the not rotated EOFs for the second to fourth mode. The spatial pattern of the first mode is almost identical for the one found in the result using the varimax criterion.

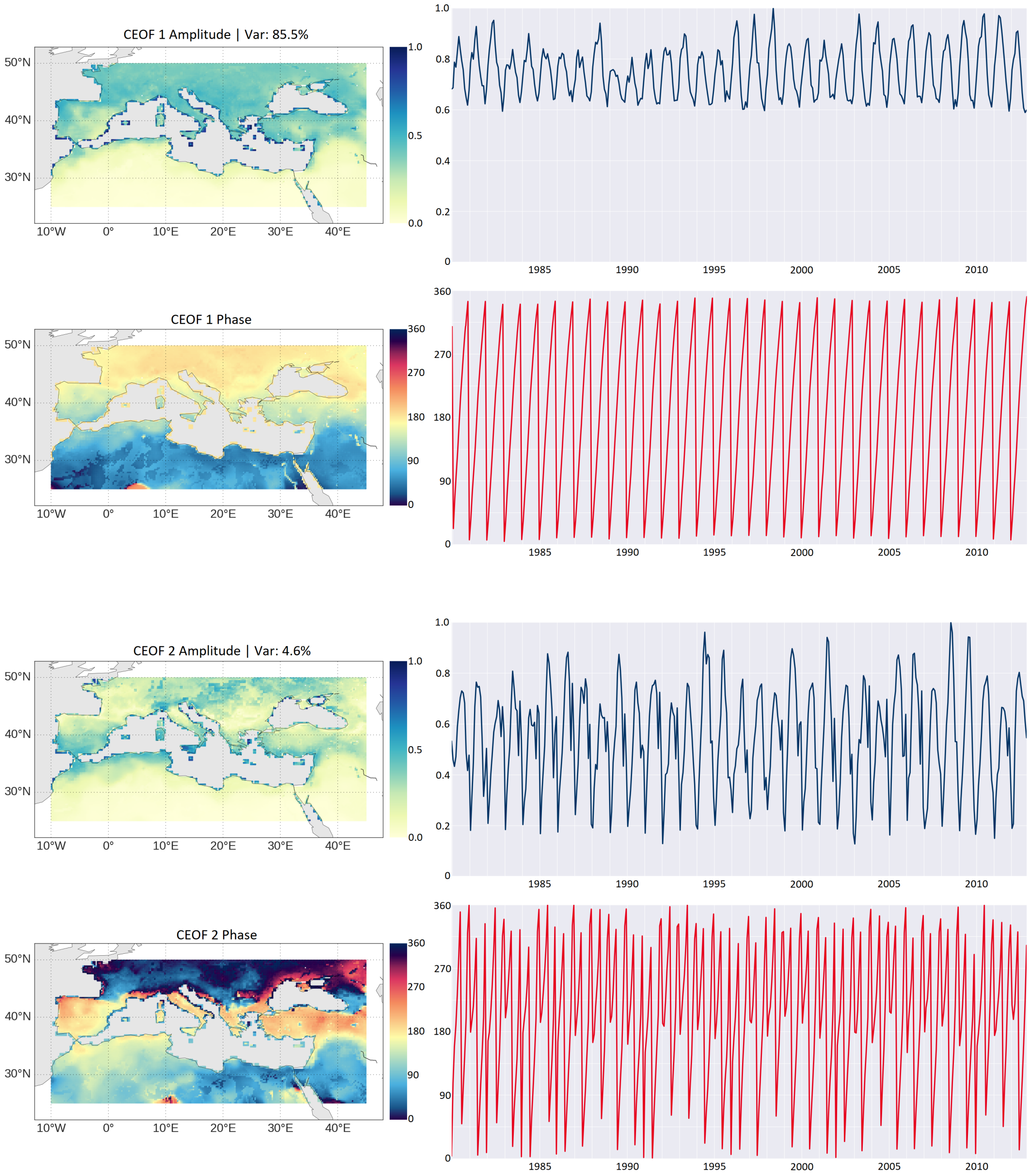

Figure 6.3: Part 1 - mode 1 and 2 of the first four modes of the results of Complex EOF analysis applied to the GLEAMv3 dataset.

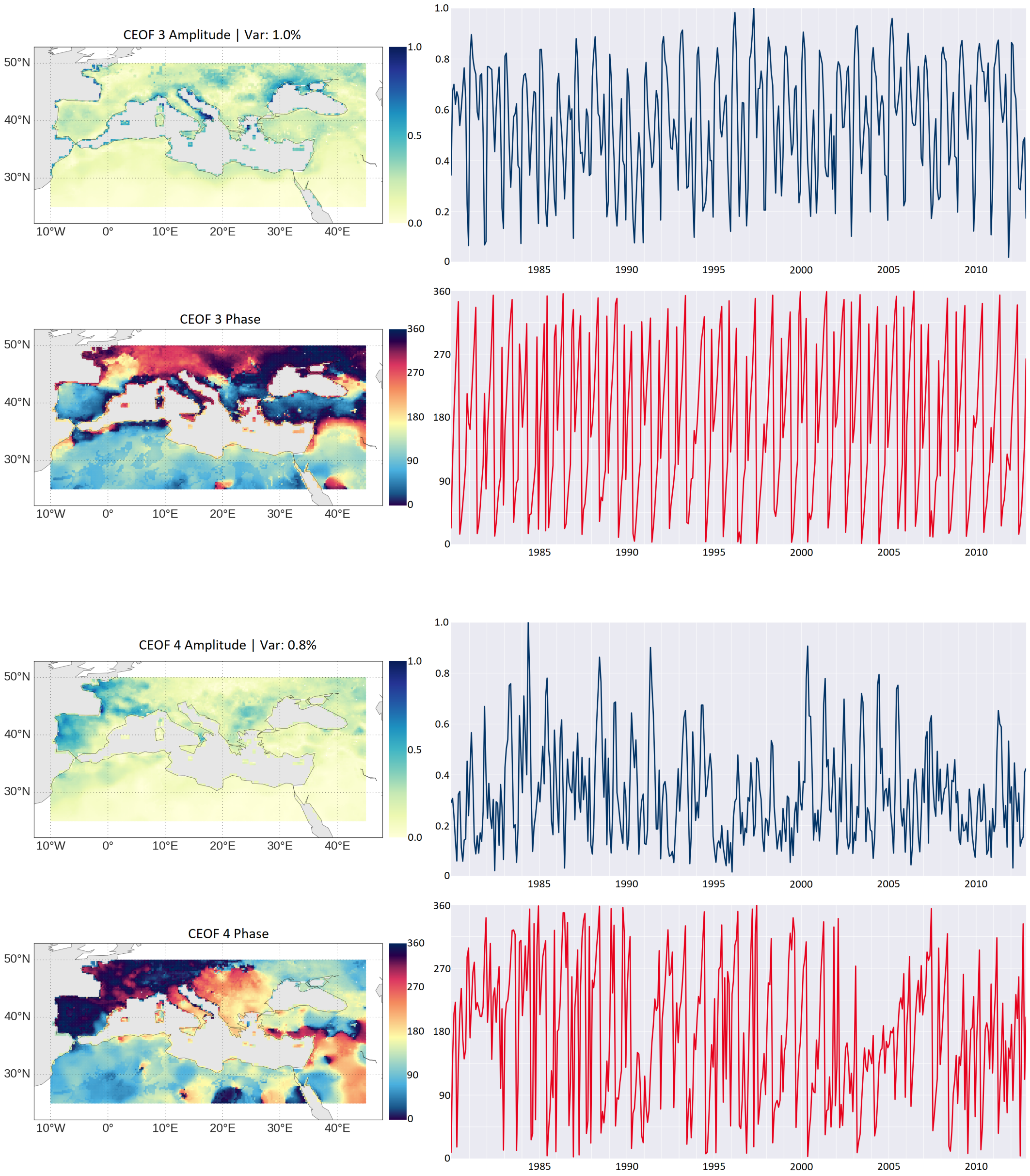

Figure 6.3: Part 2 - mode 3 and 4 of the first four modes of the results of Complex EOF analysis applied to the GLEAMv3 dataset.

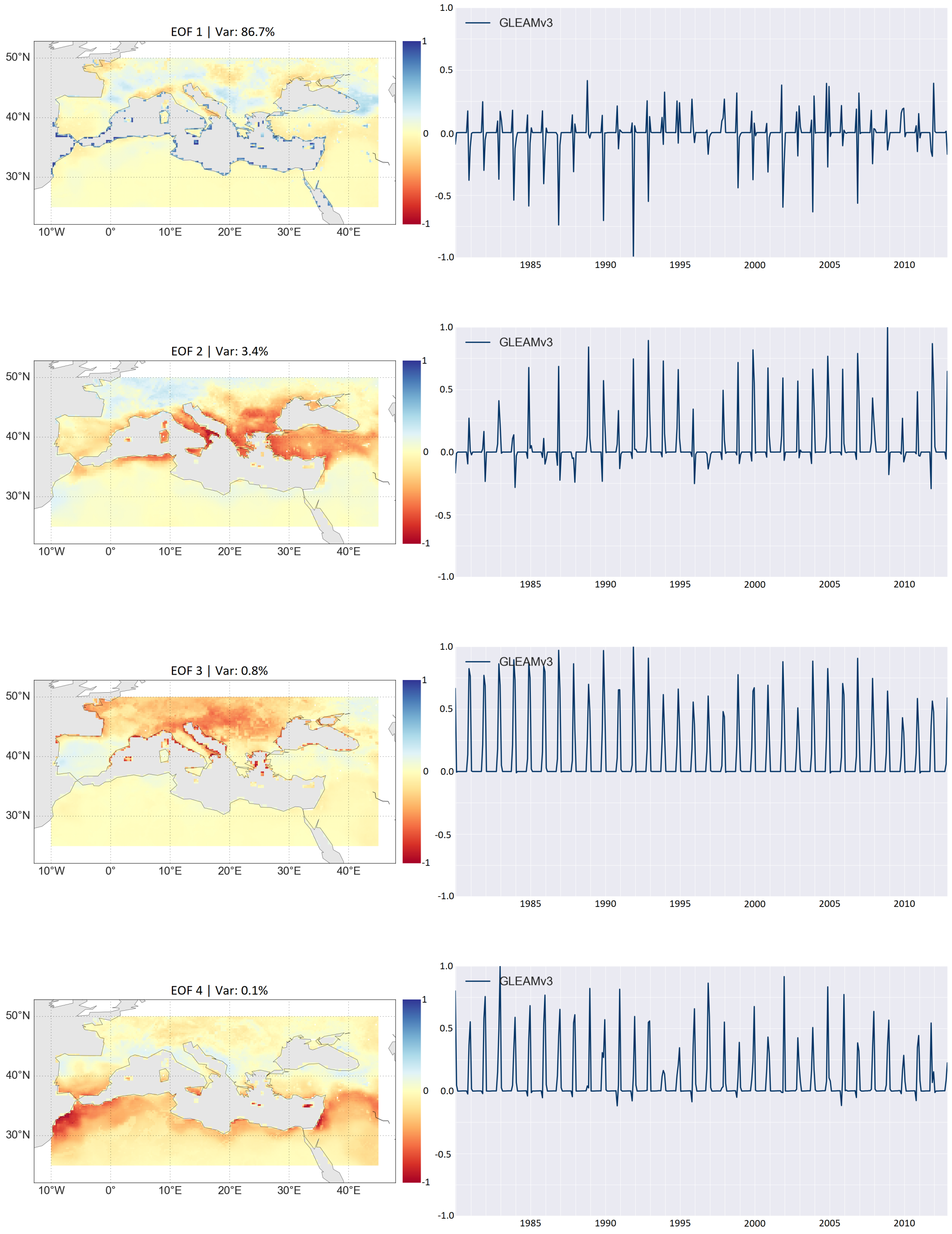

Figure 6.4: The first four modes of the results of EOF analysis and rotation using the varimax criterion applied to the GLEAMv3 dataset with the spatial extent of the Mediterranean region. A more detailed signal can be seen in the area surrounding the Mediterranean Sea.

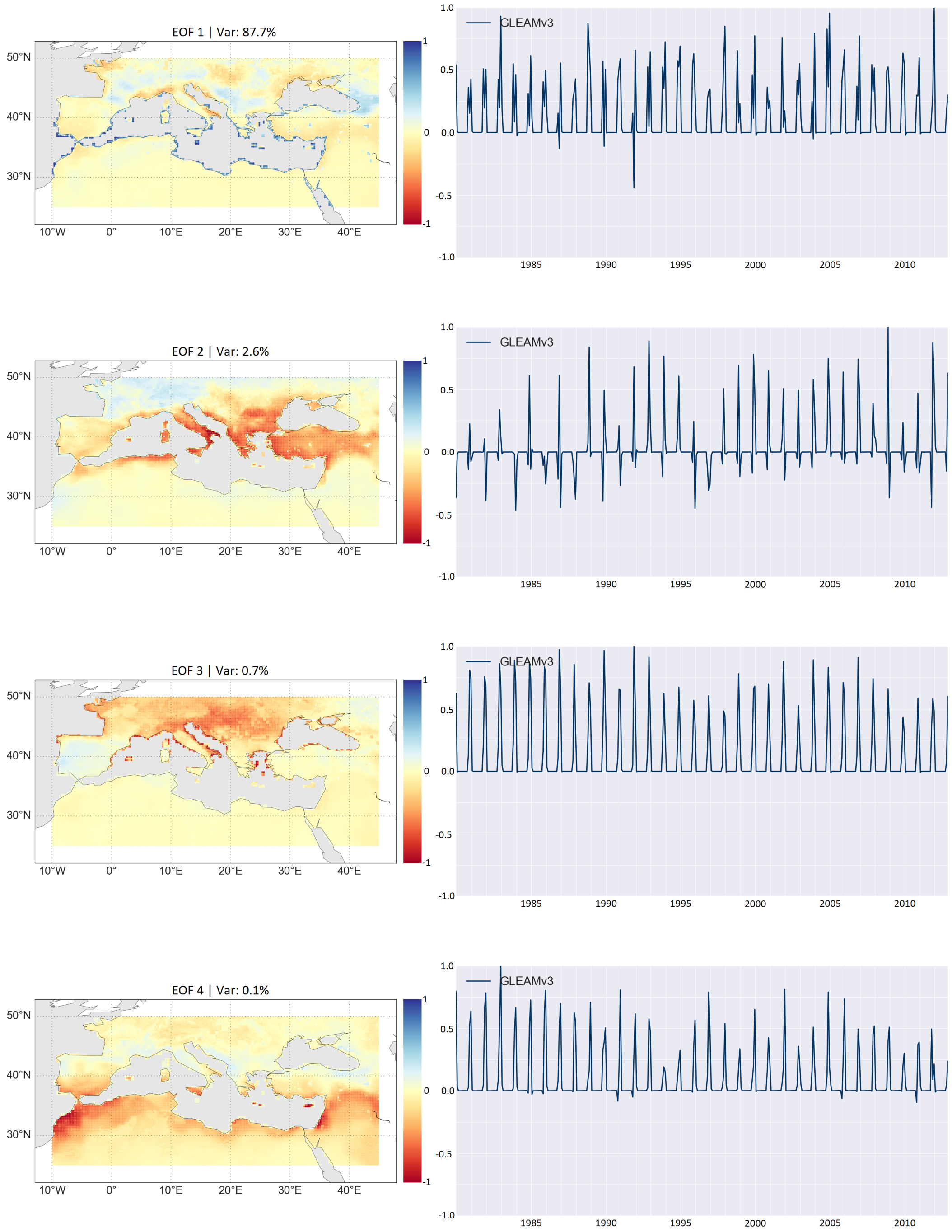

Figure 6.5: The first four modes of the results of EOF analysis and rotation using the quartimin criterion applied to the GLEAMv3 dataset with the spatial extent of the Mediterranean region. A more detailed signal can be seen in the area surrounding the Mediterranean Sea.

6.1.3 Correlations with Climate Modes

To find a correlation between climate modes and the retrieved climate signals Spearman Rank correlation as introduced in Section 5.4 was used. The correlations were calculated for the monthly values, for subsets of the monthly values by season, and by using results of the EOF analysis with the averaged seasonal values as an input. In the following some representative examples of results are presented and then an overview of the overall results given. The graphics used to show the results show a 2D grid with the first four modes of the EOF analysis in the x-axis and a list of climate modes on the y-axis. The Spearman Rank coefficient for each combination is filled in the grid which for easier review also uses a shaded background colour according to the value of the correlation coefficient. Positive values have a blue background, while negative values have a red background.

Monthly Correlations were calculated for all months of the resulting EOF and the monthly values of the selection of climate indices. Overall the correlation values with this set-up were low, ranging between -0.2 and $+0.2$.

The example shown in Figure 6.6 is the correlation matrix of not rotated EOF temporal values and the selected climate indices. The maximum value for correlation was with the East Pacific - North Pacific (EP-NP) index and the first three modes of the EOF analysis, with correlation values of a maximum of 0.19.

Seasonal Correlations were calculated by only using seasonally averaged values for DJF, MAM, JJA, and SON as an input to the EOF analysis. The results of the seasonally re-sampled dataset (see Figure 6.7) are different from the monthly results, by having a smoothing effect on the temporal pattern and a very different spatial pattern for modes three and four.

The temporal values of the results were then correlated with the seasonally averaged values of the climate indices (Figure 6.8). The values for the correlation were even lower than for the monthly data and no climate index stood out with a higher value.

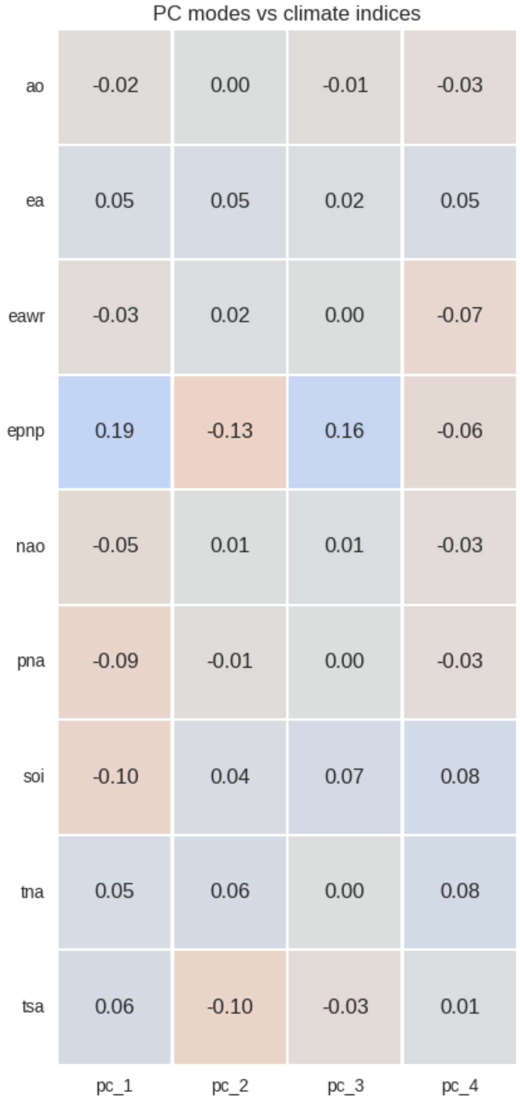

PC modes vs climate indices

	pc_1	pc_2	pc_3	pc_4
ao	-0.02	0.00	-0.01	-0.03
ea	0.05	0.05	0.02	0.05
eawr	-0.03	0.02	0.00	-0.07
epnp	0.19	-0.13	0.16	-0.06
nao	-0.05	0.01	0.01	-0.03
pna	-0.09	-0.01	0.00	-0.03
soi	-0.10	0.04	0.07	0.08
tna	0.05	0.06	0.00	0.08
tsa	0.06	-0.10	-0.03	0.01

Figure 6.6: Monthly correlations of EOFs and climate modes

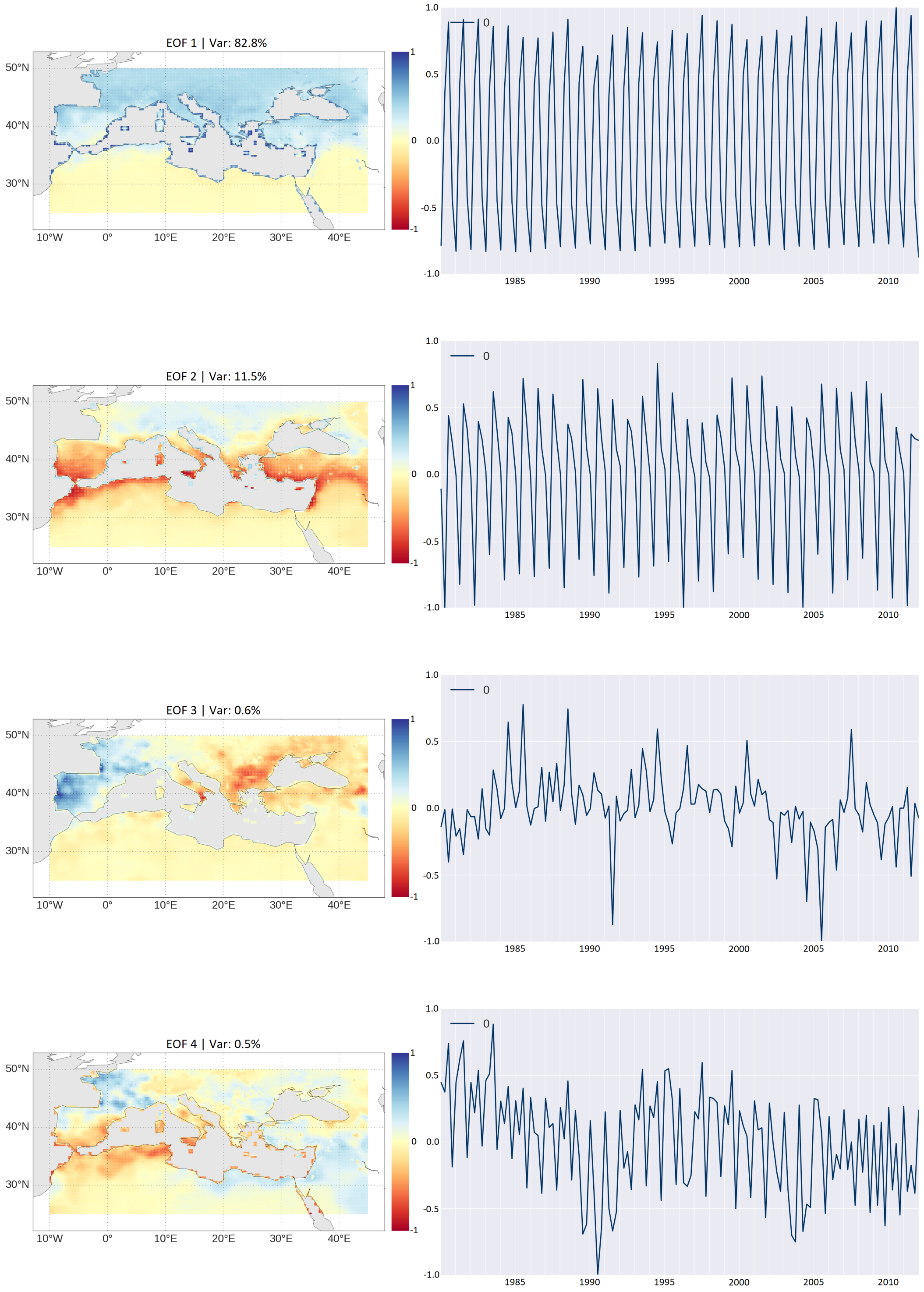

Figure 6.7: The first four modes of the results of EOF analysis applied to the GLEAMv3 dataset with seasonal values.

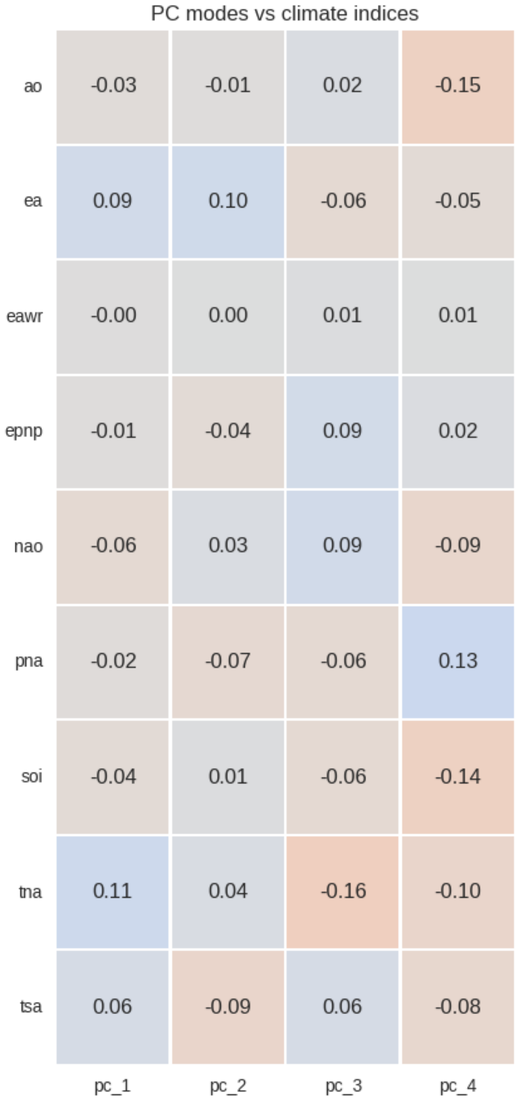

Figure 6.8: Seasonal correlations of EOFs and climate modes using all seasonal values for correlation.

The results were then correlated by season, meaning: all DJF values of the result temporal pattern were correlated with all the DJF values of the climate indices. This lead to high correlation values for specific climate indices for varying seasons. The example (Figure 6.9) shows the results for all four seasons. As other studies have shown the winter values are especially highly correlated with the climate modes. The EA has a 0.68 correlation value with the first mode and the AO and NAO correlate highly with the second mode. This is in agreement with the findings of previous studies. Also, the high correlation value (0.42) of the first mode and the SOI index for the MAM season is in line with other studies. Surprising are the high values for the correlation with the Pacific/North American (PNA) index in the JJA and SON season, as no earlier studies could be found stating this correlation.

For each value in the correlation matrix an individual plot showing the correlated values plotted on top of each other, was created. The plots give a good understanding about the relationship of the two correlated values. In Figure 6.10 the individual plots for the pairs with the highest correlation values are shown. For the DJF season the correlation with AO, EA, and NAO are shown. For MAM season, the correlation with SOI is pictured, for JJA season with TNA, and SON season with PNA.

Complex Correlations were calculated using the results of CEOF. The correlation with climate indices was calculated for the real and imaginary part separately and the absolute values of the complex numbers. Therefore, for each CEOF result three correlation matrices were created.

The matrices in Figure 6.11 show the correlation of the CEOF analysis result for the monthly sampled dataset with the climate indices. All three show low correlation values in between -0.2 and $+0.2$. The three matrices do not show much similarity on which values correlate and which not.

(a) DJF

	pc_1	pc_2	pc_3	pc_4
ao	0.01	0.72	-0.12	-0.35
ea	0.68	-0.20	0.41	-0.10
eawr	-0.02	-0.02	-0.08	0.01
epnp	-0.07	-0.31	-0.10	0.29
nao	-0.23	0.64	-0.28	-0.03
pna	-0.11	-0.12	-0.27	0.32
soi	0.03	0.13	0.24	-0.36
tna	0.41	-0.21	0.10	-0.07
tsa	0.26	-0.05	0.22	0.00

(b) MAM

	pc_1	pc_2	pc_3	pc_4
ao	0.26	0.01	0.26	-0.37
ea	0.33	0.27	-0.21	0.04
eawr	0.23	-0.01	-0.03	-0.15
epnp	-0.21	0.05	-0.02	0.07
nao	-0.05	0.08	0.30	-0.29
pna	-0.27	0.33	-0.10	0.41
soi	0.42	-0.05	0.06	-0.45
tna	0.14	-0.30	-0.12	0.16
tsa	0.27	-0.09	0.05	-0.33

Figure 6.9: Correlation by season for the GLEAMv3 dataset for DJF MAM.

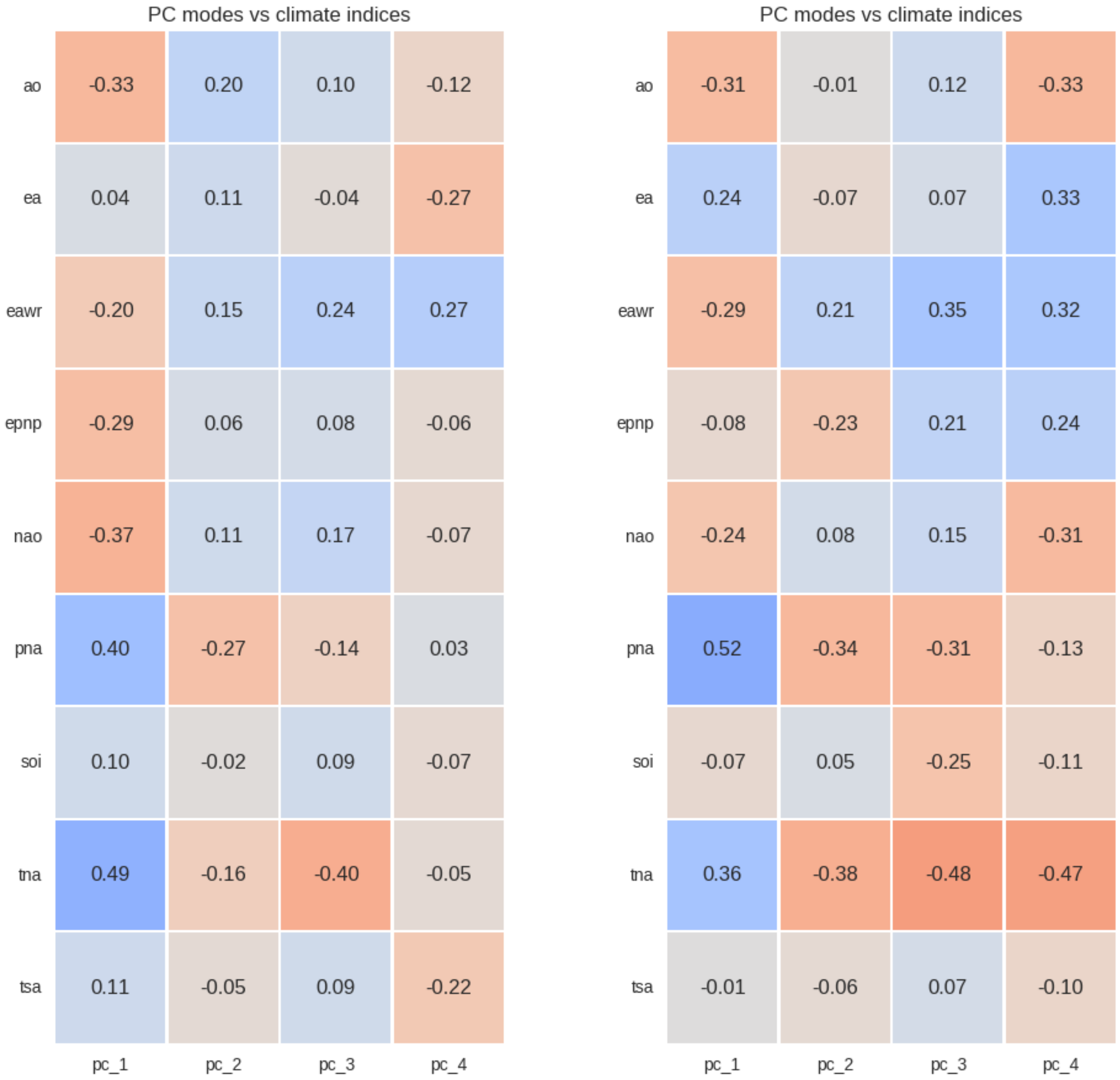

(c) JJA. (d) SON.

Figure 6.9: Correlation by season for the GLEAMv3 dataset for JJA SON.

(a) Mode 2 for DJF with AO.

(b) Mode 1 for DJF with EA.

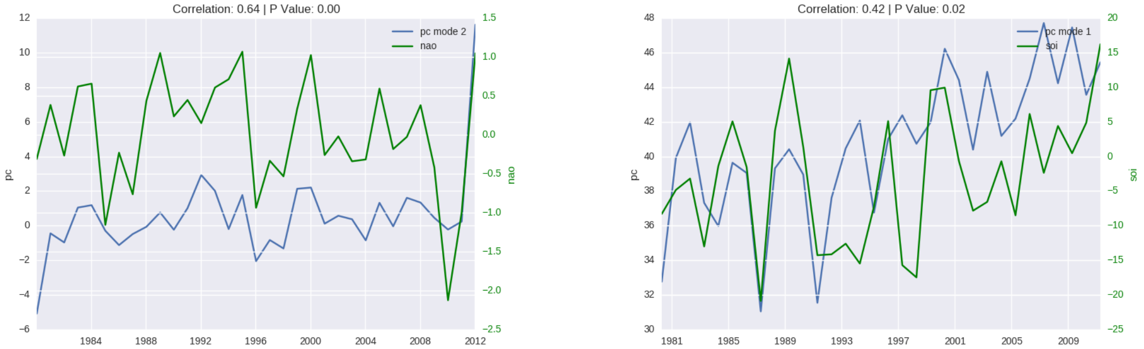

(c) Mode 2 for DJF with NAO.

(d) Mode 1 for MAM with SOI.

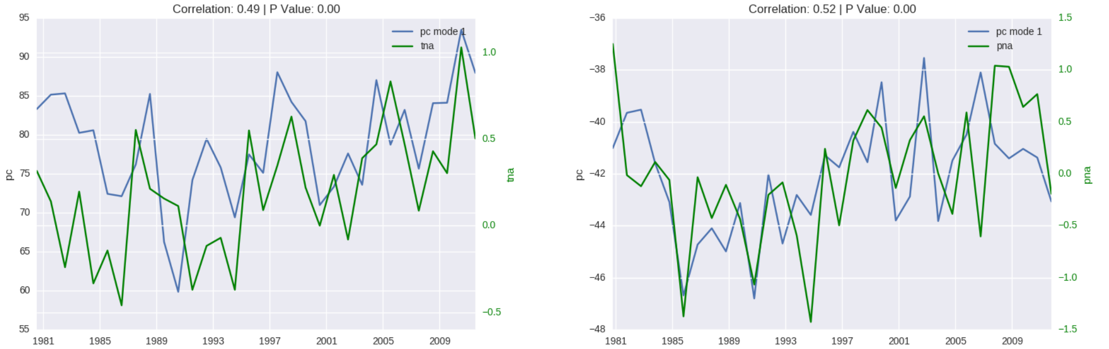

(e) Mode 1 for JJA with TNA.

(f) Mode 1 for SON with PNA.

Figure 6.10: Selected individual plots for high correlation values when correlating the seasonal values with climate modes per season for the EOF analysis results of the GLEAMv3 dataset with the Mediterranean region as a study area.

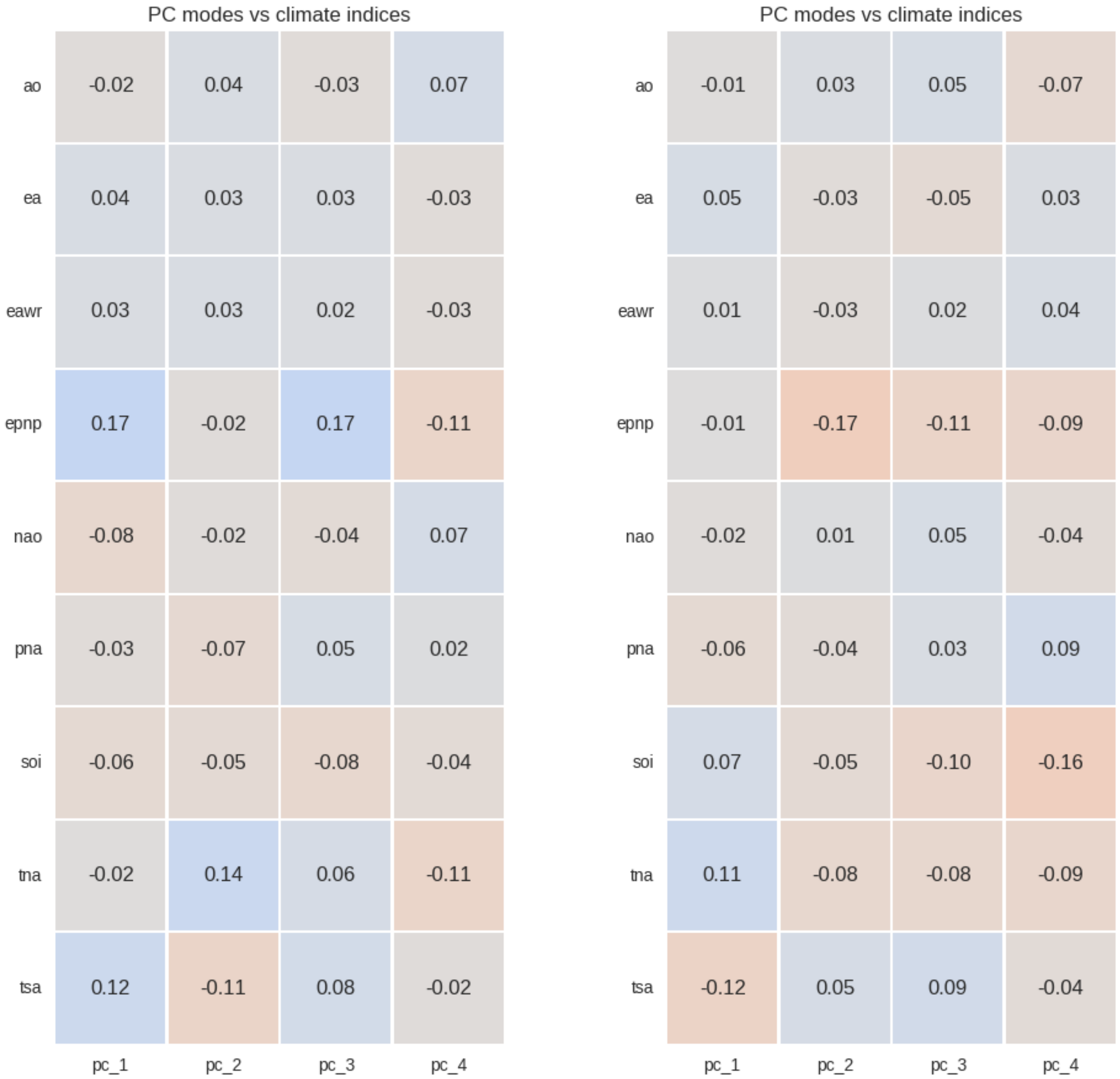

(a) amplitude

(b) imaginary part

Figure 6.11: Correlation for the CEOF analysis of the GLEAMv3 dataset separated for amplitude, the imaginary part, and the real part of the complex values.

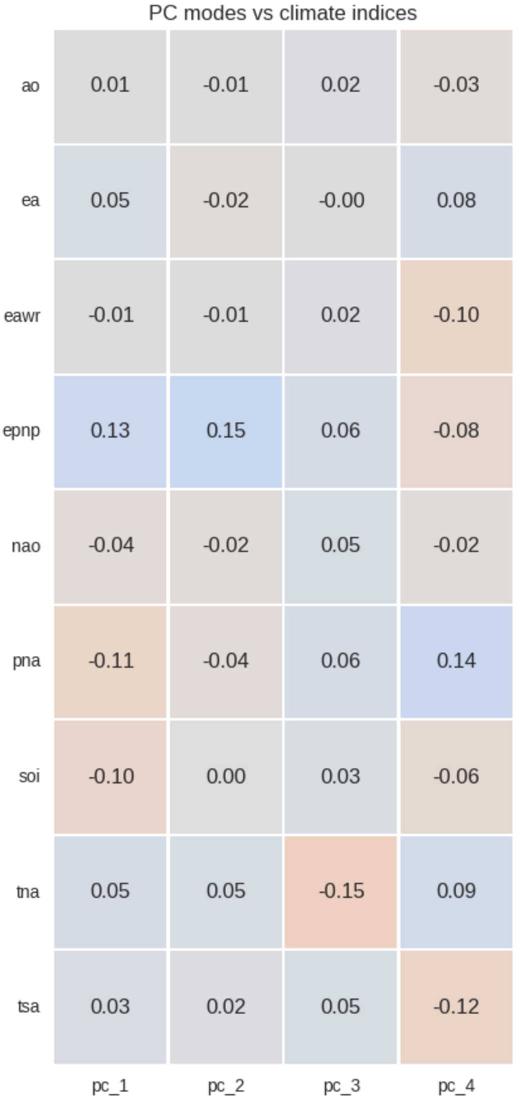

	pc_1	pc_2	pc_3	pc_4
ao	0.01	-0.01	0.02	-0.03
ea	0.05	-0.02	-0.00	0.08
eawr	-0.01	-0.01	0.02	-0.10
epnp	0.13	0.15	0.06	-0.08
nao	-0.04	-0.02	0.05	-0.02
pna	-0.11	-0.04	0.06	0.14
soi	-0.10	0.00	0.03	-0.06
tna	0.05	0.05	-0.15	0.09
tsa	0.03	0.02	0.05	-0.12

(c) real part.

Figure 6.11: Correlation for the CEOF analysis of the GLEAMv3 dataset separated for amplitude, the imaginary part, and the real part of the complex values.

6.2 General Results

In this section, a short overview of the results of all variables is given with the results of one dataset is shown in more detail as an example.

6.2.1 Precipitation

As an example, for this variable the results of the EOF analysis without rotation for the seasonally sampled GPCP dataset can be seen in Figure 6.12. The first mode shows the annual signal with only small variations over the year describing 50.6% of total variability. The second mode shows the characteristic dipole patter of the western and eastern Mediterranean describing 10.9% of total variability. This dipole pattern can also be found in the third mode of the CMORPH dataset and the second mode of the TRMM-TMPA dataset.

For correlation analysis results of the EOF modes (see Figure 6.13) show high correlations in the winter months for AO and NAO for the first mode. The spring months show low correlations for the first mode, but relatively high correlations for the second mode with SOI and AO. In the summer months, the first mode correlates with EA and SOI. In the autumn months, it is notable that the first mode correlates strongly with EP-NP as well as AO.

6.2.2 Evapotranspiration

A detailed description of this dataset was given as the practical example in the previous section (see Section 6.1). For the other datasets (MODIS16, PML-ET, NTSG and PT-JPL) the EOF analysis results show a slightly different pattern especially for the second mode. There they show a strong biannual pattern, while the GLEAM v3 dataset shows an annual temporal signal. The dipole pattern found in the third mode of the GLEAM v3 dataset cannot be found in any of the other datasets. In Figure 6.14 the results of EOF analysis applied to the MODIS16 dataset is given as an example. There, the

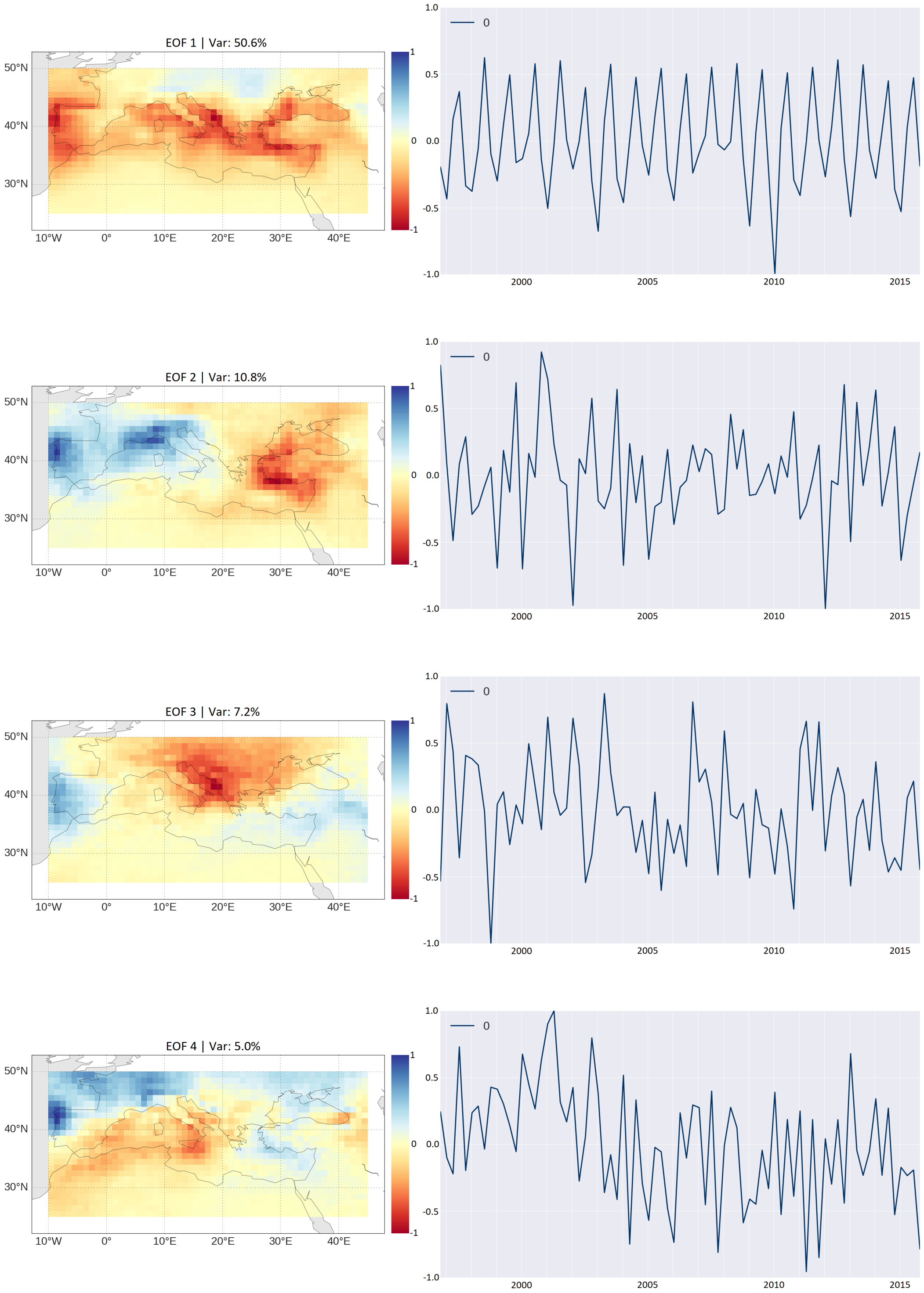

Figure 6.12: The first four modes of the results of EOF analysis applied to the GPCP dataset with seasonal values.

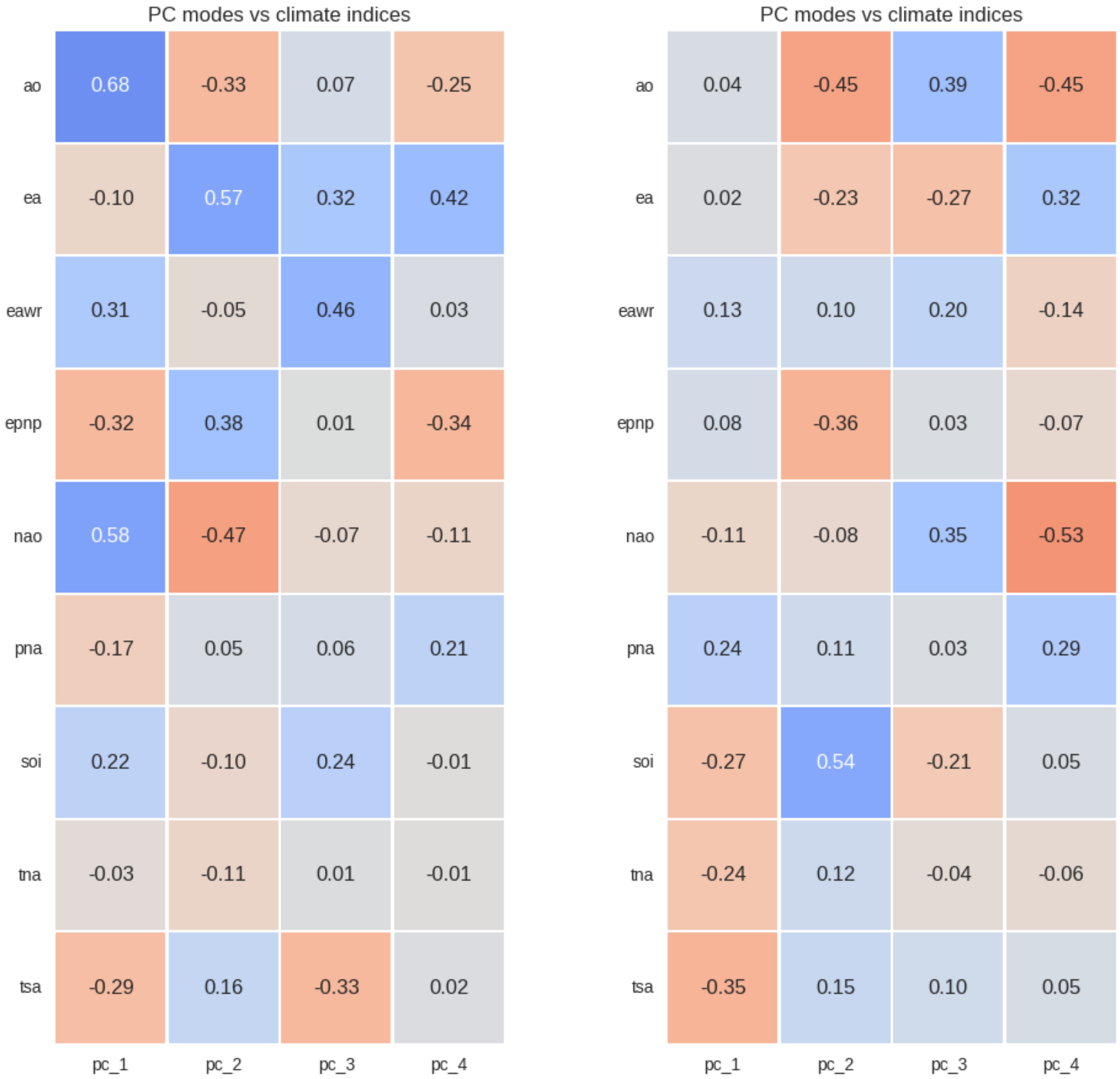

PC modes vs climate indices

	pc_1	pc_2	pc_3	pc_4
ao	0.68	-0.33	0.07	-0.25
ea	-0.10	0.57	0.32	0.42
eawr	0.31	-0.05	0.46	0.03
epnp	-0.32	0.38	0.01	-0.34
nao	0.58	-0.47	-0.07	-0.11
pna	-0.17	0.05	0.06	0.21
soi	0.22	-0.10	0.24	-0.01
tna	-0.03	-0.11	0.01	-0.01
tsa	-0.29	0.16	-0.33	0.02

(a) DJF

PC modes vs climate indices

	pc_1	pc_2	pc_3	pc_4
ao	0.04	-0.45	0.39	-0.45
ea	0.02	-0.23	-0.27	0.32
eawr	0.13	0.10	0.20	-0.14
epnp	0.08	-0.36	0.03	-0.07
nao	-0.11	-0.08	0.35	-0.53
pna	0.24	0.11	0.03	0.29
soi	-0.27	0.54	-0.21	0.05
tna	-0.24	0.12	-0.04	-0.06
tsa	-0.35	0.15	0.10	0.05

(b) MAM

Figure 6.13: Correlation by season for the GPCP dataset for DJF MAM.

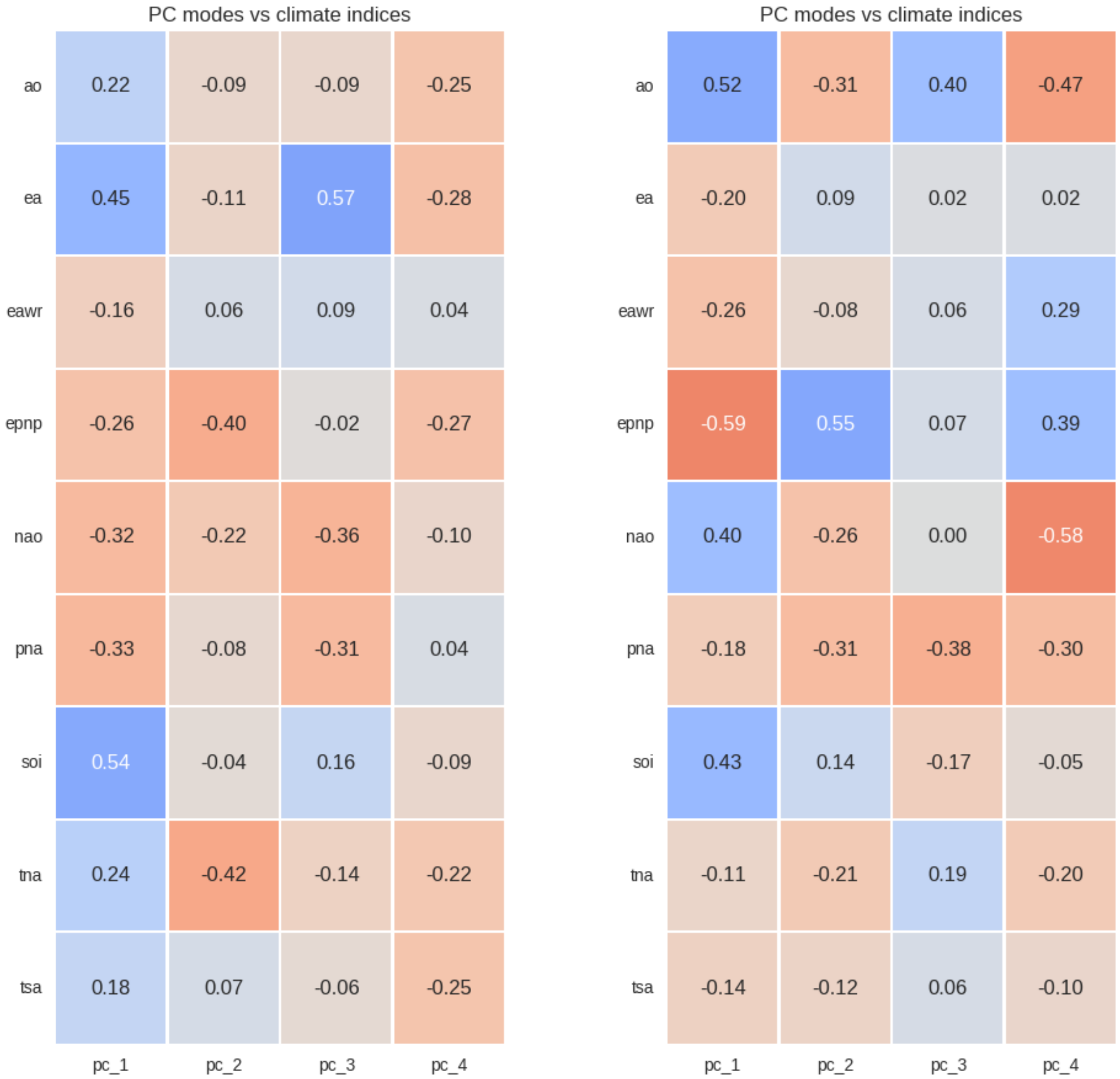

PC modes vs climate indices

	pc_1	pc_2	pc_3	pc_4
ao	0.22	-0.09	-0.09	-0.25
ea	0.45	-0.11	0.57	-0.28
eawr	-0.16	0.06	0.09	0.04
epnp	-0.26	-0.40	-0.02	-0.27
nao	-0.32	-0.22	-0.36	-0.10
pna	-0.33	-0.08	-0.31	0.04
soi	0.54	-0.04	0.16	-0.09
tna	0.24	-0.42	-0.14	-0.22
tsa	0.18	0.07	-0.06	-0.25

(c) JJA.

PC modes vs climate indices

	pc_1	pc_2	pc_3	pc_4
ao	0.52	-0.31	0.40	-0.47
ea	-0.20	0.09	0.02	0.02
eawr	-0.26	-0.08	0.06	0.29
epnp	-0.59	0.55	0.07	0.39
nao	0.40	-0.26	0.00	-0.58
pna	-0.18	-0.31	-0.38	-0.30
soi	0.43	0.14	-0.17	-0.05
tna	-0.11	-0.21	0.19	-0.20
tsa	-0.14	-0.12	0.06	-0.10

(d) SON.

Figure 6.13: Correlation by season for the GPCP dataset for JJA SON.

monthly values were used for the analysis. They clearly show the biannual temporal pattern in the second mode as described above.

An example for a representative use of rotations of EOFs can also be found in the analysis of the MODIS16 dataset. Figure 6.15 shows the result of rotated EOFs using the varimax criterion. Compared to the not rotated results the temporal pattern has a larger variance and the spatial pattern appears more refined. The variability of the first three modes is increased compared to the not rotated results. A very similar result can be seen in Figure 6.16. There the result of rotated EOFs using the quartimin criterion are shown.

6.2.3 Soil Moisture

The results of the EOF analysis without rotation for the seasonally sampled CCI dataset can be seen in Figure 6.17. It is quite striking that for all four modes the annual signal is dominating the temporal result with only very small variations over the years.

In accordance with these results, the correlation analysis results of the EOF modes are very similar across the modes. There is a strong correlation in the winter months with PNA. The only other correlation value over 0.5 can be found in the summer month for the correlation of the second mode and the TNA.

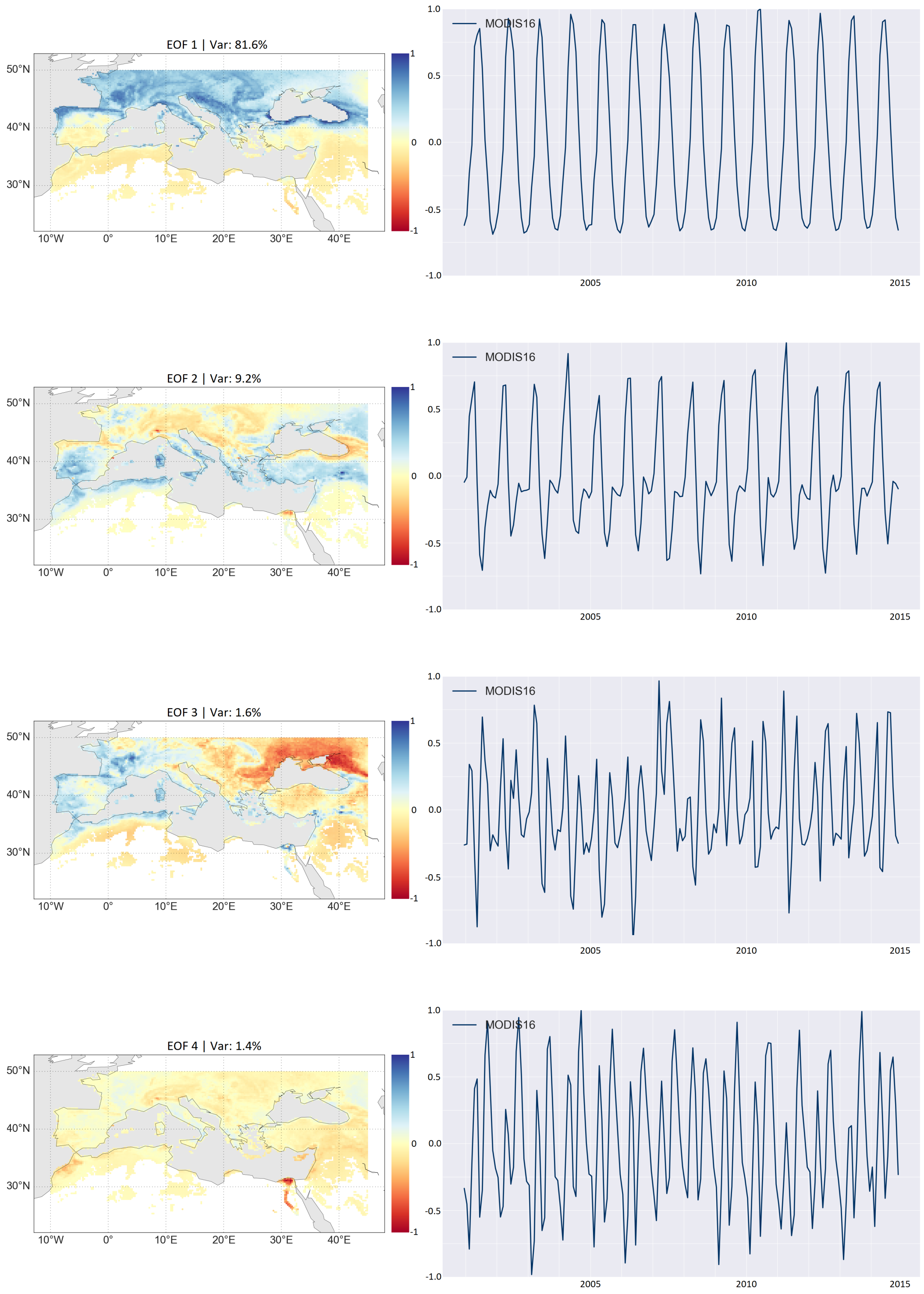

Figure 6.14: The first four modes of the results of EOF analysis applied to the MODIS16 dataset with seasonal values.

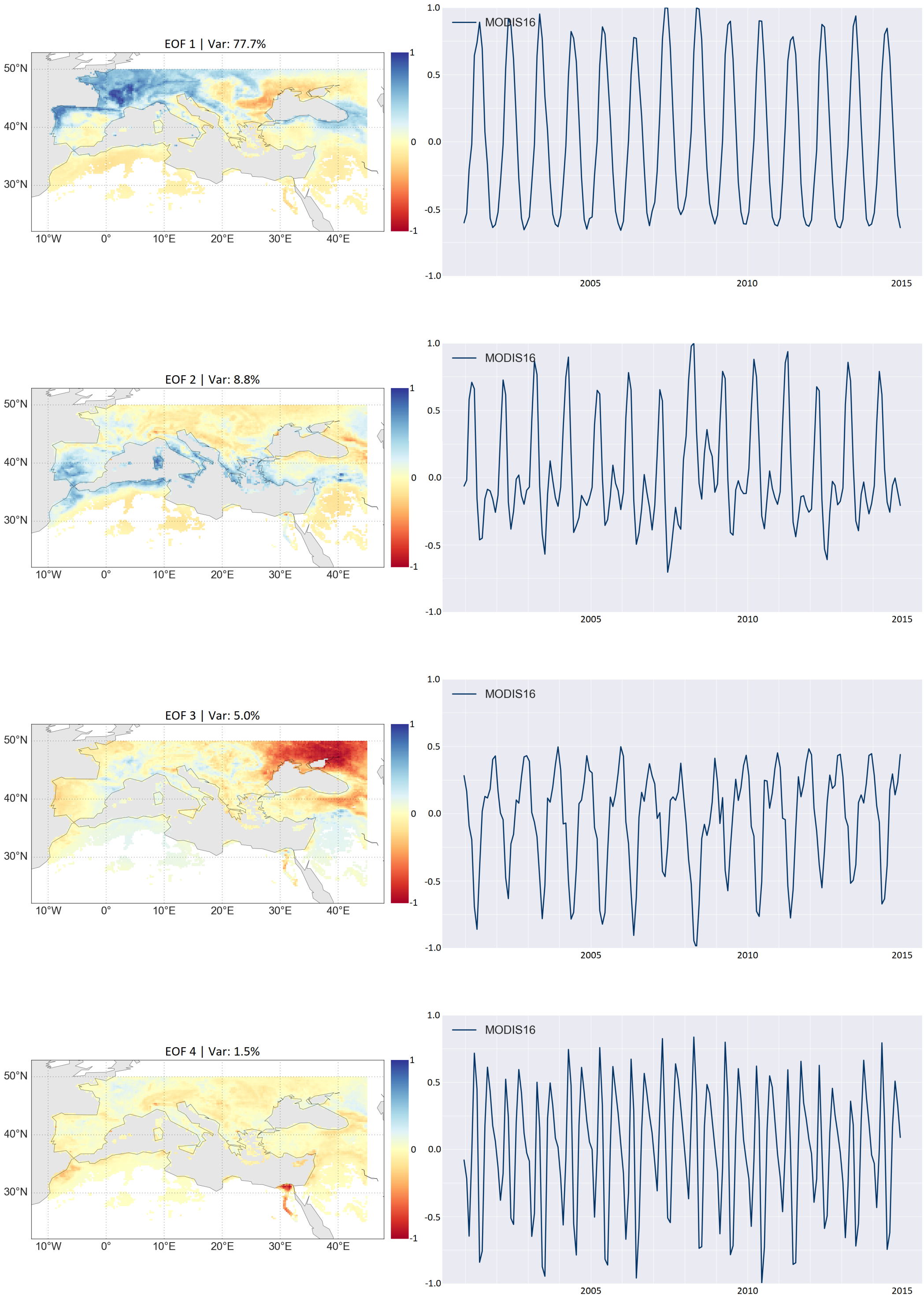

Figure 6.15: The first four modes of the results of EOF analysis and rotation using the varimax criterion applied to the MODIS16 dataset

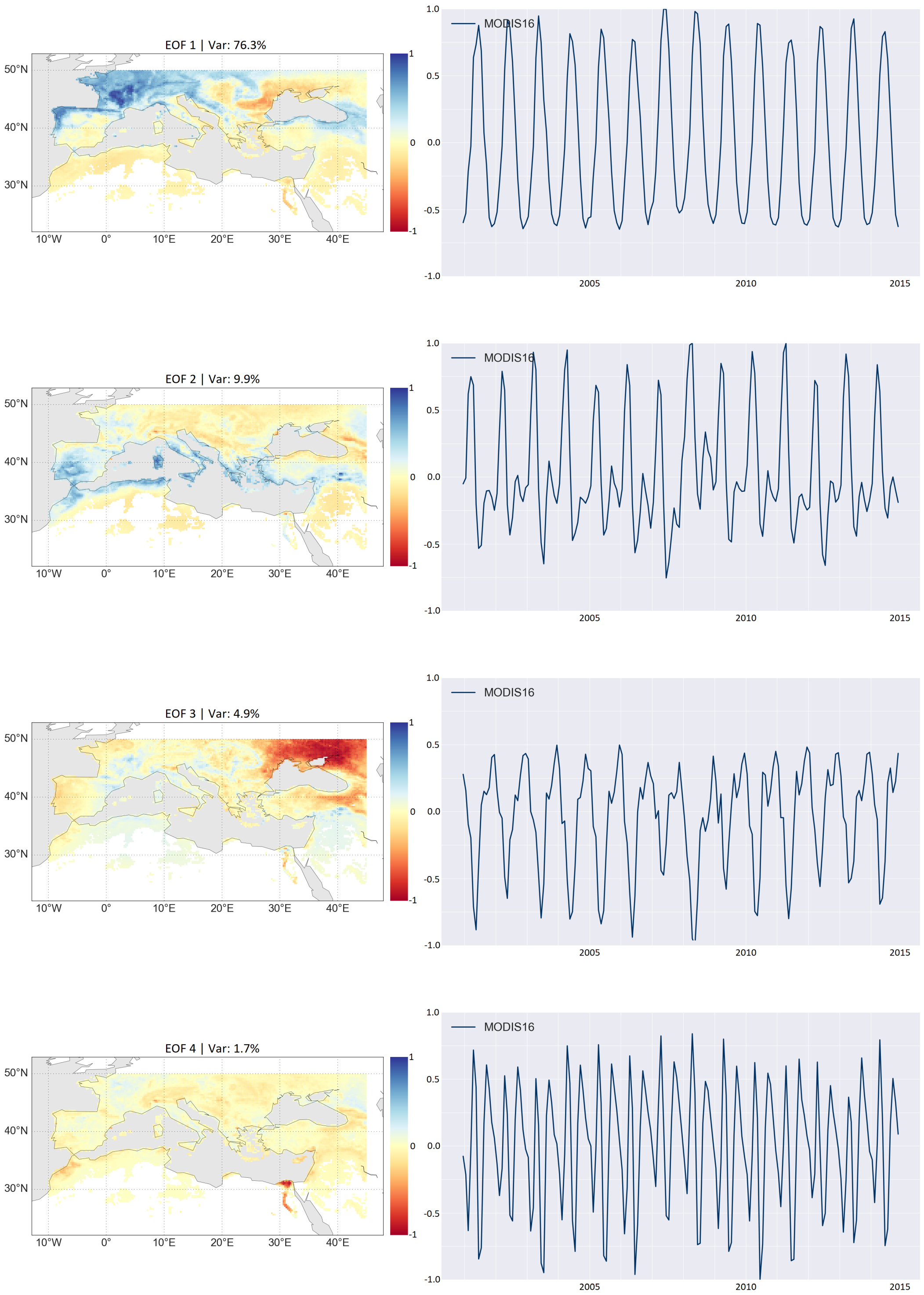

Figure 6.16: The first four modes of the results of EOF analysis and rotation using the quartimin criterion applied to the MODIS16 dataset

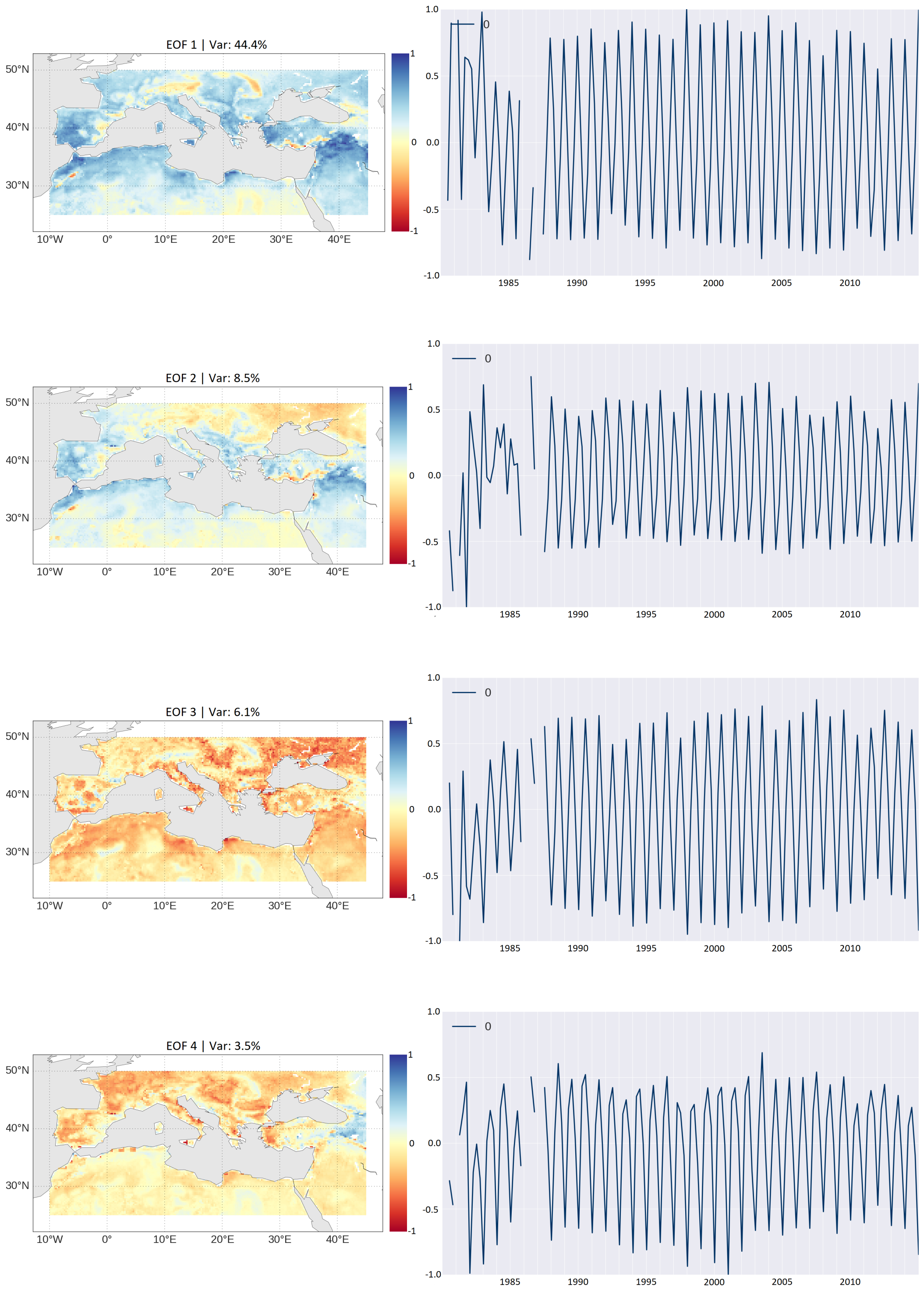

Figure 6.17: The first four modes of the results of EOF analysis applied to the CCI Soil Moisture dataset with seasonal values.

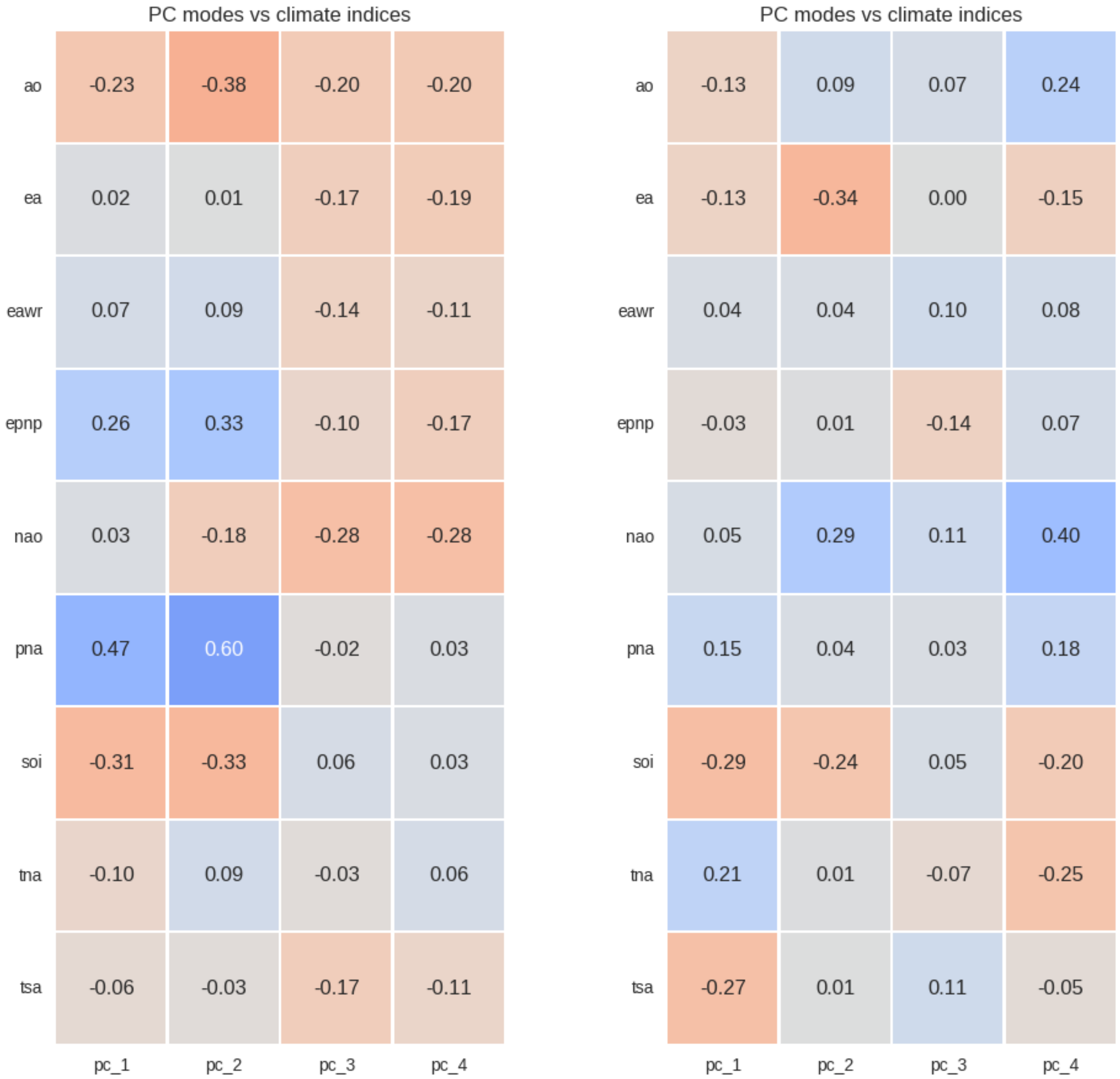

PC modes vs climate indices

	pc_1	pc_2	pc_3	pc_4
ao	-0.23	-0.38	-0.20	-0.20
ea	0.02	0.01	-0.17	-0.19
eawr	0.07	0.09	-0.14	-0.11
epnp	0.26	0.33	-0.10	-0.17
nao	0.03	-0.18	-0.28	-0.28
pna	0.47	0.60	-0.02	0.03
soi	-0.31	-0.33	0.06	0.03
tna	-0.10	0.09	-0.03	0.06
tsa	-0.06	-0.03	-0.17	-0.11

(a) DJF

PC modes vs climate indices

	pc_1	pc_2	pc_3	pc_4
ao	-0.13	0.09	0.07	0.24
ea	-0.13	-0.34	0.00	-0.15
eawr	0.04	0.04	0.10	0.08
epnp	-0.03	0.01	-0.14	0.07
nao	0.05	0.29	0.11	0.40
pna	0.15	0.04	0.03	0.18
soi	-0.29	-0.24	0.05	-0.20
tna	0.21	0.01	-0.07	-0.25
tsa	-0.27	0.01	0.11	-0.05

(b) MAM

Figure 6.18: Correlation by season for the CCI Soil Moisture dataset for DJF MAM.

	pc_1	pc_2	pc_3	pc_4
ao	-0.06	0.16	0.11	0.12
ea	-0.27	-0.10	0.40	0.07
eawr	0.04	0.36	-0.21	-0.09
epnp	0.13	0.25	-0.35	0.05
nao	0.03	0.16	-0.07	0.21
pna	0.17	-0.02	-0.01	0.03
soi	-0.15	0.11	0.11	0.11
tna	-0.04	-0.53	0.18	-0.04
tsa	-0.43	-0.19	0.43	0.37

(c) JJA.

	pc_1	pc_2	pc_3	pc_4
ao	-0.32	-0.01	0.28	0.32
ea	0.07	0.21	0.01	-0.16
eawr	-0.05	0.14	0.07	0.00
epnp	0.32	0.22	-0.29	-0.31
nao	-0.41	-0.14	0.36	0.31
pna	0.02	0.09	0.03	-0.05
soi	-0.37	-0.08	0.34	0.30
tna	-0.02	0.14	0.03	-0.20
tsa	-0.11	0.15	0.09	0.19

(d) SON.

Figure 6.18: Correlation by season for the CCI Soil Moisture dataset for JJA SON.

7 Conclusion

This study offered an insight in the spatio-temporal characteristics of the hydrology of the Mediterranean region and its connection with various climate modes. To accomplish this the study needed a lot of work in handling the big amounts of data with over ten datasets and monthly values for the entire region for roughly the last 30 years. Using EOF analysis, and variations of it made it possible to cleverly compress the data and extract the independent factors of their variability. These factors were then correlated with climate indices using Spearman Rank correlation, which was chosen for its robustness.

The Mediterranean region proved to be a highly complex study area with many details in the spatial distribution of hydrological values. By using only the region instead of the Mediterranean basin, the strong climate signals from the tropics could be avoided. Experimenting with the exact extent of the study area also showed the spatial dependency of the EOF analysis and its limitations in that perspective.

EOF analysis was chosen, because it is a well-tested tool for the extraction of climate signals from large data cubes. It indeed proved to be a useful tool in this study. It helped breaking down very large datasets into manageable modes, which then allowed further analysis. Other variations of EOF analysis did not prove to be of greater value. CEOF is a useful tool to understand the propagating nature of the modes better, but the resulting modes were not suitable for correlation analysis. The rotations of EOF proved to be highly sensitive to outliers and therefore might only deliver nonsensical results. This effect varied with the different datasets and for some, meaningful results were created. The overall result proved not to add much value to the analysis.

The relationships found between hydrological climate datasets of the Mediterranean region and climate indices all align with findings of earlier studies. The strong correlation in the winter season with NAO, AO, and EA was evident in most datasets. Also, a correlation of SOI and hydrological values in the spring months aligns with earlier findings. Correlating the values by season resulted in much higher correlation values, while using the values for the whole year showed very low correlation values. This indicates that the impact of climate oscillation on the hydrology of the Mediterranean varies throughout the year and is especially strong during the winter months.

Due to the limited scope of this master thesis, several open questions remain for further research. One suggestion is to run a meta-analysis over all of the collected results. In this study, not just the input datasets were plentiful, but the output was also too large to fully understand the connections. By statistically analysing the results, one might be able to get more general findings on the connection of climate modes and the hydrology of the Mediterranean. Also, a different form of analysis could be examined as an alternative to EOF analysis, as some limitations were met when using this method, especially the effect of the selected extent of the study area.

However, the thesis closes with the insight that climate modes do have a significant impact on the hydrology of the Mediterranean region. By using a large amount of datasets, the findings of existing studies could be enriched. The details in spatial and temporal patterns could be shown for a large number of variables and datasets. The complex nature of the topography of the region reflects in the hydrology. In addition the thesis gave insights into the effectiveness of specific variations of the EOF analysis applied to the used datasets. The findings of this thesis, hopefully contribute to the overall understanding of the Mediterranean hydrology and help to refine predictions for the future hydrology of this region.

Acronyms

AO Arctic Oscillation. iii, v, xiii, 24, 25, 65, 69, 75, 87

CCI Climate Change Initiative. 31, 36, 79

CEOF Complex Empirical Orthogonal Functions. 37, 38, 39, 59, 69, 87

CMORPH CPC MORPHing technique. 31, 33, 75

EA Eastern Atlantic. iii, v, 22, 23, 24, 27, 28, 65, 69, 75, 87

ENSO El Niño/Southern Oscillation. 19, 22, 25, 26, 27, 28

EOF Empirical Orthogonal Functions. iii, v, xiii, xiv, 21, 25, 31, 37, 38, 39, 40, 41, 42, 43, 44, 46, 47, 50, 51, 52, 55, 56, 59, 60, 65, 69, 75, 79, 87, 88

EP-NP East Pacific - North Pacific. 65, 75

ESA European Space Agency. 31, 36

GEWEX Global Energy and Water Cycle Exchanges. 33

GLEAM v3 Global Land Evaporation Amsterdam Model Version 3. 31, 34, 75

GPCP Global Precipitation Climatology Project. 31, 33, 75

MJO Madden-Julian Oscillation. 19

MODIS MODerate-resolution Imaging Spectroradiometer. 34

MODIS16 MODIS 16 - Evapotranspiration. 31, 34, 75, 79

NAO North Atlantic Oscillation. iii, v, xiii, 19, 20, 21, 22, 23, 24, 26, 27, 28, 65, 69, 75, 87

NASA National Space Agency. 34

NTSG Numerical Terradynamic Simulation Group. 31, 35, 75

PC Principal Components. 40, 46, 51

PDO Pacific Decadal Oscillation. 19

PML-ET Penman-Monteith-Leuning Evapotranspiration. 31, 35, 75

PNA Pacific/North American. 65, 69, 79

PT-JPL Priestley–Taylor Jet Propulsion Laboratory. 31, 35, 75

SLP Sea Level Pressure. 21

SOI Southern Oscillation Index. 26, 27, 65, 69, 75, 87

SST Sea Surface Temperature. 21, 22, 25, 26

SVD Singular Value Decomposition. 45, 46, 47, 50

TNA Tropical Northern Atlantic. iii, v, 21, 22, 28, 69, 79

TRMM Tropical Rainfall Measuring Mission. 33

TRMM-TMPA TRMM Multi-satellite Precipitation Analysis. 31, 33, 75

TSA Tropical Southern Atlantic. 21

WCRP World Climate Research Program. 33

Bibliography

[1] R. Adler, M Sapiano, George J. Huffman, David Bolvin, G. Gu, Jun Wang, Nelkin, Ping-Ping Xie, L. Chiu, Ralph Ferraro, Udo Schneider, and A. Becker. The New Version 2 . 3 of the Global Precipitation Climatology Project (GPCP) Monthly Analysis Product. *Journal of hydrometeorology*, 2008(April), 2016.

[2] Pinhas Alpert, Marina Baldi, Ronny Ilani, Shimon Krichak, Colin Price, Xavier Rodó, Hadas Saaroni, Baruch Ziv, Pavel Kishcha, Joseph Barkan, Annarita Mariotti, and Eleni Xoplaki. Chapter 2 Relations between climate variability in the Mediterranean region and the tropics: ENSO, South Asian and African monsoons, hurricanes and Saharan dust. *Developments in Earth and Environmental Sciences*, 4(C):149–177, 2006.

[3] Pinhas Alpert, Debbie Hemming, Fengjun Jin, Gillian Kay, Akio Kitoh, and Annarita Mariotti. The Hydrological Cycle of the Mediterranean. In Antonio Navarra and Laurence Tubiana, editors, *Regional Assessment of Climate Change in the Mediterranean: Volume 1: Air, Sea and Precipitation and Water*, pages 201–239. Springer Netherlands, 2013.

[4] Rita Valéria Andreoli and Mary Toshie Kayano. Multi-scale variability of the sea surface temperature in the Tropical Atlantic. *Journal of Geophysical Research*, 109(C5):C05009, 2004.

[5] Bernhard Bauer-Marschallinger. *Spatiotemporal Analyses of Remotely Sensed Soil Moisture with Respect to Regional Climate Modes and Solar Activity in Australia.* Masterthesis, Vienna University of Technology, 2012.

[6] Bernhard Bauer-Marschallinger, Wouter A. Dorigo, Wolfgang Wagner, and Albert I J M Van Dijk. How oceanic oscillation drives soil moisture variations over mainland Australia: An analysis of 32 years of satellite observations*. *Journal of Climate*, 26(24):10159–10173, 2013.

[7] J. P. Bethoux and B. Gentili. Functioning of the Mediterranean sea: Past and present changes related to freshwater input and climate changes. *Journal of Marine Systems*, 20(1-4):33–47, 1999.

[8] Hans-Jürgen Bolle. *Mediterranean Climate - Variability and Trends.* Springer Berlin Heidelberg, 2003.

[9] S Brönnimann. Impact of El Niño-Southern Oscillation on European climate. *Rev. Geophys.*, 45(3), 2007.

[10] Wilfried Brutsaert. *Hydrology: an introduction.* Cambridge University Press, 2005.

[11] Mirian Capa-Morocho, Belén Rodríguez-Fonseca, and Margarita Ruiz-Ramos. Sea surface temperature impacts on winter cropping systems in the Iberian Peninsula. *Agricultural and Forest Meteorology*, 226-227:213–228, 2016.

[12] Benjamin I. Cook, Kevin J. Anchukaitis, Ramzi Touchan, David M. Meko, and Edward R. Cook. Spatiotemporal drought variability in the Mediterranean over the last 900 years. *Journal of Geophysical Research: Atmospheres*, 121(5):2060–2074, 2016.

[13] O. De Viron, J. O. Dickey, and M. Ghil. Global modes of climate variability. *Geophysical Research Letters*, 40(9):1832–1837, 2013.

[14] Stanley Lawrence Dingman. *Physical Hydrolog.* Waveland press, third edit edition, 2015.

[15] Wouter Dorigo, Wolfgang Wagner, Clement Albergel, Franziska Albrecht, Gianpaolo Balsamo, Luca Brocca, Daniel Chung, Martin Ertl, Matthias Forkel, and Alexander Gruber. ESA CCI Soil Moisture for improved Earth system understanding: State-of-the art and future directions. *Remote Sensing of Environment*, 2017.

[16] P. Drobinski, V. Ducrocq, P. Alpert, E. Anagnostou, K. Beranger, M. Borga, I. Braud, A. Chanzy, S. Davolio, G. Delrieu, C. Estournel, N. Filali Boubrahmi, J. Font, V. Grubisic, S. Gualdi, V. Homar, B. Ivancan-Picek, C. Kottmeier, V. Kotroni, K. Lagouvardos, P. Lionello, M. C. Llasat, W. Ludwig, C. Lutoff, A. Mariotti, E. Richard, R. Romero, R. Rotunno, O. Roussot, I. Ruin, S. Somot, I. Taupier-Letage, J. Tintor, R. Uijlenhoet, and H. Wernli. HYMEX: A 10-year multidisciplinary program on the mediterranean water cycle. *Bulletin of the American Meteorological Society*, 95(7):1063–1082, 2014.

[17] Weili Duan, Bin He, Kaoru Takara, Pingping Luo, Maochuan Hu, Nor Eliza Alias, and Daniel Nover. Changes of precipitation amounts and extremes over Japan between 1901 and 2012 and their connection to climate indices. *Climate Dynamics*, 45(7-8):2273–2292, 2015.

[18] D B Enfield, A M Mestas-Nunez, D A Mayer, and L Cid-Cerrano. How ubiquitous is the dipole relationship in tropical Atlantic sea surface temperatures? *Journal of Geophysical Research*, 104(C4):7841–7848, 1999.

[19] Estellus. WACMOS-MED. http://wacmosmed.estellus.fr/.

[20] European Space Agency and Technische Universität Wien. Soil Moiture CCI. http://www.esa-soilmoisture-cci.org/, 2012.

[21] Joshua B. Fisher, Kevin P. Tu, and Dennis D. Baldocchi. Global estimates of the land-atmosphere water flux based on monthly AVHRR and ISLSCP-II data, validated at 16 FLUXNET sites. *Remote Sensing of Environment*, 112(3):901–919, 2008.

[22] Francesco Geri, Valerio Amici, and Duccio Rocchini. Human activity impact on the heterogeneity of a Mediterranean landscape. *Applied Geography*, 30(3):370–379, 2010.

[23] Filippo Giorgi and Piero Lionello. Climate change projections for the Mediterranean region. *Global and Planetary Change*, 63(2-3):90–104, 2008.

[24] Adam K. Gobena, Frank a. Weber, and Sean W. Fleming. The Role of Large-Scale Climate Modes in Regional Streamflow Variability and Implications for Water Supply Forecasting: A Case Study of the Canadian Columbia River Basin. *Atmosphere-Ocean*, 51(4):380–391, 2013.

[25] Przemyslaw Grzegorzewski and Paulina Ziembinska. *Spearmans Rank Correlation Coefficient for Vague Preferences*, volume 7022 of *Lecture Notes in Computer Science*. Springer Berlin Heidelberg, Berlin, Heidelberg, 2011.

[26] A. Hannachi, I. T. Jolliffe, D. B. Stephenson, and N. Trendafilov. In search of simple structures in climate: Simplifying EOFS. *International Journal of Climatology*, 26(1):7–28, 2006.

[27] A. Hannachi, I. T. Jolliffe, and David B. Stephenson. Empirical orthogonal functions and related techniques in atmospheric science: A review. *International Journal of Climatology*, 27(2007):1119–1152., 2007.

[28] J.D. Horel. Complex Principal Component Analysis: Theory and Examples, 1984.

[29] J. T. Houghton, Y. Ding, D. J. Griggs, M. Noguer, P. J. van der Linden, X. Dai, K. Maskell, and C. A. Johnson. Contribution of Working Group I to the Third Assessment Report of the Intergovernmental Panel on Climate Change. Technical report, IPCC 2001, Cambridge, United Kingdom and New York, NY, USA, 2001.

[30] George J. Huffman, Angeline Pendergrass, and National Center for Atmospheric Research Staff (Eds). TRMM: Tropical Rainfall Measuring Mission, 2017.

[31] James W Hurrell, Yochanan Kushnir, Geir Ottersen, and Martin Visbeck. An overview of the North Atlantic Oscillation. In *Climatic Significance and Environmental Impact*, number 134, pages 1–35. 2003.

[32] Intergovernmental Panel on Climate Change. *Climate Change 2014: Impacts, Adaptation and Vulnerability. Part B: Regional Aspects. Contribution of Working Group II to the Fifth Assessment Report of the Intergovernmental Panel on Climate Change.* Cambridge University Press, Cambridge, United Kingdom and New York, NY, USA, 2014.

[33] Fengjun Jin, Akio Kitoh, and Pinhas Alpert. Water cycle changes over the Mediterranean: a comparison study of a super-high-resolution global model with CMIP3. *Philosophical transactions. Series A, Mathematical, physical, and engineering sciences*, 368(1931):5137–49, 2010.

[34] Robert J. Joyce, John E. Janowiak, Phillip A. Arkin, and Pingping Xie. CMORPH: A Method that Produces Global Precipitation Estimates from Passive Microwave and Infrared Data at High Spatial and Temporal Resolution. *Journal of Hydrometeorology*, 5(3):487–503, 2004.

[35] Ercan Kahya. *Hydrological, Socioeconomic and Ecological Impacts of the North Atlantic Oscillation in the Mediterranean Region*, volume 46 of *Advances in Global Change Research*. Springer Netherlands, Dordrecht, 2011.

[36] Henry F. Kaiser. The varimax criterion for analytic rotation in factor analysis. *Psychometrika*, 23(3):187–200, 1958.

[37] W. Köppen. Versuch einer Klassifikation der Klimate, vorzugsweise nach ihren Beziehungen zur Pflanzenwelt. *Geographische Zeitschrift*, 6(12 H):657–679, 1900.

[38] Markus Kottek, Jürgen Grieser, Christoph Beck, Bruno Rudolf, and Franz Rubel. World map of the Köppen-Geiger climate classification updated. *Meteorologische Zeitschrift*, 15(3):259–263, 2006.

[39] P Lionello, P Malanotte-Rizzoli, and R Boscolo. The Mediterranean climate: an overview of the main characteristics and issues. *Developments in earth*, 2006.

[40] Piero Lionello, Fatima Abrantes, Letizia Congedi, Francois Dulac, Miro Gacic, Damià Gomis, Clare Goodess, Holger Hoff, Haim Kutiel, Jürg Luterbacher, Serge Planton, Marco Reale, Katrin Schröder, Maria Vittoria Struglia, Andrea Toreti, Michael Tsimplis, Uwe Ulbrich, and Elena Xoplaki. Introduction: Mediterranean climate-background information. *The Climate of the Mediterranean Region*, 2012.

[41] J. I. López-Moreno, S. M. Vicente-Serrano, E. Morán-Tejeda, J. Lorenzo-Lacruz, A. Kenawy, and M. Beniston. Effects of the North Atlantic Oscillation (NAO) on combined temperature and precipitation winter modes in the Mediterranean

mountains: Observed relationships and projections for the 21st century. *Global and Planetary Change*, 77(1-2):62–76, 2011.

[42] E N Lorenz. Empirical Orthogonal Functions and Statistical Weather Prediction, 1956.

[43] Annarita Mariotti, Maria Vittoria Struglia, Ning Zeng, and K.-M. Lau. The Hydrological Cycle in the Mediterranean Region and Implications for the Water Budget of the Mediterranean Sea. *Journal of Climate*, 15:1674–1690, 2002.

[44] Annarita Mariotti, Ning Zeng, Jin-Ho Yoon, Vincenzo Artale, Antonio Navarra, Pinhas Alpert, and Laurent Z X Li. Mediterranean water cycle changes: transition to drier 21st century conditions in observations and CMIP3 simulations. *Environmental Research Letters*, 3(4):044001, 2008.

[45] Brecht Martens, Diego G. Miralles, Hans Lievens, Robin van der Schalie, Richard A. M. de Jeu, Diego Férnandez-Prieto, Hylke E. Beck, Wouter A. Dorigo, and Niko E. C. Verhoest. GLEAM v3: satellite-based land evaporation and root-zone soil moisture. *Geoscientific Model Development Discussions*, pages 1–36, 2017.

[46] Adrián Martínez-Asensio, Marta Marcos, Michael N. Tsimplis, Damià Gomis, Simon Josey, and Gabriel Jordà. Impact of the atmospheric climate modes on Mediterranean sea level variability. *Global and Planetary Change*, 118:1–15, 2014.

[47] D. G. Miralles, T. R H Holmes, R. A M De Jeu, J. H. Gash, A. G C A Meesters, and A. J. Dolman. Global land-surface evaporation estimated from satellite-based observations. *Hydrology and Earth System Sciences*, 15(2):453–469, 2011.

[48] D. G. Miralles, C. Jiménez, M. Jung, D. Michel, A. Ershadi, M. F. McCabe, M. Hirschi, B. Martens, A. J. Dolman, J. B. Fisher, Q. Mu, S. I. Seneviratne, E. F. Wood, and D. Fernández-Prieto. The WACMOS-ET project - Part 2: Evaluation of global terrestrial evaporation data sets. *Hydrology and Earth System Sciences*, 20(2):823–842, 2016.

[49] G. W K Moore and I. A. Renfrew. Cold European winters: Interplay between the NAO and the East Atlantic mode. *Atmospheric Science Letters*, 13(1):1–8, 2012.

[50] National Aeronautics and Space Administration (NASA). MODIS Evapotranspiration. https://modis.gsfc.nasa.gov/data/dataprod/mod16.php.

[51] National Center for Atmospheric Research Staff (Eds). The Climate Data Guide: Precipitation Data Sets: Overview & Comparison table. https://climatedataguide.ucar.edu/climate-data/precipitation-data-sets-overview-comparison-table, 2014.

[52] NOAA. GPCP Version 2.3 Combined Precipitation Data Set. https://www.esrl.noaa.gov/psd/data/gridded/data.gpcp.html.

[53] ORNL DAAC. Spatial Data Access Tool (SDAT). https://doi.org/10.3334/ORNLDAAC/1388, 2017.

[54] M. C. Peel, B. L. Finlayson, and T. a. McMahon. Updated world map of the Köppen-Geiger climate classification. *Meteorologische Zeitschrift*, 15:259–263, 2006.

[55] S. Queralt, E. Hernández, D. Barriopedro, D. Gallego, P. Ribera, and C. Casanova. North Atlantic Oscillation influence and weather types associated with winter total and extreme precipitation events in Spain. *Atmospheric Research*, 94(4):675–683, 2009.

[56] P. Quintana Seguí, A. Ribes, E. Martin, F. Habets, and J. Boé. Comparison of three downscaling methods in simulating the impact of climate change on the hydrology of Mediterranean basins. *Journal of Hydrology*, 383(1-2):111–124, 2010.

[57] Balaji Rajagopalan, Yochanan Kushnir, and Yves M. Tourre. Observed decadal midlatitudes and tropical Atlantic climate variability.pdf, 1998.

[58] Eugene M. Rasmusson, Phillip a. Arkin, Wen-Yuan Chen, and John B. Jalickee. Biennial Variations in Surface Temperature over the United States as Revealed by Singular Decomposition, 1981.

[59] Michael B. Richman. Rotation of Principal Components. *Journal of Climatology*, 6:293–335, 1986.

[60] A. R. Robinson, W. G. Leslie, A. Theocharis, and A. Lascaratos. Mediterranean Sea Circulation. *Encyclopedia of Ocean Sciences: Second Edition*, pages 710–725, 2008.

[61] J. Sáenz, J. Zubillaga, and C. Rodríguez-Puebla. Interannual variability of winter precipitation in Northern Iberian Peninsula. *International Journal of Climatology*, 21:1503–1513, 2001.

[62] J. Sáenz, J. Zubillaga, and C. Rodríguez-Puebla. Interannual winter temperature variability in the north of the Iberian Peninsula. *Climate Research*, 16(3):169–179, 2001.

[63] Ana Rita Salgueiro, Maria J. Machado, Mariano Barriendos, Henrique Garcia Pereira, and Gerardo Benito. Flood magnitudes in the Tagus River (Iberian Peninsula) and its stochastic relationship with daily North Atlantic Oscillation since mid-19th Century. *Journal of Hydrology*, 502:191–201, 2013.

[64] Nico Salmaso. Influence of atmospheric modes of variability on a deep lake south of the Alps. *Climate Research*, 51(2):125–133, 2012.

[65] Christian-Dietrich Schönwiese. Praktische Statistik für Meteorologen und Geowissenschaftler. *Zeitschrift für Geomorphologie*, 52:3, 2006.

[66] Sonia I. Seneviratne, Thierry Corti, Edouard L. Davin, Martin Hirschi, Eric B. Jaeger, Irene Lehner, Boris Orlowsky, and Adriaan J. Teuling. Investigating soil moisture-climate interactions in a changing climate: A review. *Earth-Science Reviews*, 99(3-4):125–161, 2010.

[67] M. Spencer and R. Essery. Scottish snow cover dependence on the North Atlantic Oscillation index. *Hydrology Research*, page nh2016085, 2016.

[68] David W. J. Thompson and John M. Wallace. The Arctic oscillation signature in the wintertime geopotential height and temperature fields. *Geophysical Research Letters*, 25(9):1297, 1998.

[69] Mladen Todorovic, Biljana Karic, and Luis S. Pereira. Reference evapotranspiration estimate with limited weather data across a range of Mediterranean climates. *Journal of Hydrology*, 481:166–176, 2013.

[70] K E Trenberth, L Smith, T T Qian, A Dai, and J Fasullo. Estimates of the global water budget and its annual cycle using observational and model data. *Journal of Hydrometeorology*, 8(4):758–769, 2007.

[71] R M Trigo. Relations between variability in the Mediterranean region and Mid-latitude variability. *The Mediterranean Climate: an overview of the main characteristics and issues*, pages 179–226, 2006.

[72] Paul J. van der Linden and Clair E. Hanson. *Climate Change 2007: Impacts, adaptation and vulnerability.* Cambridge University Press, Cambridge, United Kingdom and New York, NY, USA, 2007.

[73] John M. Wallace and David S. Gutzler. Teleconnections in the Geopotential Height Field during the Northern Hemisphere Winter, 1981.

[74] C Z Wang. Atlantic climate variability and its associated atmospheric circulation cells. *Journal of Climate*, 15(13):1516–1536, 2002.

[75] Guiling Wang and David Schimel. Climate Change, Climate Modes, and Climate Impacts. *Annual Review of Environment and Resources*, 28(1):1–28, 2003.

[76] Daniel S Wilks. *Statistical methods in the atmospheric sciences.* Academic press, third edit edition, 2011.

[77] Matteo Zampieri, Fabio D'Andrea, Robert Vautard, Philippe Ciais, Nathalie De Noblet-Ducoudré, and Pascal Yiou. Hot European summers and the role of soil moisture in the propagation of mediterranean drought. *Journal of Climate*, 22(18):4747–4758, 2009.

[78] Ke Zhang, John S. Kimball, Qiaozhen Mu, Lucas A. Jones, Scott J. Goetz, and Steven W. Running. Satellite based analysis of northern ET trends and associated changes in the regional water balance from 1983 to 2005. *Journal of Hydrology*, 379(1-2):92–110, 2009.

[79] Ke Zhang, John S. Kimball, Ramakrishna R. Nemani, and Steven W. Running. A continuous satellite-derived global record of land surface evapotranspiration from 1983 to 2006. *Water Resources Research*, 46(9):1–21, 2010.

[80] Yongqiang Zhang, Jorge L. Peña-Arancibia, Tim R. McVicar, Francis H. S. Chiew, Jai Vaze, Changming Liu, Xingjie Lu, Hongxing Zheng, Yingping Wang, Yi Y. Liu, Diego G. Miralles, and Ming Pan. Multi-decadal trends in global terrestrial evapotranspiration and its components. *Scientific Reports*, 6(1):19124, 2016.